THE UNIVERSITY OF OKLAHOMA

GRADUATE COLLEGE

Integration of Time-Lapse Seismic Data into Automatic History Matching

A Dissertation

SUBMITTED TO THE GRADUATE FACULTY

in partial fulfillment

of the requirements for the degree of

Doctor of Philosophy

By

Yannong Dong

Norman, Oklahoma

2005

THE UNIVERSITY OF OKLAHOMA

GRADUATE COLLEGE

Integration of Time-Lapse Seismic Data into Automatic History Matching

A Dissertation APPROVED FOR THE

MEWBOURNE SCHOOL OF

PETROLEUM AND GEOLOGICAL

ENGINEERING

BY:

Dean S. Oliver, Committee Chair

Abousleiman, Younane

Civan, Faruk

Sondergeld, Carl

Young, Roger A.

© Copyright by Yannong Dong 2005
All Rights Reserved

ACKNOWLEDGEMENTS

I wish to express my sincere appreciation and gratitude to Dr. Dean S. Oliver, Director and Eberly Chair of the Mewbourne School of Petroleum and Geological Engineering (MPGE) for his invaluable assistance, guidance, and support during this study, and to his family for introducing me to this country and her different culture. I also thank Dr. Younane Abousleiman, Brummet/ONEOK Chair Professor of MPGE, Dr. Faruk Civan, Alumni Professor of MPGE, Dr. Carl Sondergeld, Unocal Professor of MPGE, and Dr. Roger A. Young, Professor of the School of Geology and Geophysics, for their active service in my committee and able suggestions for this work.

I also wish to express my appreciation to Dr. Albert C. Reynolds, Professor of Department of the Petroleum Engineering in the University of Tulsa (TU), for his automatic history matching class, which built a strong base for my research.

I would like to extend my thanks and appreciation to all other faculties. I benefitted a lot from their knowledge and excellent classes. Special appreciations to all the staff in both MPGE and the Department of Petroleum Engineering of TU. Their kind and always available help gave me a strong support for my academic life.

I wish to show my sincere appreciation to Dr. Younes Jalali, who sponsored me for my summer internship. I not only accumulated experience about real field projects, but also benefited a lot from discussions with Younes.

I gratefully acknowledge the Department of Energy (DOE), U.S. and all the member companies of TUPREP (**U**niversity of **T**ulsa **P**etroleum **R**eservoir **E**xploitation **P**rojects), for their financial support. The simulator used in this work was provided by the Chevron-Texaco Corporation.

I also would like to give my thanks to my fellow graduate students and research team members in OU and TU. They enriched and broadened my life.

I also want to express my sincere thanks to all the friends that I know in Tulsa and Norman. They provided me invaluable chances to share with American families in their daily lives, their happiness, and their challenges. I give special thanks for their guidance in my spiritual life, which has helped me become more mature beyond my academics.

Lastly, I dedicate this work to my dear wife, Yaqing Gu, for her uninterrupted support during this 4-year journey. I am so glad to have her beside me to share every piece of success and to give me a shield with her unconditional love in difficult situations. Also to my family members in China, my parents and my grandma, for their love and care.

TABLE OF CONTENTS

LIST OF TABLES

LIST OF FIGURES

ABSTRACT

Using the Bayesian framework, the identification of the most probable reservoir model in automatic history matching can be changed into a minimization problem, whose objective function includes square difference between observed data and computed data, as well as square difference between current model parameters and prior model information. Minimizing the objective function once can provide one realization of reservoir field. Due to the non-linearity of the equations describing 3-D, 3-phase flow in porous media, the minimization process is very demanding in both gradient and search direction computations. In this work, the adjoint method (Lagrange Multiplier) is used for gradient computation and the limited memory Broyden-Fletcher-Goldfarb-Shanno (LBFGS) method for search direction calculation.

Production data, such as bottomhole pressure (P_{wf}), gas oil ratio (GOR), and water oil ratio (WOR), are widely used in automatic history matching. Although they can provide high resolution estimation around well locations, properties in regions far from wells are poorly constrained. To reduce uncertainty in estimation, seismic data can be integrated with the production data, to provide areally dense information across whole field. In this work, seismic P-wave impedance change data derived from time-lapse (4D) seismic are used. A series of rock physics models have been added to the reservoir simulator, **C**hevron **L**imited **A**pplication **S**imulation **S**ystem (CLASS), making it possible to compute seismic impedance using saturations and pressures from the simulator. A semi-synthetic case study is used to test the effectiveness of this methodology, and a real case from Bay Marchand field, Gulf of Mexico, shows its potential in an industry level application.

As an alternate to automating history matching through the minimization approach, the ensemble Kalman filter (EnKF) can be used to rapidly update the estimate of model variables. One advantage of the EnKF method is that it is relatively easy to implement as there is no need to write extensive simulator-dependent code. The EnKF can be used to assimilate observed data as they become available to continuously update a set of reservoir simulation models, which makes the EnKF suitable for high-frequency input, for example, measurements from permanent sensors. Generation of an ensemble of "history-matched" models is very appropriate for conducting uncertainty analysis. In this work, a small synthetic case study is used to show that it is possible to integrate both time-lapse seismic impedance data and production data using the EnKF.

CHAPTER I

INTRODUCTION

The process of generating reservoir properties is crucial to reservoir engineers in that 1) they help to make decisions on reservoir management; 2) they are starting points for reservoir predictions. To have reliable realizations, however, is always difficult due to limited availability of information. In contrast to other engineering fields, it is impractical in petroleum engineering to have direct measurements of the necessary properties throughout the reservoir under study, except at well locations. Away from the wells, any information about reservoir parameters can only be inferred through indirect measurements gathered from wells, such as bottomhole pressure (P_{wf}), gas oil ratio (GOR), and water oil ratio (WOR). If the reservoir under study is regarded as a flow system governed by a set of fluid flow equations derived from material and momentum balance equations, the production histories from the reservoir are actually outputs of the system and the reservoir properties are system parameters. The process of estimating system parameters from system outputs is a typical problem in **inverse theory**. Unfortunately, most inverse problems are highly under-determined, which means that the number of system parameters is much greater than the number of system outputs. In this case, there are an unlimited number of combinations of the system parameters, which, if fed back to the system, can reproduce the same system outputs. This non-unique feature makes it necessary to find an appropriate solution to an inverse problem with aid of some particular criteria. In this work, the Bayesian framework, which will be discussed in detail in Chapter 2, is used to ensure plausibility.

For typical oil, gas, and water flow problems, the governing equations are nonlinear, which makes it extremely difficult in most cases to have an analytical solution for saturations and pressures. Reservoir simulation, which discretizes the governing equations in a set of gridblocks and finds numerical solution of distributions of oil, gas, and water at those gridblocks, is a useful tool for estimating solutions. Then, to estimate reservoir parameters is to obtain reservoir simulation model parameters, which can produce production histories having reasonable closeness to observed histories. This process is called history matching. Because reservoirs are usually very heterogenous, there are hundreds of thousands of gridblocks in a typical reservoir simulation system to capture reservoir parameters in high resolution. Manually adjusting parameters in gridblocks is not feasible. Instead, computers are employed to automatically vary the parameters. This process is called automatic history matching.

Automatic history matching can be thought of as a minimization problem, whose objective function includes the sum of squared difference between observed data and computed data, as well as a model parameter regularization term arising from prior information about the reservoir under study. To minimize the objective function, an efficient minimization algorithm must be chosen. There are two categories of minimization methods, gradient based methods and non-gradient based methods. For non-gradient based methods, some well known representatives are simulated annealing (SA) (Deutsch and Journel, 1994; Sen et al., 1995; Ouenes et al., 1992, 1993, 1994; Vasco et al., 1997; Abdassah et al., 1996; Portellaand and Prais, 1999; Romero et al., 2000; Saccomano et al., 2001) and genetic algorithm (GA) (Sen et al., 1995). Although non-gradient based methods can be used to find the global minimization point, they may require thousands or millions of simulation runs to converge. When processing large scale or even medium scale automatic history matching problems, this intensive demanding on simulation computation makes the non-gradient based methods impractical. Therefore, in this work, only gradient based minimization methods are

used.

Some widely used gradient based minimization methods include Steepest Descent method, Gauss-Newton method, Levenberg-Marquardt algorithm and Conjugate Gradient (CG) method. The required inputs for these methods are gradient (first derivative) and/or the Hessian matrix (second derivative) of the objective function. In our problem, the Hessian matrix is constructed involving the sensitivity coefficients of data with respect to model parameters. The sensitivity coefficients for production data typically have large values around well locations and decrease with distance increasing from wells (Li, 2001).

The most straightforward way to compute sensitivity coefficient of a datum with respect to a model parameter is to compute the derivative by finite difference approximation, which is also called the perturbation method. The perturbation method requires two simulation runs, one run with model parameters fixed at base values and the other one with all other model parameters still in base values except one parameter at a perturbed value. The perturbation ratio is usually chosen as 2% to 5% of base parameter value (Li, 2001). Then the sensitivity coefficient can be computed using Eq. 1.1,

$$\frac{\partial g_i}{\partial m_j} = \frac{g_i(m + \triangle m_j) - g_i(m)}{\triangle m_j}\,, \tag{1.1}$$

where,

- $g(\cdot)$ represents a reservoir simulator;
- $g_i(m)$ is the ith simulated datum output from the reservoir simulator;
- m is the model parameter vector currently used;
- $\triangle m_j$ is perturbation value for the jth parameter.

In Eq. 1.1, if $g_i(m)$ is replaced with the objective function, the result will be an entry of the gradient of the objective function. If there are N_m model parameters, $N_m + 1$ simulation runs are required to calculate all sensitivity coefficients.

Although Eq. 1.1 is only practical when number of model parameters is very small and only has theoretical meaning in many cases, it shows that the number of model parameters is a crucial issue to gradient computation. Fine grid models are able to capture reservoir features in small scale, but the number of model parameters is large, and usually require a large amount of effort to compute the gradient. In contrast, a coarse grid can reduce the number of model parameters and is less demanding in gradient computation at the expense of losing detailed trends. For the latter way, re-parametrization is often used to reduce the number of model parameters, such as zonation method and pilot point method.

Zonation method for automatic history matching was introduced by Jacquard and Jain (1965) and Jahns (1966) and then used by Gavalas et al. (1976); Shah et al. (1978); Makhlouf et al. (1993). A recent application can be found in Huang et al. (2001). The zonation method divides a reservoir into zones and assume homogeneous reservoir properties within each zone, which reduces model parameters to just a few values for those zones. Although it decreases the number of model parameters, zonation method can not provide estimations at the scale smaller than zone scales.

The pilot point method was developed by de Marsily et al. (1984); Certes and de Marsily (1991). Further work can be found in both petroleum engineering and groundwater hydrology (RamaRao et al., 1995; Landa and Horne, 1997; Xue et al., 1997; Wen et al., 1997; Bissell et al., 1997; Roggero, 1997; Arenas et al., 2001; Wen et al., 2002). In the pilot point method we 1) choose a series of pilot point locations in a reservoir model; 2) adjust model parameters at those pilot points to minimize the objective function; 3) interpolate among the pilot points to get field distributions of model parameters, for example, kriging interpolation. The pilot point method has overshooting problems at pilot points, which can be seen in the figures of Xue et al. (1997). Some other problems of the pilot point method include determination of optimal pilot point locations and choice of a interpolation scheme most suitable for

a specific case.

If the gridblock size is kept small to provide high resolution, more efficient gradient computation methods must be used. Gradient simulator method is one widely applied method. Early results in hydrology and petroleum engineering can be found in Yeh (1986) and Anterion et al. (1989). This method computes sensitivity coefficients of data with respect to model parameters at each time step after flow equations are solved in the simulator. The gradient simulator method solves a matrix problem with the same coefficient matrix as the simulation equations but different multiple right hand vectors. The efficiency of gradient simulator method decreases dramatically with increase of the number of model parameters.

A more efficient method to compute the gradient is the adjoint method, which is also the method used in this work. The adjoint method was applied to petroleum engineering by Chavent et al. (1975) and Chen et al. (1974). He et al. (1997) applied this method to a 3-D single phase problem, and a 2-phase (water/oil) problem was done by Wu et al. (1999). Finally, the adjoint method was successfully extended to a 3-D, 3-phase flow problem (Li et al., 2003).

The adjoint method is derived using the Lagrange Multiplier. It has some important features. First, the adjoint equations are solved from the last time step to the first time step. A typical process is to save pressure and saturation from flow equations at each simulation time step when the flow equations are solved. After finishing the simulation run, the adjoint equations are solved using the stored pressure and saturation information. Secondly, the adjoint equations are linear although the forward reservoir simulation equations are non-linear, which implies that the backward solution does not necessarily require the same time step interval as the forward solution. By carefully choosing time step intervals when solving the adjoint equations, more efficiency can be gained. Third, computation cost of solving the adjoint equations is independent of the number of model parameters, but related to the number

of data because each individual datum requires a set of Lagrange multipliers being saved at each time step. If the number of data is very large, computation of sensitivity coefficients of each datum will become demanding in computational cost. This potential disadvantage, however, can be avoided by choosing an appropriate minimization algorithm.

As stated before, Newton type minimization methods, such as the Gauss-Newton method and Levenberg-Marquardt algorithm, have been widely used to minimize non-linear objective function because of their quadratic convergence rate. This fast convergence rate, however, is achieved at the expense of requiring computation of the Hessian matrix of the objective function as well as the gradient. The Hessian matrix is the second derivative of the objective function with respect to model parameters. To compute this matrix requires computation of sensitivity coefficient matrix G. Since the dimension of matrix G is $N_d \times N_m$, where N_d is the number of data and N_m is the number of model parameters, it will become impractically expensive to either store the matrix when model size is large, or to compute sensitivity coefficients when the number of data is large. When large scale problems are considered, those two bottlenecks usually make the Newton type methods unfeasible.

In contrast to the Newton type methods, another group of gradient based minimization methods requires only the gradient of the objective function. Some well known representatives are Steepest Descent method, Conjugate Gradient (CG) method, Preconditioned Conjugate Gradient (PCG) method, the Broyden-Fletcher-Goldfarb-Shanno (BFGS) method and the limited memory Broyden-Fletcher-Goldfarb-Shanno (LBFGS) method. Since none of these require the Hessian matrix, the sensitivity coefficient matrix is not a problem any more. Particularly, if the whole objective function is used as a datum, the adjoint equations can efficiently compute the gradient of the objective function (Li, 2001; Zhang and Reynolds, 2002; Zhang, 2002).

Thus, for large scale problems, these methods are preferred. Among them, the Steepest Descent method uses the negative gradient as search direction, which makes it most easily implemented once the gradient is obtained from the adjoint equations. The major drawback of the Steepest Descent method is that it converges slowly, especially as the objective function approaches its minimization point. Since each iteration step involves a simulation run and solving the adjoint equations, the number of iteration steps must be kept as small as possible.

The CG method uses not only current gradient information, but also gradient information saved at previous iteration steps, to construct search direction for the next iteration step. Since it is only necessary to store a small number of vectors, memory cost is very low. Generally, the CG method converges faster than the Steepest Descent method, but in order to have reasonable convergence speed for large scale problems, the matrix condition number is improved by multiplication by a preconditioning matrix. For our history matching problems, however, it is difficult to find a general scheme to construct the preconditioning matrix (Zhang and Reynolds, 2002; Zhang, 2002).

The BFGS method (Broyden, 1970; Fletcher, 1970; Goldfarb, 1970; Shanno, 1970) has a convergence rate between linear and quadratic because it uses the Hessian approximation constructed from the gradient. However, the BFGS method explicitly forms the Hessian approximation, which is still impractical for large scale problems. In 1980, Nocedal (1980) introduced a new scheme to implement the BFGS method without explicitly storing the Hessian approximation. Instead, it only saves the gradient and the objective function value from previous iteration steps. This new implementation of the BFGS method is called the limited memory BFGS (LBFGS) method. After intensive comparison using different synthetic and real case studies, Zhang and Reynolds (2002) concluded that the LBFGS method is the most efficient minimization method for typical history matching problems.

As the name implies, automatic history matching mainly uses production data, including P_{wf}, GOR, and WOR. Estimates of reservoir properties obtained from production data typically are only well-resolved near the well-bore. For regions far from wells, model estimation is usually poorly constrained, especially when the model size is large or the number of production data is limited. Although inverse problems in general, and automatic history matching problems in particular, are under-determined, i.e., the number of data is smaller than the number of model parameters that need to be adjusted, results derived from small amounts of production data still provide estimates that are less than satisfying. It would clearly be beneficial to make use of some type of "space-dense" data that would improve the resolution of the estimate in the gridblocks far away from well locations. Seismic data is the most promising candidate for improved spatial coverage. In addition, advances in automatic history matching, such as the adjoint method and the LBFGS algorithm, have begun to allow researchers to consider the integration of large amount of data.

The amplitude of seismic signals are sensitive to both static rock properties, such as shaliness and lithology, and dynamic rock properties, such as pore pressure and saturation at the time when seismic is shot. Large temperature changes, such as occur in steam floods, will also result in significant changes in the amplitude of seismic reflection data. In this work, reservoir temperature is assumed to be constant, so effects from temperature changes are not considered. For purpose of automatic history matching, pressure and saturation changes reflected through seismic data are most interesting to us because they are related to some very important reservoir parameters, such as permeability and porosity. If seismic data from only one survey are used, it is difficult to differentiate static effects from dynamic effects. To reduce the effects from uncertainty in static parameters, time-lapse seismic data can be used. Time-lapse seismic repeats seismic surveys at same locations but different times. By subtracting data obtained in the base survey from data obtained in the repeat survey, the effects

of fluid changes can be emphasized.

Time-lapse seismic is not a new topic in petroleum engineering and geophysics. The pioneering work of time-lapse seismic can be traced back to late 1980's and early 1990's (Wayland and Lee, 1986; Greaves and Fulp, 1987; Dunlop et al., 1991). Similar studies can also be found at the Foinhaven Field (Cooper et al., 1999), the Meren Field in Nigeria (Lumley et al., 1999) and the Bay Marchand field in the Gulf of Mexico (Behrens et al., 2002). The primary objectives at Foinhaven were simply to map fluid movements and to identify by-passed oil. The authors of the study concluded that the time-lapse signal qualitatively agreed with the expected reservoir performance. At Meren, the goal was to identify pathways of injected water, sealing faults, and compartments that may have by-passed oil. For Bay Marchand, time-lapse seismic was used to monitor water flux and identify the bypassed oil. Moreover, the analysis provided a qualitative comparison of the quality of seismic data before and after cross equalization, which is a very important step in time-lapse seismic data processing. The authors concluded that the data allowed these objectives to be achieved. Other reservoir management references that discuss time-lapse seismic include Ross et al. (1996); Hughes (1998); Shyeh et al. (1999); Blonk et al. (2000); Burkhart et al. (2000); Hughes (2000); Khan et al. (2000); Rickett and Lumley (2001); Waggoner et al. (2002); Gouveia et al. (2004); Raef et al. (2004). According to Lumley and Viejo (2004), in the 4 years between 2000 and 2003, total time-lapse seismic expenditures were about (US) $500 million.

Besides direct use of time-lapse seismic as a reservoir monitoring tool, the other, more difficult, approach is to integrate time-lapse seismic data in automatic history matching to estimate the reservoir flow parameters, such as permeability and porosity. Landa and Horne (1997) estimated reservoir parameters assuming that water saturation changes could be derived from the time-lapse seismic. They included dynamic data observed from wells. The reservoir model was re-parameterized to

decrease the number of model parameters and the gradient simulator method was used to compute the gradient and the Hessian matrix. Huang et al. (1997) used time-lapse seismic amplitude data and the finite perturbation method to calculate required derivatives. The method used by Waggoner (1998) was similar. Huang et al. (2001) used zonation to history match both production data and time-lapse seismic data. Each zone was assumed to have homogeneous properties. Because the number of model parameters was small, the finite perturbation method was used to compute the derivatives. Like Landa and Horne (1997), van Ditzhuijzen et al. (2001) matched water saturation changes presumably derived from multiple seismic surveys, as well as production data. The model parameters were geometric parameters of the faults, such as positions, size and, throw because the authors believed that in that area, the geometric parameters were more important than the porosity and permeability for the reservoir management. Arenas et al. (2001) conducted semi-automatic history matching using both production data and P-wave velocity differences. The pilot point method was employed to decrease the number of model parameters and Kriging interpolation was used to recover the whole porosity and permeability fields once the pilot points were updated during minimization. The gradient simulator method was used to compute sensitivity coefficients and the Levenberg-Marquardt algorithm to minimize the objective function. Phan and Horne (2002) also used water saturation changes interpreted from time-lapse seismic records to adjust channel parameters, including channel orientation and deviation of channel center line from maximum continuity. In a recent work, Waggoner et al. (2002) used acoustic impedance difference derived from time-lapse seismic. To reduce the number of model parameters, they adjusted only vertically averaged porosities and calculated the permeabilities through a correlation between the porosity and permeability. Due to the relatively small number of model parameters, they were able to use the finite perturbation method to compute derivatives. Bogan et al. (2003) used multiple time-lapse

seismic attributes, including velocity, impedance, and amplitude in a GOM field to estimate fluid flow barriers, facies parameters, and variogram structures. Gosselin et al. (2003) tested automatic history matching method with both production data and time-lapse seismic data, using a gradient based optimization method. Gradzones were used in re-parameterizations. Kretz et al. (2004a) used the gradual deformation method to history match the production data and time-lapse seismic data, but their time-lapse seismic data were only indicators of changes observed through 4D seismic. Pannett et al. (2004) matched synthetic amplitude data generated using a software based on some rock physics parameters. Kretz et al. (2004b) matched water fronts extracted from time-lapse seismic surveys. Mezghani et al. (2004) used time-lapse seismic acoustic impedance in history matching, together with production data. The finite perturbation method was used to compute the required derivatives. Dong and Oliver (2005) matched both seismic impedance change data and production data in a medium scale problem. The adjoint method was used to compute gradient and the LBFGS method for search direction calculation.

The type of time-lapse seismic data used for property estimation has varied among the researchers. Huang et al. (1997) used amplitude difference or other seismic attributes difference, while Arenas et al. (2001) used velocity difference. Gosselin et al. (2000) assumed that pressure and saturation changes were available. Landa and Horne (1997) also assumed that saturation changes could be obtained directly from time-lapse surveys. While a number of geophysicists (Tura and Lumley, 1999; Landrø, 2001; Meadows, 2001) have assumed that changes in saturation and pressure can be estimated directly from time-lapse seismic data (including offset data), it is clearly better to work directly from the rock physics, mass, and momentum balance relationships to ensure that all data are honored. In this work, seismic P-wave impedance change data derived from time-lapse seismic are chosen.

Seismic P-wave impedance (hereafter, seismic impedance) is defined as the multiplication of body density and P-wave velocity. If a rock is very hard to compress, its impedance will have high value; if a rock is soft, it will have low impedance value. During production, elastic properties of reservoir rocks will change because pressure and saturation are different from time to time. For example, if a reservoir is under water flooding, its rocks usually become stiffer because water is generally more difficult to compress than oil. These changes in rock properties can be inferred through changes in seismic impedance data. On the other hand, some fluid flow parameters, such as permeability and porosity, must be indirectly inferred from changes in pressure and saturation distributions. It can be seen that seismic impedance is actually a bridge between permeability and porosity, and pressure and saturation distributions. Based on preliminary investigation (Dong and Oliver, 2002), seismic impedance change data are used because seismic impedance change data are relatively insensitive to variations of poorly constrained variables such as shaliness.

The objective function derived from the Bayesian framework includes the squared mismatch between observed data and computed data. To integrate seismic impedance change data into the objective function, it is required to have some equations to compute seismic impedance change using outputs from the reservoir simulator. This task is achieved by inserting a series of rock physics models in the reservoir simulator. Some well known rock physics models are the Gassmann equation (Gassmann, 1951), the Han equation (Han et al., 1986), and the Ramammorthy equation (Ramammorthy et al., 1995). For studies of real field data, ad hoc equations particularly suitable for the field are sometimes used to achieve better match to observed seismic impedance data. One example can be found in the Bay Marchand field study, which is discussed in Chapter 5.

One important issue to be considered with integration of seismic impedance change data is estimation of the data noise covariance matrix. As will be seen in Chapter 2,

the objective function has data noise covariance matrix as its weighting matrix for squared mismatch of observed data and computed data. When only production data are used, the noise covariance matrix is usually assumed to be diagonal with its entries equal to the noise variance of each individual datum because the production data sampling interval is generally larger than their correlation length in time space (Aanonsen et al., 2002, 2003), so data noise is uncorrelated. It is probably not valid, however, to assume that the noise in the seismic data are not correlated. This correlated noise typically comes from two sources, data gathering system when the seismic survey is shot and seismic data processing. To make appropriate balances among seismic data, the data noise covariance structure must be evaluated (Aanonsen et al., 2002, 2003). There are two ways to do this. One is to capture noise features through the whole work flow for computation of seismic impedance change. The other is to analyze noise structure directly from the seismic data by doing variogram analysis on impedance change data residual. In this work, the latter method is used. For the synthetic case study shown in Chapter 4, a diagonal noise covariance matrix is used because both observed and computed seismic impedance change data are generated at each gridblock using only pressure and saturation in that gridblock, but for the real case study in Chapter 5, a non-diagonal matrix is constructed.

Automatic history matching through minimizing an objective function can successfully integrate both seismic impedance change data and production data with the help from the adjoint method and the LBFGS method. Although the results are satisfactory (Dong and Oliver, 2005), there are still some drawbacks. First of all, the adjoint equations require access to the source code of the reservoir simulator, which prevents researchers from building adjoint system on commercial simulators. Secondly, the adjoint code is very time-consuming to write and needs to be re-written if switching to another simulator. Third, the minimization process uses all data once to find an optimal model estimation. If new data are available, this minimization

process needs to start over with all data integrated. This feature makes the minimization approach unsuitable for high-frequency data input, for example, measurements from permanent sensors. Moreover, to minimize the objective function once can only provide one "history-matched" model. To conduct uncertainty analysis, however, a set of "history-matched" models are required. Considering the time required for one minimization of the data mismatch (Zhang, 2002; Gao and Reynolds, 2004), the uncertainty analysis by minimizing multiple initial models is not very practical for large reservoir models. In that case, an investigation of alternate automatic history matching methods is worthwhile.

In this work, the ensemble Kalman filter (EnKF) (Evensen, 1994) with integration of both time-lapse seismic data and production data is investigated. The EnKF is an extension of the traditional Kalman filter (Kalman, 1960), which has been widely applied to optimal control field. The traditional Kalman filter is appropriate for data assimilation problem in linear systems, while for non-linear systems, some modifications are needed as found, for example, the extended Kalman filter (EKF). The EKF is not practical due to requirement of the adjoint system. The EnKF is a Monte Carlo method that does not require the adjoint equations and is independent of reservoir simulators. It continuously updates an ensemble of reservoir models whenever new observations are available. The final output is a set of "history-matched" models, which are very suitable for uncertainty analysis. The EnKF has been applied mainly in oceanography and meteorology during the past decade (Evensen, 1994, 1996; Houtekamer and Mitchell, 1998; Anderson and Anderson, 1999; Anderson, 2001; Houtekamer and Mitchell, 2001; Evensen, 2003, 2004), but recently there are some applications in petroleum engineering (Nævdal et al., 2002, 2005; Gu and Oliver, 2005b,a; Gao et al., 2005; Liu and Oliver, 2005; Wen and Chen, 2005).

In this dissertation, a small synthetic case study is conducted, showing that it is feasible to integrate time-lapse seismic impedance data into reservoir characterization

using the EnKF. Improved initial member sampling method is used to increase initial members' quality, which provides a more stable filter behavior.

There are 7 chapters in this dissertation. Chapter 2 introduces the Bayesian framework and the adjoint method. Chapter 3 discusses in detail about the time-lapse seismic and seismic impedance change. Some rock physics models used in this work are listed and discussed. To show that seismic impedance change data can provide reasonable constraints in automatic history matching, a sensitivity computation is shown of seismic impedance change data points with respect to model parameters in a small synthetic case. Chapter 4 mainly includes results obtained from two case studies, a small synthetic one and a medium-sized semi-synthetic one generated from the Tengiz field. Chapter 5 focuses on a real case study from the Bay Marchand field, the Gulf of Mexico. Some real case study related issues are covered. Chapter 6 is devoted to the EnKF method. The small synthetic case study is discussed in detail there. Finally, conclusions are presented in Chapter 7.

CHAPTER II

THE BAYESIAN FRAMEWORK AND ADJOINT METHOD

On one hand, the purpose of automatic history matching is to match the observed history, i.e., to match the observations, by adjusting flow parameters in each reservoir simulation gridblock. One the other hand, some existing information about the reservoir under study must be considered during the matching process. The estimated reservoir model parameters should be consistent with the prior geologic information. To properly transform an automatic history matching into a minimization problem, one central question is how to consider simultaneously these two parts to provide an objective function, which is not only mathematically correct, but also physically make sense. Here, the Bayesian framework is used to determine the correct objective function.

2.1 Bayesian framework

In this section, a brief introduction to the Bayesian framework for inverse problems will be given. A thorough description can be found in Tarantola (1987).

Suppose that the reservoir under study can be modelled as a random field in which the reservoir parameters, such as porosity and permeability, are all random variables. The probability of occurrence of any particular configuration of flow properties can then be characterized using a probability density function (hereafter PDF) $p_M(m)$. In our application, the random field is usually assumed to be Gaussian. Under this

assumption, the PDF of the reservoir model can be written as,

$$p_M(m) = a \exp\left(-\frac{1}{2}\left(m - m_{\text{prior}}\right)^T C_M^{-1}\left(m - m_{\text{prior}}\right)\right), \tag{2.1}$$

where m is the vector of model parameters, a is a constant, m_{prior} is the best estimate for parameters based on prior information about the field, and C_M is the model variable covariance matrix. The prior information contains general knowledge about the reservoir, such as expected porosity and permeability. The matrix C_M is usually constructed through geostatistical tools. Its diagonal entries are variances of all model parameters.

Observed data gathered during exploration and production, such as production data from wells and seismic data from seismic surveys, can be written as,

$$d_{\text{obs}} = d_{\text{true}} + \epsilon\,, \tag{2.2}$$

where ϵ is measurement noise. The addition of the noise term accounts for the fact that the recorded observations are corrupted by noise due to limitations of measurement tools. If the measurement noise is also assumed to be Gaussian with mean equal to zero, then the PDF of the observation noise can be written as Eq. 2.3,

$$\begin{aligned} p(\epsilon) &= b \exp\left(-\frac{1}{2}\epsilon^T C_D^{-1}\epsilon\right) \\ &= b \exp\left(-\frac{1}{2}\left(d_{\text{true}} - d_{\text{obs}}\right)^T C_D^{-1}\left(d_{\text{true}} - d_{\text{obs}}\right)\right), \end{aligned} \tag{2.3}$$

where b is a constant and C_D is the measurement noise covariance matrix, which defines correlations among noise contained in observed data, diagonal for production data but non-diagonal for seismic data. The diagonal entries of C_D are variances of the measurement noise. On the other hand, if the true model m_{true} is given to a reservoir simulator, then some "true" observations can be computed, $d_{\text{true}} = g(m_{\text{true}})$. Since the measurement noise ϵ is random, the observations given the true model m_{true} are also random and can be described using the conditional PDF written in Eq. 2.4,

$$p(d_{\text{obs}} \mid m_{\text{true}}) = b \exp\left(-\frac{1}{2}\left(g(m_{\text{true}}) - d_{\text{obs}}\right)^T C_D^{-1}\left(g(m_{\text{true}}) - d_{\text{obs}}\right)\right), \tag{2.4}$$

where $g(m_{\text{true}})$ represents the forward simulation run.

According to the Bayes' Theorem, the conditional PDF of the model parameters m given observations, d_{obs}, can be written as,

$$p(m \mid d_{\text{obs}}) = \frac{p(d_{\text{obs}} \mid m) p_M(m)}{p(d_{\text{obs}})} = \frac{p(d_{\text{obs}} \mid m) p_M(m)}{\int p(d_{\text{obs}} \mid u) p_M(u) du}\,, \tag{2.5}$$

where $p(d_{\text{obs}})$ is the PDF of the observation. Inserting Eq. 2.1 and Eq. 2.4 into Eq. 2.5, the conditional PDF can be written as Eq. 2.6,

$$\begin{aligned} p(m \mid d_{\text{obs}}) =& c \exp\left(-\frac{1}{2}\left(m - m_{\text{prior}}\right)^T C_M^{-1}\left(m - m_{\text{prior}}\right)\right) \\ & \times \exp\left(-\frac{1}{2}\left(g(m) - d_{\text{obs}}\right)^T C_D^{-1}\left(g(m) - d_{\text{obs}}\right)\right)\,, \end{aligned} \tag{2.6}$$

where c is a normalizing constant. The PDF in Eq. 2.6 is called the posterior PDF. For our automatic history matching problem, we want to generate an estimate of m that has the maximum probability, i.e., the maximum a posteriori (MAP) estimate. Obviously, such an estimate can be obtained by minimizing the arguments of the exponential term in Eq. 2.6, which gives the objective function,

$$\begin{aligned} O(m) &= \frac{1}{2}\left(m - m_{\text{prior}}\right)^T C_M^{-1}\left(m - m_{\text{prior}}\right) + \frac{1}{2}\left(g(m) - d_{\text{obs}}\right)^T C_D^{-1}\left(g(m) - d_{\text{obs}}\right) \\ &= O_m(m) + O_d(m)\,, \end{aligned} \tag{2.7}$$

where $O_m(m)$ is the model mismatch term and $O_d(m)$ is the data mismatch term. There are some important features of this objective function. First, it conditions to the observed data as well as the prior information. If only data mismatch term is used, for example, constraints from the prior are lost. Secondly, the model mismatch term provides normalization for the Hessian matrix. Its effect is two-fold, 1) it prevents the Hessian matrix from being numerically singular; 2) it damps extremely high or low values resulting from over-adjustments in data mismatch term. Third, both data and model parameters are well balanced by their variances contained in C_M and C_D. Also, the correlations among model parameters can be retained through non-diagonal part of C_M.

From the perspective of reservoir management, values of permeability and porosity at some specific places of the reservoir model are not very meaningful, especially considering that the results of automatic history matching problem are non-unique. The more important problem is to characterize uncertainties of future reservoir performance. To do that using Monte Carlo methods requires generation of a number of history-matched models. One general work flow to obtain a set of estimations that all honor both the prior and the observed data is:

- Develop a mathematical model of the posterior PDF of the reservoir model, for example, the one shown in Eq. 2.5 and Eq. 2.6.
- Sample the PDF to obtain a series of realizations;
- Feed the realizations into a reservoir simulator to predict their performance, such as oil production rates, water cuts at wells, etc.;
- Calculate statistical parameters summarizing the performance predictions, such as histogram, P10, P90, etc.;
- Provide uncertainty analysis based on statistical parameters.

To implement this work flow, the key factor is to find an efficient algorithm to sample the posterior PDF. In this work, the **R**andomized **M**aximum **L**ikelihood (**RML**) method is used for sampling (Oliver, 1996; Kitanidis, 1995). This method includes the following 4 steps,

Step 1 Generate an unconditional realization of model variables, m_{uc}, and an unconditional realization of noise in the observed data, resulting in d_{uc};

Step 2 Minimize the objection function in Eq. 2.8 to generate one conditional realization,

$$O(m) = \frac{1}{2}\left(m - m_{\text{uc}}\right)^T C_M^{-1}\left(m - m_{\text{uc}}\right) + \frac{1}{2}\left(g(m) - d_{\text{uc}}\right)^T C_D^{-1}\left(g(m) - d_{\text{uc}}\right) , \tag{2.8}$$

where, compared with Eq. 2.7, m_{prior} and d_{obs} are replaced with m_{uc} and d_{uc};

Step 3 If the number of conditional realizations meets requirement, go to **Step 4**; otherwise, go to **Step 1**;

Step 4 Run reservoir simulator using the conditional realizations and conduct uncertainty analysis.

The unconditional realizations of model parameters and data can be generated a few different ways. One way to generate realizations from a Gaussian PDF with mean m_{prior} and model covariance C_M is

$$m_{\text{uc}} = m_{\text{prior}} + LZ\,, \tag{2.9}$$

where Z is a random vector sampled from $N(0,1)$ and L is lower triangular part of the Cholesky decomposition of the model covariance matrix C_M, which is

$$LL^T = C_M\,. \tag{2.10}$$

Similarly, unconditional realization of data is,

$$d_{\text{uc}} = d_{\text{obs}} + L_D Z\,, \tag{2.11}$$

where Z is also a random vector sampled from $N(0,1)$ and L_D is

$$L_D L_D^T = C_D\,. \tag{2.12}$$

One major drawback of this method is that when model size becomes large, the Cholesky decomposition of the model covariance matrix is not computationally feasible. Oliver (1995) gave a very efficient moving average method to generate unconditional realizations for large scale models. Sequential Gaussian Simulation (SGS) (Deutsch and Journel, 1992) and Sequential Gaussian Co-Simulation (SGCS) are other two frequently used algorithms. The SGS can be used to generate realizations for one parameter, for example, permeability, while the SGCS is often used to generate realizations for multiple parameters, which have correlations with each other.

2.2 Adjoint method

Using the Bayesian framework, automatic history matching can be transformed into a minimization problem, which leads to either a MAP estimate or multiple realizations. Efficient minimization of the objective function in Eq. 2.7 then becomes into the important aspect. As introduced in Chapter 1, the LBFGS method is employed for minimization. The LBFGS method requires only the gradient of the objective function. Therefore, the key point is to calculate the gradient efficiently. Compared with other methods, the adjoint method is more efficient in computing the gradient, especially when both model size and the number of data are large. Since the adjoint method is closely related to the simulation system, the principles of reservoir simulator will be covered before introducing the adjoint equations.

2.2.1 Reservoir simulation equations

Suppose that the reservoir under study is rectangularly shaped, occupying volume Ω,

$$\Omega = \{(x, y, z) \mid 0 < x < L_x, 0 < y < L_y, 0 < z < L_z\} \ , \tag{2.13}$$

where L_x, L_y, and L_z are reservoir lengths along x, y, and z directions respectively. In this reservoir, there are multiple fluid phases in the porous rocks. By applying mass balance, momentum balance, and energy balance relationships, a set of partial

differential equations governing the fluid flow in porous media can be achieved,

$$\begin{aligned}
\nabla \cdot \left[\frac{k k_{ro}}{B_o \mu_o} \left(\nabla p_o - \gamma_o \nabla D \right) \right] + q_o &= \frac{\partial}{\partial t} \left(\frac{\phi S_o}{B_o} \right) \\
\nabla \cdot \left[\frac{k k_{rw}}{B_w \mu_w} \left(\nabla p_w - \gamma_w \nabla D \right) \right] + q_w &= \frac{\partial}{\partial t} \left(\frac{\phi S_w}{B_w} \right) \\
\nabla \cdot \left[\frac{k k_{rg}}{B_g \mu_g} \left(\nabla p_g - \gamma_g \nabla D \right) + \frac{R_s k k_{ro}}{B_o \mu_o} \left(\nabla p_o - \gamma_o \nabla D \right) \right] + q_g &= \frac{\partial}{\partial t} \left[\phi \left(\frac{R_s S_o}{B_o} + \frac{S_g}{B_g} \right) \right] ,
\end{aligned} \tag{2.14}$$

where,

- o, g, and w stand for oil phase, gas phase, and water phase respectively;
- k_r is relative permeability;
- k is permeability of rocks;
- B is formation volume factor;
- μ is viscosity;
- p is pressure;
- γ is specific gravity;
- D is vertical distance from datum level;
- q is production rate;
- R_s is solution gas oil ratio;
- ϕ is porosity;
- S is saturation.

The derivation of Eq. 2.14 uses the **black oil** model, which assumes that the only fluid phases are oil, gas, and water, gas can dissolve into oil but oil can not be vaporized into gas, water and oil are immiscible. Although the pressures in each phase may be

different due to capillary pressure, in this work, capillary pressure is assumed to be negligible.

Since the PDEs in Eq. 2.14 are non-linear, it is difficult to solve them analytically. If finite difference approximation is applied to Eq. 2.14, the reservoir volume Ω will have N_x, N_y and N_z gridblocks along x, y and z directions respectively, and at each of $N_b = N_x \times N_y \times N_z$ gridblocks, there are 3 finite difference equations for oil, gas, and water. Totally, there will be $3N_b$ equations representing the mass balance in all gridblocks. In addition, N_w well equations will be added if there are N_w wells. Each well can have different constraint, such as constant bottomhole pressure, constant oil production rate, and constant total production rate. If bottomhole pressure is applied as a constraint in wells, the corresponding phase production rate can be computed using the Peaceman equation (Peaceman, 1983). These $3N_b + N_w$ equations plus appropriate discretized boundary and initial conditions consist of a complete set of reservoir simulation equations. The solution of the system for pressure and saturation distributions of each phase in each grid at different times is called reservoir simulation. The reservoir simulator used here is a fully-implicit, 3-D, 3-phase, black oil simulator provided by Chevron-Texaco, named CLASS (**C**hevron **L**imited **A**pplication **S**imulation **S**ystem).

For the ith gridblock, the three finite difference equations can be generally written as, $f^n_{m,i} = 0$, where $m = o, g, w$ and n is the time index. The flow equations are solved at discrete times, i.e., $t^{n+1} = t^n + \triangle t^n$. The primary variables to be solved in each gridblock are case dependent. CLASS can alter them automatically according to phase changes. For example, p, S_o, and S_g are typically primary variables in a 3-phase system, but if no free gas is present, solution gas oil ratio, R_s, replaces S_g as one of the primary variables. Table 2.1 shows how equations and primary variables change with difference phase combination (Zhang, 2002). In the table, "Sum" means that the equation $f^n_{s,i} = f^n_{o,i} + f^n_{g,i} + f^n_{w,i} = 0$ is solved.

Phases		Equations	Unknowns	Auxiliary Equations
O-W-G	$S_g > 0$	Sum, Oil, Gas	p,S_o,S_g	$S_w = 1 - S_o - S_g$; R_s from PVT table
	$S_g = 0$	Sum, Oil, Gas	p,S_o,R_s	$S_w = 1 - S_o - S_g$
O-W		Sum, Oil	p,S_o	$S_w = 1 - S_o$; R_s from PVT table
W-G		Sum, Gas	p,S_g	$S_w = 1 - S_g$
O-G	$S_g > 0$	Sum, Gas	p,S_g	$S_o = 1 - S_g$; R_s from PVT table
	$S_g = 0$	Sum, Gas	p,R_s	$S_o = 1 - S_g$

Table 2.1: Equations and primary variables for different phase combinations

At time step n, let y^n denote the primary variable vector,

$$y^n = \left[p_1^n, \quad S_{o,1}^n, \quad S_{g,1}^n, \quad p_2^n, \quad \cdots \quad S_{g,N_b}^n, \quad p_{wf,1}^n, \quad \cdots \quad p_{wf,N_w}^n \right]^T , \tag{2.15}$$

where N_b is the number of gridblocks, N_w is the number of wells, P_{wf} is bottomhole pressure, and S_g will be replaced with R_s if necessary. The simulation equations can be concisely written as

$$f^{n+1} = f(y^{n+1}, y^n, m) = \begin{bmatrix} f_{s,1}^{n+1} \\ f_{o,1}^{n+1} \\ f_{g,1}^{n+1} \\ f_{s,2}^{n+1} \\ \vdots \\ f_{g,N_b}^{n+1} \\ f_{wf,1}^{n+1} \\ \vdots \\ f_{wf,N_w}^{n+1} \end{bmatrix} , \tag{2.16}$$

where m is the vector of model parameters, f_{wf} is well equation, and $f_s = f_o + f_g + f_w$. Eq. 2.16 can be solved using the Newton-Raphson method (Aziz and Settari, 1979),

$$J^{n,k} \delta y^{n,k+1} = -f^{n,k} \tag{2.17}$$

$$y^{n,k+1} = y^{n,k} + \delta y^{n,k+1} , \tag{2.18}$$

where k is the Newton-Raphson iteration index, n is time step index, and $J^{n,k}$ is the Jacobian matrix,

$$J^{n,k} = \left[\nabla_{y^n} \left(f^n\right)^T\right]^T_{y^{n,k}} . \tag{2.19}$$

2.2.2 Adjoint equations

If a general scalar function is defined as

$$\beta = \beta(y^1, \cdots, y^L, m) , \tag{2.20}$$

where $1, \cdots, L$ corresponds to a series of time steps, y is the vector of primary variables defined in Eq. 2.15, and m is the vector of model parameters, the sensitivity of β with respect to model parameters m can be computed as following.

First of all, a new functional J is formed by adding a linear combination of the constraints to the functional β:

$$J = \beta + \sum_{n=0}^{L} (\lambda^{n+1})^T f^{n+1} , \tag{2.21}$$

where λ^{n+1} is the vector of multipliers, which are called the adjoint variables here. In vector form, it is

$$\lambda^{n+1} = \left[\lambda_1^{n+1}, \quad \lambda_2^{n+1}, \quad \ldots, \quad \lambda_{3N_b+N_w}^{n+1}\right]^T , \tag{2.22}$$

where $3N_b$ means that each gridblock has three adjoint variables for equations f_s, f_o and f_g respectively. Taking the total differential on Eq. 2.21 leads to

$$\begin{aligned} dJ = d\beta &+ \sum_{n=0}^{L} \left(\lambda^{n+1}\right)^T \left[\nabla_{y^{n+1}} \left(f^{n+1}\right)^T\right]^T dy^{n+1} + \sum_{n=0}^{L} \left(\lambda^{n+1}\right)^T \left[\nabla_{y^n} \left(f^{n+1}\right)^T\right]^T dy^n \\ &+ \sum_{n=0}^{L} \left(\lambda^{n+1}\right)^T \left[\nabla_m \left(f^{n+1}\right)^T\right]^T dm . \end{aligned} \tag{2.23}$$

The three summation terms in Eq. 2.23 start their sum index from 0. If the start

index is changed to 1, the summation terms can be written as,

$$\sum_{n=0}^{L}\left(\lambda^{n+1}\right)^{T}\left[\nabla_{y^{n+1}}\left(f^{n+1}\right)^{T}\right]^{T}dy^{n+1}=\sum_{n=1}^{L}\left(\lambda^{n}\right)^{T}\left[\nabla_{y^{n}}\left(f^{n}\right)^{T}\right]^{T}dy^{n} + \left(\lambda^{L+1}\right)^{T}\left[\nabla_{y^{L+1}}\left(f^{L+1}\right)^{T}\right]^{T}dy^{L+1}\,, \tag{2.24}$$

$$\sum_{n=0}^{L}\left(\lambda^{n+1}\right)^{T}\left[\nabla_{y^{n}}\left(f^{n+1}\right)^{T}\right]^{T}dy^{n}=\sum_{n=1}^{L}\left(\lambda^{n+1}\right)^{T}\left[\nabla_{y^{n}}\left(f^{n+1}\right)^{T}\right]^{T}dy^{n} + \left(\lambda^{1}\right)^{T}\left[\nabla_{y^{0}}\left(f^{1}\right)^{T}\right]^{T}dy^{0}\,, \tag{2.25}$$

and

$$\sum_{n=0}^{L}\left(\lambda^{n+1}\right)^{T}\left[\nabla_{m}\left(f^{n+1}\right)^{T}\right]^{T}dm=\sum_{n=1}^{L}\left(\lambda^{n}\right)^{T}\left[\nabla_{m}\left(f^{n}\right)^{T}\right]^{T}dm + \left(\lambda^{L+1}\right)^{T}\left[\nabla_{m}\left(f^{L+1}\right)^{T}\right]^{T}dm\,. \tag{2.26}$$

Inserting Eqs. 2.24, 2.25, and 2.26 into Eq. 2.23, the total differential of the functional J can be written as,

$$\begin{aligned} dJ = d\beta &+ \sum_{n=1}^{L}\left(\lambda^{n}\right)^{T}\left[\nabla_{y^{n}}\left(f^{n}\right)^{T}\right]^{T}dy^{n} + \sum_{n=1}^{L}\left(\lambda^{n+1}\right)^{T}\left[\nabla_{y^{n}}\left(f^{n+1}\right)^{T}\right]^{T}dy^{n} \\ &+ \sum_{n=1}^{L}\left(\lambda^{n}\right)^{T}\left[\nabla_{m}\left(f^{n}\right)^{T}\right]^{T}dm + \left(\lambda^{L+1}\right)^{T}\left[\nabla_{y^{L+1}}\left(f^{L+1}\right)^{T}\right]^{T}dy^{L+1} \\ &+ \left(\lambda^{1}\right)^{T}\left[\nabla_{y^{0}}\left(f^{1}\right)^{T}\right]^{T}dy^{0} + \left(\lambda^{L+1}\right)^{T}\left[\nabla_{m}\left(f^{L+1}\right)^{T}\right]^{T}dm\,. \end{aligned} \tag{2.27}$$

Since the scalar function β depends on m and y at different time steps from 1 to L, its total differential is

$$d\beta=\sum_{n=1}^{L}\left[\nabla_{y^{n}}\beta\right]^{T}dy^{n}+\left[\nabla_{m}\beta\right]^{T}dm\,. \tag{2.28}$$

At time step 0, the primary variables y are equal to initial conditions, so the total differential of y at time step 0 is zero,

$$dy^{0}=0\,. \tag{2.29}$$

L denotes the last time step in forward simulation run. At $L+1$ step, the adjoint variables λ achieve their initial values, which are chosen to be 0s,

$$\lambda^{L+1}=0\,. \tag{2.30}$$

Inserting Eq. 2.28 into Eq. 2.27 with two conditions in Eq. 2.30 and Eq. 2.29 applied, the total differential of J becomes into,

$$\begin{aligned} dJ &= \sum_{n=1}^{L} (\lambda^n)^T \left[\nabla_{y^n} (f^n)^T\right]^T dy^n + \sum_{n=1}^{L} \left(\lambda^{n+1}\right)^T \left[\nabla_{y^n} \left(f^{n+1}\right)^T\right]^T dy^n \\ &\quad + \sum_{n=1}^{L} \left[\nabla_{y^n}\beta\right]^T dy^n + \sum_{n=1}^{L} (\lambda^n)^T \left[\nabla_m (f^n)^T\right]^T dm + \left[\nabla_m \beta\right]^T dm \\ &= \sum_{n=1}^{L} \left\{ (\lambda^n)^T \left[\nabla_{y^n} (f^n)^T\right]^T + \left(\lambda^{n+1}\right)^T \left[\nabla_{y^n} \left(f^{n+1}\right)^T\right]^T + \left[\nabla_{y^n}\beta\right]^T \right\} dy^n \\ &\quad + \sum_{n=1}^{L} (\lambda^n)^T \left[\nabla_m (f^n)^T\right]^T dm + \left[\nabla_m \beta\right]^T dm \,. \end{aligned} \tag{2.31}$$

Only the last two terms in Eq. 2.31 are related to the derivatives of the functional J with respect to the model parameters m, so the first term in Eq. 2.31 need to be cancelled out by setting all terms multiplied by dy^n equal to zero, which gives the adjoint equations,

$$(\lambda^n)^T \left[\nabla_{y^n} (f^n)^T\right]^T + \left(\lambda^{n+1}\right)^T \left[\nabla_{y^n} \left(f^{n+1}\right)^T\right]^T + \left[\nabla_{y^n}\beta\right]^T = 0 \,. \tag{2.32}$$

Rearranging Eq. 2.32 gives a solvable form as shown in Eq. 2.33,

$$\left[\nabla_{y^n} (f^n)^T\right] \lambda^n = - \left[\nabla_{y^n} \left(f^{n+1}\right)^T\right] \lambda^{n+1} - \nabla_{y^n}\beta \,. \tag{2.33}$$

Eq. 2.33 is solved for λ from time step $L+1$ to 0 using the initial conditions defined in Eq. 2.30. Since the coefficient matrix in the left hand side of Eq. 2.33 is independent of the adjoint variable λ, the adjoint equations are linear. It should cost less to solve the adjoint equations than to solve the forward reservoir simulation equations, for which iterations are required at each time step. In form, the coefficient matrix in Eq. 2.33 is the transpose of the Jacobian matrix in Eq. 2.19, but only if the same system of equations are used in each gridblock for both simulation solution and adjoint solution, are these two matrices exact transposes of each other. The dimension of both $\nabla_{y^n} (f^n)^T$ and $\nabla_{y^n} (f^{n+1})^T$ are $(3N_b+N_w)\times(3N_b+N_w)$. $\nabla_{y^n}\beta$ is a vector with length equal to $3N_b + N_w$.

After the adjoint variables are obtained, the total differential of J can be obtained from

$$dJ = [\nabla_m \beta]^T \, dm + \sum_{n=1}^{L} (\lambda^n)^T \left[\nabla_m \left(f^n\right)^T\right]^T dm \,. \tag{2.34}$$

Since $dJ = [\nabla_m J]^T dm$, the derivatives of the functional J with respect to model parameters m are

$$\nabla_m J = \nabla_m \beta + \sum_{n=1}^{L} \left[\nabla_m \left(f^n\right)^T\right] \lambda^n \,. \tag{2.35}$$

The typical length of $\nabla_m \beta$ is $2N_b$ if porosity and horizontal permeability in each gridblock are model parameters. Correspondingly, the dimension of $\nabla_m \left(f^n\right)^T$ will be $2N_b \times (3N_b + N_w)$. Eq. 2.33 and Eq. 2.35 consist of the adjoint method for computing the gradient of the objective function.

The two gradients, $\nabla_{y^n} \left(f^n\right)^T$ and $\nabla_{y^n} \left(f^{n+1}\right)^T$, are derivatives of the flow equations (Eq. 2.16) with respect to the primary variables (Eq. 2.15), computed at all time steps that the forward simulation run uses. Although the adjoint solution does not necessarily use the same time step as the simulation, in this work, same time steps were used at both forward and backward solutions. In detailed form, if the primary variables are p, S_o, and S_g, then

$$\nabla_{y^n} [f^n]^T = \begin{bmatrix} \frac{\partial f^n_{s,1}}{\partial p^n_1} & \frac{\partial f^n_{o,1}}{\partial p^n_1} & \cdots & \frac{\partial f^n_{g,N_b}}{\partial p^n_1} & \frac{\partial f^n_{wf,1}}{\partial p^n_1} & \cdots & \frac{\partial f^n_{wf,N_w}}{\partial p^n_1} \\ \frac{\partial f^n_{s,1}}{\partial S^n_{o,1}} & \frac{\partial f^n_{o,1}}{\partial S^n_{o,1}} & \cdots & \frac{\partial f^n_{g,N_b}}{\partial S^n_{o,1}} & \frac{\partial f^n_{wf,1}}{\partial S^n_{o,1}} & \cdots & \frac{\partial f^n_{wf,N_w}}{\partial S^n_{o,1}} \\ \frac{\partial f^n_{s,1}}{\partial S^n_{g,1}} & \frac{\partial f^n_{o,1}}{\partial S^n_{g,1}} & \cdots & \frac{\partial f^n_{g,N_b}}{\partial S^n_{g,1}} & \frac{\partial f^n_{wf,1}}{\partial S^n_{g,1}} & \cdots & \frac{\partial f^n_{wf,N_w}}{\partial S^n_{g,1}} \\ \frac{\partial f^n_{s,1}}{\partial p^n_2} & \frac{\partial f^n_{o,1}}{\partial p^n_2} & \cdots & \frac{\partial f^n_{g,N_b}}{\partial p^n_2} & \frac{\partial f^n_{wf,1}}{\partial p^n_2} & \cdots & \frac{\partial f^n_{wf,N_w}}{\partial p^n_2} \\ \vdots & \vdots & \cdots & \vdots & \vdots & \cdots & \vdots \\ \frac{\partial f^n_{s,1}}{\partial S^n_{g,N_b}} & \frac{\partial f^n_{o,1}}{\partial S^n_{g,N_b}} & \cdots & \frac{\partial f^n_{g,N_b}}{\partial S^n_{g,N_b}} & \frac{\partial f^n_{wf,1}}{\partial S^n_{g,N_b}} & \cdots & \frac{\partial f^n_{wf,N_w}}{\partial S^n_{g,N_b}} \\ \frac{\partial f^n_{s,1}}{\partial p^n_{wf,1}} & \frac{\partial f^n_{o,1}}{\partial p^n_{wf,1}} & \cdots & \frac{\partial f^n_{g,N_b}}{\partial p^n_{wf,1}} & \frac{\partial f^n_{wf,1}}{\partial p^n_{wf,1}} & \cdots & \frac{\partial f^n_{wf,N_w}}{\partial p^n_{wf,1}} \\ \vdots & \vdots & \cdots & \vdots & \vdots & \cdots & \vdots \\ \frac{\partial f^n_{s,1}}{\partial p^n_{wf,N_w}} & \frac{\partial f^n_{o,1}}{\partial p^n_{wf,N_w}} & \cdots & \frac{\partial f^n_{g,N_b}}{\partial p^n_{wf,N_w}} & \frac{\partial f^n_{wf,1}}{\partial p^n_{wf,N_w}} & \cdots & \frac{\partial f^n_{wf,N_w}}{\partial p^n_{wf,N_w}} \end{bmatrix}, \tag{2.36}$$

and

$$\nabla_{y^n}\left[f^{n+1}\right]^T = \begin{bmatrix} \frac{\partial f_{s,1}^{n+1}}{\partial p_1^n} & \frac{\partial f_{o,1}^{n+1}}{\partial p_1^n} & \cdots & \frac{\partial f_{g,N_b}^{n+1}}{\partial p_1^n} & \frac{\partial f_{wf,1}^{n+1}}{\partial p_1^n} & \cdots & \frac{\partial f_{wf,N_w}^{n+1}}{\partial p_1^n} \\ \frac{\partial f_{s,1}^{n+1}}{\partial S_{o,1}^n} & \frac{\partial f_{o,1}^{n+1}}{\partial S_{o,1}^n} & \cdots & \frac{\partial f_{g,N_b}^{n+1}}{\partial S_{o,1}^n} & \frac{\partial f_{wf,1}^{n+1}}{\partial S_{o,1}^n} & \cdots & \frac{\partial f_{wf,N_w}^{n+1}}{\partial S_{o,1}^n} \\ \frac{\partial f_{s,1}^{n+1}}{\partial S_{g,1}^n} & \frac{\partial f_{o,1}^{n+1}}{\partial S_{g,1}^n} & \cdots & \frac{\partial f_{g,N_b}^{n+1}}{\partial S_{g,1}^n} & \frac{\partial f_{wf,1}^{n+1}}{\partial S_{g,1}^n} & \cdots & \frac{\partial f_{wf,N_w}^{n+1}}{\partial S_{g,1}^n} \\ \frac{\partial f_{s,1}^{n+1}}{\partial p_2^n} & \frac{\partial f_{o,1}^{n+1}}{\partial p_2^n} & \cdots & \frac{\partial f_{g,N_b}^{n+1}}{\partial p_2^n} & \frac{\partial f_{wf,1}^{n+1}}{\partial p_2^n} & \cdots & \frac{\partial f_{wf,N_w}^{n+1}}{\partial p_2^n} \\ \vdots & \vdots & \cdots & \vdots & \vdots & \cdots & \vdots \\ \frac{\partial f_{s,1}^{n+1}}{\partial S_{g,N_b}^n} & \frac{\partial f_{o,1}^{n+1}}{\partial S_{g,N_b}^n} & \cdots & \frac{\partial f_{g,N_b}^{n+1}}{\partial S_{g,N_b}^n} & \frac{\partial f_{wf,1}^{n+1}}{\partial S_{g,N_b}^n} & \cdots & \frac{\partial f_{wf,N_w}^{n+1}}{\partial S_{g,N_b}^n} \\ \frac{\partial f_{s,1}^{n+1}}{\partial p_{wf,1}^n} & \frac{\partial f_{o,1}^{n+1}}{\partial p_{wf,1}^n} & \cdots & \frac{\partial f_{g,N_b}^{n+1}}{\partial p_{wf,1}^n} & \frac{\partial f_{wf,1}^{n+1}}{\partial p_{wf,1}^n} & \cdots & \frac{\partial f_{wf,N_w}^{n+1}}{\partial p_{wf,1}^n} \\ \vdots & \vdots & \cdots & \vdots & \vdots & \cdots & \vdots \\ \frac{\partial f_{s,1}^{n+1}}{\partial p_{wf,N_w}^n} & \frac{\partial f_{o,1}^{n+1}}{\partial p_{wf,N_w}^n} & \cdots & \frac{\partial f_{g,N_b}^{n+1}}{\partial p_{wf,N_w}^n} & \frac{\partial f_{wf,1}^{n+1}}{\partial p_{wf,N_w}^n} & \cdots & \frac{\partial f_{wf,N_w}^{n+1}}{\partial p_{wf,N_w}^n} \end{bmatrix}. \tag{2.37}$$

To compute each entry of those two matrices, the pressure and saturation at each gridblock during forward simulation run are saved at each time step. When the model size is large, the variables are stored in hard disk instead of memory but the reduction in computation speed due to I/O operations was not substantial (Zhang, 2002). The equations for each entry are fully consistent with the equations used in CLASS and can be found in Li (2001).

In Eq. 2.35, the gradient of the flow equations with respect to model parameters m is

$$\nabla_m[f^n]^T = \begin{bmatrix} \frac{\partial f_{s,1}^n}{\partial m_1} & \frac{\partial f_{o,1}^n}{\partial m_1} & \frac{\partial f_{g,1}^n}{\partial m_1} & \cdots & \frac{\partial f_{g,N_b}^n}{\partial m_1} & \frac{\partial f_{wf,1}^n}{\partial m_1} & \cdots & \frac{\partial f_{wf,N_w}^n}{\partial m_1} \\ \frac{\partial f_{s,1}^n}{\partial m_2} & \frac{\partial f_{o,1}^n}{\partial m_2} & \frac{\partial f_{g,1}^n}{\partial m_2} & \cdots & \frac{\partial f_{g,N_b}^n}{\partial m_2} & \frac{\partial f_{wf,1}^n}{\partial m_2} & \cdots & \frac{\partial f_{wf,N_w}^n}{\partial m_2} \\ \vdots & \vdots & \vdots & \vdots & \vdots & \vdots & \vdots & \vdots \\ \frac{\partial f_{s,1}^n}{\partial m_{N_m}} & \frac{\partial f_{o,1}^n}{\partial m_{N_m}} & \frac{\partial f_{g,1}^n}{\partial m_{N_m}} & \cdots & \frac{\partial f_{g,N_b}^n}{\partial m_{N_m}} & \frac{\partial f_{wf,1}^n}{\partial m_{N_m}} & \cdots & \frac{\partial f_{wf,N_w}^n}{\partial m_{N_m}} \end{bmatrix}, \tag{2.38}$$

where N_m is the number of model parameters, which is equal to $2N_b$ if porosity and horizontal permeability at each gridblock are to be estimated. The equations for each entry can also be found in Li (2001).

In Eq. 2.33,$\nabla_{y^n}\beta$ is called the source term. In matrix form, it is,

$$\nabla_{y^n}\beta = \left[\frac{\partial\beta}{\partial p_1^n},\ \frac{\partial\beta}{\partial S_{o,1}^n},\ \frac{\partial\beta}{\partial S_{g,1}^n},\ \frac{\partial\beta}{\partial p_2^n},\ \cdots\ \frac{\partial\beta}{\partial S_{g,N_b}^n},\ \frac{\partial\beta}{\partial p_{wf,1}^n},\ \cdots\ \frac{\partial\beta}{\partial p_{wf,N_w}^n}\right]^T. \quad (2.39)$$

$\nabla_m\beta$ in Eq. 2.35 is

$$\nabla_m\beta = \left[\frac{\partial\beta}{\partial m_1},\ \frac{\partial\beta}{\partial m_2},\ \cdots\ \frac{\partial\beta}{\partial m_{N_m}}\right]^T. \quad (2.40)$$

It is the direct dependence of β on model parameters m. In contrast, $\sum_{n=1}^{L}\left[\nabla_m\left(f^n\right)^T\right]\lambda^n$ reflects the implicit dependence inherited from flow equations. If model parameters are not explicitly related to β, many (or all) entries of $\nabla_m\beta$ will become 0. For example, if GOR or WOR data are chosen as β and porosity is the only model parameter, $\nabla_m\beta$ will vanish.

If β denotes individual data points at different time steps, solving Eq. 2.33 and Eq. 2.35 provides the sensitivity of the datum with respect to model parameters, such as, sensitivities of P_{wf}, GOR, and WOR with respect to permeability and porosity. These sensitivities are rows of the sensitivity matrix, which is used to construct the Hessian matrix in Gauss-Newton methods. For some typical types of data, the derivative equations can be found in Li (2001). Since in this work, seismic impedance change data are integrated as well as production data, the derivatives of seismic impedance change with respect to the primary variables and model parameters are required.

As stated before, the LBFGS method is used, which does not require the Hessian matrix and sensitivities of individual data points. So the whole objective function shown in Eq. 2.7 is used as β to get the gradient of the objective function. Thus, the source term in the adjoint equation (Eq. 2.33) and the direct dependence term in Eq. 2.35 change into

$$\begin{aligned}\nabla_{y^n}\beta &= \nabla_{y^n}\left\{\frac{1}{2}\left(g(m)-d_{\text{obs}}\right)^T C_D^{-1}\left(g(m)-d_{\text{obs}}\right)\right\}\\ &= \left[\nabla_{y^n}\left(g(m)-d_{\text{obs}}\right)^T\right] C_D^{-1}\left(g(m)-d_{\text{obs}}\right)\\ &= \nabla_{y^n}\left[g(m)\right]^T C_D^{-1}\left(g(m)-d_{\text{obs}}\right),\end{aligned} \quad (2.41)$$

and

$$\begin{aligned}\nabla_m \beta &= C_M^{-1}\left(m - m_{\text{prior}}\right) + \nabla_m \left\{\frac{1}{2}\left(g(m) - d_{\text{obs}}\right)^T C_D^{-1}\left(g(m) - d_{\text{obs}}\right)\right\} \\ &= C_M^{-1}\left(m - m_{\text{prior}}\right) + \left[\nabla_m \left(g(m) - d_{\text{obs}}\right)^T\right] C_D^{-1}\left(g(m) - d_{\text{obs}}\right) \\ &= C_M^{-1}\left(m - m_{\text{prior}}\right) + \nabla_m \left[g(m)\right]^T C_D^{-1}\left(g(m) - d_{\text{obs}}\right) .\end{aligned} \tag{2.42}$$

$\nabla_{y^n}\left[g(m)\right]^T$ and $\nabla_m\left[g(m)\right]^T$ in Eq. 2.41 and Eq. 2.42 are

$$\nabla_{y^n}\left[g(m)\right]^T = \begin{bmatrix} \frac{\partial g_1}{\partial p_1^n} & \frac{\partial g_2}{\partial p_1^n} & \cdots & \frac{\partial g_{N_d}}{\partial p_1^n} \\ \frac{\partial g_1}{\partial S_{o,1}^n} & \frac{\partial g_2}{\partial S_{o,1}^n} & \cdots & \frac{\partial g_{N_d}}{\partial S_{o,1}^n} \\ \frac{\partial g_1}{\partial S_{g,1}^n} & \frac{\partial g_2}{\partial S_{g,1}^n} & \cdots & \frac{\partial g_{N_d}}{\partial S_{g,1}^n} \\ \frac{\partial g_1}{\partial p_2^n} & \frac{\partial g_2}{\partial p_2^n} & \cdots & \frac{\partial g_{N_d}}{\partial p_2^n} \\ \vdots & \vdots & \cdots & \vdots \\ \frac{\partial g_1}{\partial S_{g,N_b}^n} & \frac{\partial g_2}{\partial S_{g,N_b}^n} & \cdots & \frac{\partial g_{N_d}}{\partial S_{g,N_b}^n} \\ \frac{\partial g_1}{\partial p_{wf,1}^n} & \frac{\partial g_2}{\partial p_{wf,1}^n} & \cdots & \frac{\partial g_{N_d}}{\partial p_{wf,1}^n} \\ \vdots & \vdots & \cdots & \vdots \\ \frac{\partial g_1}{\partial p_{wf,N_w}^n} & \frac{\partial g_2}{\partial p_{wf,N_w}^n} & \cdots & \frac{\partial g_{N_d}}{\partial p_{wf,N_w}^n} \end{bmatrix}, \tag{2.43}$$

and

$$\nabla_m[g(m)]^T = \begin{bmatrix} \frac{\partial g_1}{\partial m_1} & \frac{\partial g_2}{\partial m_1} & \cdots & \frac{\partial g_{N_d}}{\partial m_1} \\ \frac{\partial g_1}{\partial m_2} & \frac{\partial g_2}{\partial m_2} & \cdots & \frac{\partial g_{N_d}}{\partial m_2} \\ \vdots & \vdots & \cdots & \vdots \\ \frac{\partial g_1}{\partial m_{N_m}} & \frac{\partial g_2}{\partial m_{N_m}} & \cdots & \frac{\partial g_{N_d}}{\partial m_{N_m}} \end{bmatrix}, \tag{2.44}$$

where N_d is the number of data. Each entry in the two matrices are derivatives of data with respect to the primary variables and the model parameters. The equations in Li (2001) can still be used to compute them. Although each columns of $\nabla_{y^n}\left[g(m)\right]^T$ and $\nabla_m[g(m)]^T$ are vectors shown in Eq. 2.39 and Eq. 2.40, those two matrices are never explicitly formed. Instead, $\nabla_{y^n}\left[g(m)\right]^T C_D^{-1}\left(g(m) - d_{\text{obs}}\right)$ and $\nabla_m\left[g(m)\right]^T C_D^{-1}\left(g(m) - d_{\text{obs}}\right)$ are computed. Thus, only two vectors are kept in memory (Golub and van Loan, 1989).

Seismic impedance change data are treated as two separate source terms in the adjoint equations at two different time steps, but with opposite signs. In Eq. 2.43 and Eq. 2.44, columns corresponding to seismic impedance data will be added at time steps when two seismic surveys are shot.

Before ending this chapter, a flow chart is shown in Fig. 2.1, which shows how the seismic impedance change data as well as production data are integrated into the minimization process derived from the Bayesian framework. The gradient computation comes from the adjoint method, while the search direction calculation uses the LBFGS method, which will be covered in the first part of Chapter 4.

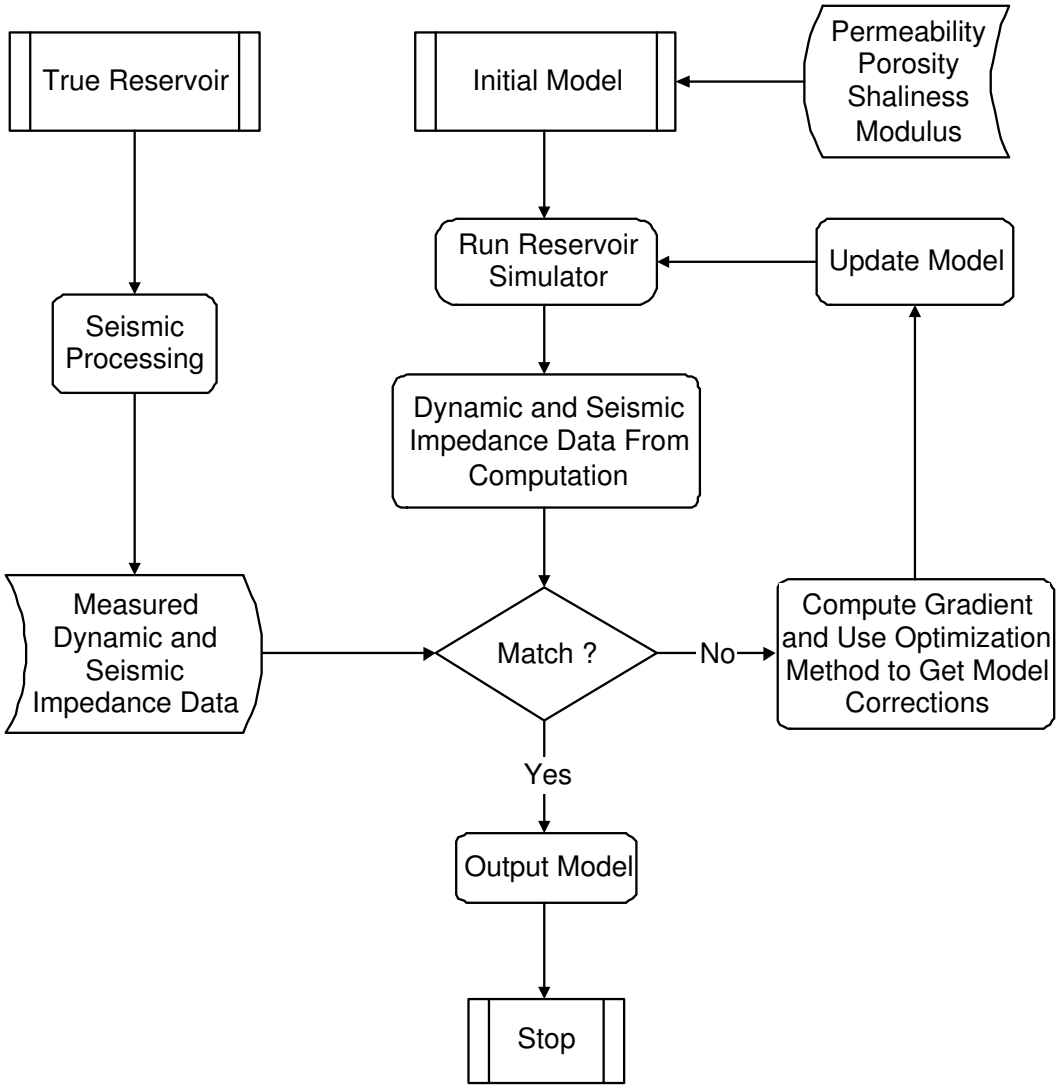

Figure 2.1: Flow chart of automatic history matching with integration of seismic impedance change data and production data

CHAPTER III

SENSITIVITY OF SEISMIC IMPEDANCE CHANGE DATA WITH RESPECT TO POROSITY AND PERMEABILITY

Since the LBFGS method does not require the Hessian matrix, the sensitivity of individual seismic impedance change datum with respect to model parameters, such as permeability and porosity, is not computed during the minimization process. However, given a reservoir model, computation of sensitivities of seismic data with respect to porosity and permeability is still sometimes useful,

- To investigate how the sensitivity coefficients are distributed around the location where the seismic datum is recorded;
- To calibrate with the sensitivity coefficients computed using the perturbation method, which can check if the derivatives of rock physics models are calculated correctly.

To better understand the information from time-lapse seismic, before conducting history matching case study, the sensitivity coefficients of seismic impedance change data with respect to porosity and permeability are computed based on a small 2-D synthetic model. It will be seen that the sensitivities of time-lapse seismic data (impedance changed data) to porosity and permeability have vastly different magnitudes. The relative error between the sensitivities computed from the adjoint method and from the perturbation method is small.

This chapter will start with a introduction of seismic impedance and time-lapse seismic, then the derivatives of different rock physics models are followed, finally the sensitivity coefficient plots are shown.

3.1 Seismic impedance

Although amplitude data are preferred for interpreting geologic structure, they depend on both reflectivities among layers and on the source properties for the signal. In this dissertation, seismic impedance is the attribute that will be used for estimation of flow properties. Qualitatively, it indicates how stiff rocks are, high impedance if rocks are hard to compress and low impedance if rocks are soft. Because of fluid production, pressure and saturation distributions will change, which can alter the distribution of elastic properties of rocks, especially when the reservoir experiences changes from no gas exist to free gas. Such changes in elastic properties can be captured through changes in seismic impedance data. On the other hand, pressure and saturation distributions are determined primarily by permeability and porosity. Hence, seismic impedance data have a strong relationship with permeability and porosity.

Seismic impedance usually refers to P-wave impedance, which is defined as

$$Z = \rho V_p \,, \tag{3.1}$$

where ρ is body density and V_p is P-wave velocity. Since only P-wave impedance data is used in this work, the term "seismic impedance" will be used exclusively hereafter. The P-wave velocity is

$$V_p = \sqrt{\frac{1}{\rho}\left(K + \frac{4}{3}G\right)} \,, \tag{3.2}$$

where K is the bulk modulus and G is the shear modulus. The bulk modulus can be regarded as the reciprocal of compressibility. For stiff rocks, the bulk modulus has large value. The shear modulus is the coefficient between shear strain and shear stress.

Besides the P-wave, another type of wave that is commonly met in geophysics is called the shear wave, also denoted as S-wave. The propagation direction of the shear wave is perpendicular to its vibration direction. The shear wave velocity is

$$V_s = \sqrt{\frac{G}{\rho}}\,. \tag{3.3}$$

Using Eq. 3.2 and Eq. 3.3 into Eq. 3.1, a new equation for impedance calculation can be written as in Eq. 3.4,

$$Z = \rho V_p = \sqrt{\rho\left(K + \frac{4}{3}G\right)} = \sqrt{\rho K + \frac{4}{3}\rho^2 V_s^2}\,. \tag{3.4}$$

From Eq. 3.4, it can be seen that to compute the seismic impedance, two groups of parameters are required, either ρ, K and G or ρ, K and V_s. The bulk density ρ is related to porosity and saturations using Eq. 3.5,

$$\rho = \left(\rho_o S_o + \rho_g S_g + \rho_w (1.0 - S_o - S_g)\right)\phi + (1-\phi)\,\rho_{\text{solid}}\,, \tag{3.5}$$

where S_o, S_g, and S_w are saturations of oil, gas, and water, ρ_o, ρ_g, and ρ_w are densities of oil, gas, and water, ρ_{solid} is dry rock density, and ϕ is porosity. For the bulk modulus K, the well known Gassmann equations are frequently used (Gassmann, 1951). The shear modulus G and shear wave velocity V_s can be calculated using empirical formulas, such as Han equation (Han et al., 1986), Kuster and Toksöz equation (Kuster and Toksöz, 1974), and Ramammorthy equation (Ramammorthy et al., 1995). Other equations can be found in Guerin (2000).

3.1.1 Gassmann equations

The Gassmann equations (Gassmann, 1951) divide the bulk modulus of a fluid saturated rock into three parts: the bulk modulus of components in the rock, the bulk modulus of the rock's dry frame, and the bulk modulus of fluids in the rock's pores. According to Murphy et al. (1993) and Nolen-Hoeksema (2000), the Gassmann formula is a low frequency approximation of the **Biot** theory (Biot, 1956a,b, 1962). The

Gassmann equations for bulk modulus are

$$K = K_{\text{grain}} \frac{K_{\text{frame}} + Q}{K_{\text{grain}} + Q}, \tag{3.6}$$

and

$$Q = \frac{K_{\text{fluid}} \left(K_{\text{grain}} - K_{\text{frame}}\right)}{\phi \left(K_{\text{grain}} - K_{\text{fluid}}\right)}, \tag{3.7}$$

where, K_{grain} is the bulk modulus of grain (matrix components), K_{frame} is the bulk modulus of the porous dry frame, and K_{fluid} is the bulk modulus of the pore fluid. Some assumptions of the Gassmann equations are (Smith et al., 2003; Wang, 2001),

- Rocks are homogeneous and isotropic;
- Pores in rocks are connected and have good communication;
- Wave frequency is low enough to achieve equilibrium;
- Viscosities of the fluids are negligible;
- No chemical effects between fluids and rock frames.

Some assumptions listed above are generally satisfied, for example, the low wave frequency assumption, which is generally true in seismic exploration due to the attenuation of high-frequency wave components. Other assumptions, however, may not be valid in real application. Although moderate deviations from them may not result in invalidation of the model, some caution is worthwhile. First, if rocks consist of different minerals with very strong contrasts in their elastic properties, or with obvious heterogeneous alignments, the Gassmann equations tend to be poor models (Smith et al., 2003). Secondly, the Gassmann equations do not specify pore shapes, but they are not appropriate if pores are anisotropic within rocks. Moreover, if the Gassmann equations are applied to rocks with very low porosity, the reduction in accuracy may be expected (Smith et al., 2003; Wang, 2001).

The bulk modulus of fluid can be computed using Eq. 3.8,

$$\frac{1}{K_{\text{fluid}}} = \frac{1.0 - S_o - S_g}{K_w} + \frac{S_g}{K_g} + \frac{S_o}{K_o}\,, \tag{3.8}$$

where K_o, K_g, and K_w are bulk modulli of oil, gas, and water, and S_o, S_g, and S_w are oil, gas, and water saturations. The bulk modulli of oil, gas, and water are reciprocals of their isothermal compressibilities. The general definition of isothermal compressibility is

$$\frac{1}{K} = c = -\frac{1}{V}\frac{dV}{dP}\,. \tag{3.9}$$

So the PVT tables input into the reservoir simulator can be used to compute the bulk modulus of pore fluid. Correlation equations are frequently used to calculate the bulk modulus of pore fluid (Batzle and Wang, 1992). Usually, the magnitude of K_g is two orders of magnitude smaller than K_o and K_w. Since the bulk modulus of the fluid is a geometric mean of the bulk modulus of individual phase, a small amount of gas saturation change can lead to a large change in the bulk modulus of fluid.

The bulk modulus of grain takes into account bulk modulli of different minerals in rocks, usually averaging according to their percentage in rocks. One widely used average method is called the **Voight-Reuss-Hill** (VRH) average (Hill, 1952; Smith et al., 2003; Wang, 2001), which is

$$K_{\text{grain}} = \frac{1}{2}\left(K_{\text{grain,V}} + K_{\text{grain,R}}\right)\,, \tag{3.10}$$

where $K_{\text{grain,V}}$ is the bulk modulus of grain computed using the Voight average (Voight, 1928) and $K_{\text{grain,R}}$ is the bulk modulus of grain computed using the Reuss average (Reuss, 1929). Respectively, they are

$$K_{\text{grain,V}} = \sum_{i=1}^{n} c_i K_i\,, \tag{3.11}$$

and

$$\frac{1}{K_{\text{grain,R}}} = \frac{c_i}{K_i}\,, \tag{3.12}$$

where c_i is the volume percentage of each mineral and K_i is the bulk modulus, correspondingly. If it is assumed that rocks mainly consist of sand and clay, then the bulk modulus of grain can be calculated using Eq. 3.13,

$$K_{\text{grain}} = \frac{1}{2}\left[\gamma K_c + (1-\gamma)K_s + \frac{K_s K_c}{K_s\gamma + K_c(1-\gamma)}\right], \tag{3.13}$$

where K_s is the bulk modulus of sand, K_c is the bulk modulus of clay, and γ is the shaliness (percentage of clay). According to Dong and Oliver (2002), variations in the bulk moduli of sand and clay, and shaliness do not cause substantial deviations in seismic impedance change compared to changes caused by fluid saturation changes. Hence, for synthetic case studies, some common values of K_c, K_s, and γ are used.

The bulk modulus of dry frame can be estimated through lab measurements, logging data analysis or computed using the Gassmann equations knowing the bulk modulus of fluid saturated rock (Smith et al., 2003; Wang, 2001). In this work, an empirical equation is used (Guerin, 2000),

$$\log_{10} K_{\text{frame}} = \log_{10} K_{\text{grain}} - 4.25\phi\,, \tag{3.14}$$

where ϕ is porosity. Other equations for computing K_{frame} can be found in Smith et al. (2003) and Wang (2001).

3.1.2 Equations for G and V_s

The shear wave velocity V_s can be estimated from the porosity and shaliness using the Han equation (Han et al., 1986),

$$V_s = 3520.0 - 4910.0\phi - 1890.0\gamma\,, \tag{3.15}$$

where the unit of V_s is m/s.

The Kuster and Toksöz equation (Kuster and Toksöz, 1974) or the Ramammorthy equations (Ramammorthy et al., 1995) can be used to estimate the shear modulus G. The Kuster and Toksöz equation is

$$G = G_m \frac{(6K_m + 12G_m)\,G_i + (9K_m + 8G_m)\,((1-I_c)\,G_m + I_c G_i)}{(9K_m + 8G_m)\,G_m + (6K_m + 12G_m)\,((1-I_c)\,G_i + I_c G_m)}\,, \tag{3.16}$$

where G_m denotes the shear modulus of the matrix and G_i is the shear modulus of the inclusion. When a mixture only includes clay and sand, I_c is replaced by the shaliness, γ, and the matrix is referred to sand. Therefore, K_m and G_m are bulk modulus and shear modulus of sand. G_i is the shear modulus of clay.

The Ramammorthy equations for estimating the shear modulus are

$$G = G_{\text{grain}} \left(1 - 3.48\phi + 2.19\phi^2\right) , \tag{3.17}$$

and

$$G_{\text{grain}} = \left(0.039 \log_{10} \gamma + 0.072\right)^{-1} , \tag{3.18}$$

where G_{grain} is the shear modulus of grain, ϕ is porosity, and γ is shaliness. According to Ramammorthy et al. (1995), Eq. 3.18 is valid when γ is between 0.06 and 0.42. If γ is below 0.06, Ramammorthy et al. (1995) recommended using the following equation:

$$G = 42.65 \left(1 - 3.48\phi + 2.19\phi^2\right) , \tag{3.19}$$

where 42.65 is the shear modulus of pure quartz and the unit of G is GPa. Eq. 3.19 was first derived by Murphy et al. (1993).

3.2 Time-lapse seismic

Time-lapse seismic consists of multiple seismic surveys, which can be 2D seismic, 3D seismic, VSP, and cross-well seismic, acquired at different times but the same location. Usually, the first survey is called the base-line survey and the repeated surveys are called the monitor surveys. Seismic reflection data from one seismic survey are sensitive to both static parameters, such as lithology, porosity, and shaliness, and dynamic fluid flow related parameters, for example, permeability and porosity. If just one seismic survey is used, it is difficult to differentiate these two sources of effects. By comparing seismic data obtained from surveys at different times, it is possible to reduce the effects from static parameters and focus on dynamic changes coming

from pressure and saturation re-distributions due to production, which is the goal of automatic history matching.

The idea of time-lapse seismic can be traced back to late 1980's and early 1990's, when there were three different papers discussing how multiple seismic surveys were used to monitor reservoirs under production, by comparing data obtained from different surveys. The first two applications were to monitor steam movement in enhanced oil recovery projects (Wayland and Lee, 1986; Greaves and Fulp, 1987), where temperature changes caused easily captured seismic signal changes. A few years later, the first paper to document using time-lapse seismic to monitor fluid flow under isothermal condition appeared (Dunlop et al., 1991). Other applications to reservoir monitoring and management during the last decade can be found in Ross et al. (1996); Lumley et al. (1999); Behrens et al. (2002); Waggoner et al. (2002); Gouveia et al. (2004). Through 2001, there have been 75 active time-lapse seismic projects worldwide costing on the order of (US) $50 to (US) $100 million (Lumley, 2001).

Figs. 3.1 and 3.2 show results from a real time-lapse seismic project in Draugen field, North Sea (Koster et al., 2000). The seismic attribute displayed in the sections is impedance. In Draugen, there were two seismic surveys: the base-line survey in 1990 and the monitor survey in 1998. A green line in both monitor survey and base-line survey maps (Fig. 3.1) denotes the location of the injection well. The thick black line indicates the seal rock of the reservoir, under which is the top location of the oil layer, the thick red line in both surveys. In the base-line survey, the reflection of the reservoir top is not very strong. At some locations, it is not even continuous. After eight years production, however, the top reservoir has a very strong reflection, which comes from the replacement of oil with water. Because the bulk modulus of water is higher than that of oil, the top reservoir becomes stiffer after water flooding so the reservoir top becomes more obvious. The other parts of the reservoir show little change. By subtracting impedance volumes in the base-line survey from impedance

volumes in the monitor survey, the changes in top reservoir are emphasized with most of unchanged signals cancelled out (Fig. 3.2). The long red feature in the figure denotes the location of the seal rock.

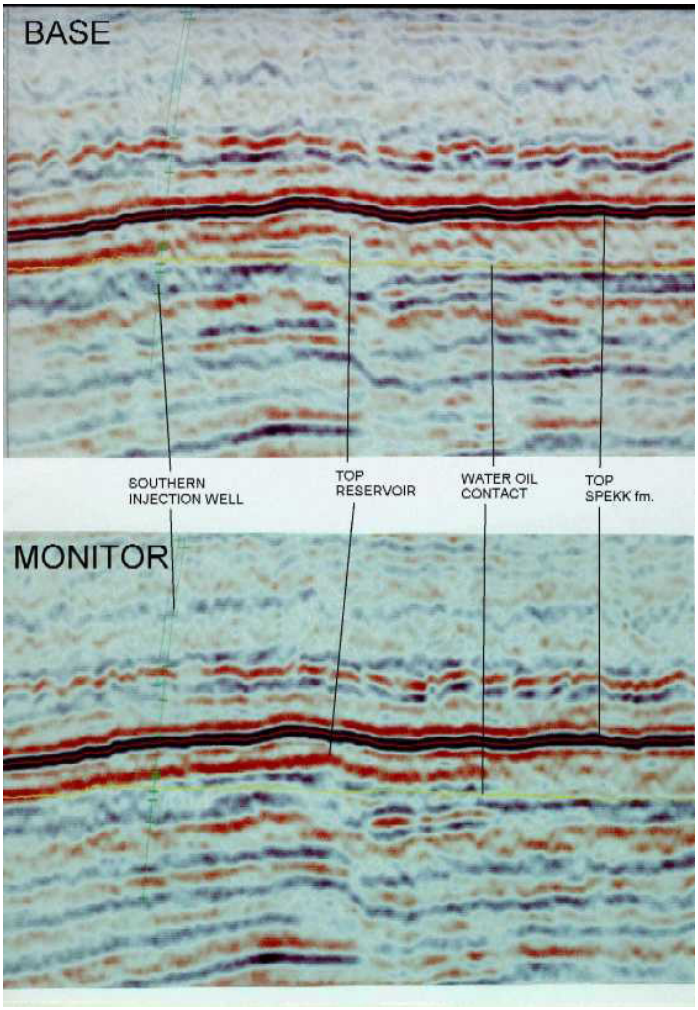

Figure 3.1: Seismic surveys in 1990 (top) and 1998 (bottom) from Draugen field, North Sea

Whether the time-lapse seismic data are used for reservoir monitoring or automatic history matching, comparison between monitor survey and base-line survey is always required, usually by subtracting one from the other. Subtraction should result in an emphasis of changes and absence of events which do not change. To make a meaningful comparison, two important conditions are necessary,

- Signals from locations where no changes in properties have occurred should be

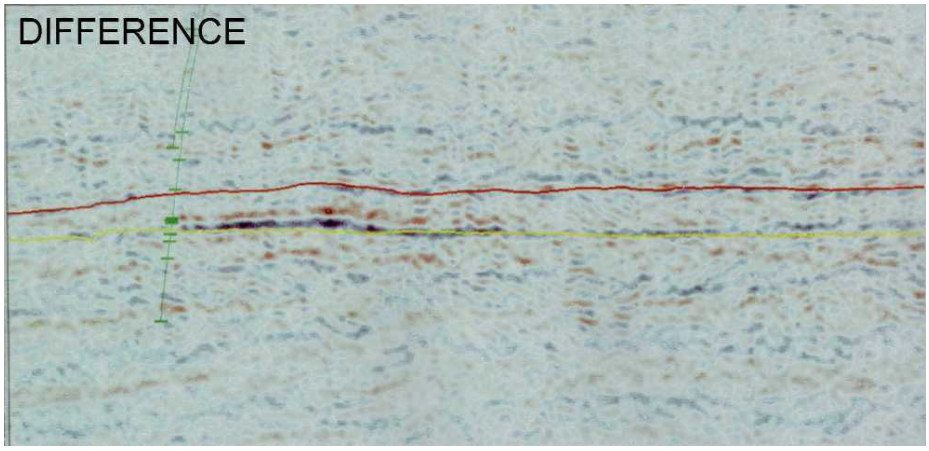

Figure 3.2: Changes from the two surveys from Draugen field, North Sea

kept as similar as possible in different surveys;

- Differences related to saturation, pressure, or stress should be as large as possible in different surveys.

The primary influence on the second condition is from reservoir conditions, such as time interval between surveys, depth of reservoir, and fluid phase changes between surveys. Those reservoir conditions generally can determine whether the changes will be large or not. To address the first condition, some steps must be taken to increase the similarities, in both acquisition and processing. Whenever possible, it is advantageous to use the same survey area, same geometric alignment, and same acquisition parameters, and in processing to use the same parameters for both the base-line survey and the monitor survey. Using the time-lapse seismic terminologies, these are feasibility and repeatability studies in the design phase and cross equalization in the processing phase.

3.2.1 Feasibility study

Feasibility study investigates different reservoir features, such as fluid saturation contrast and dry bulk modulus, to see whether the reservoir is a possible candidate for a successful time-lapse seismic project. The reason is that due to natural limitations,

some reservoirs may not express enough changes in seismic surveys, no matter how long they have been produced. Lumley et al. (1994, 1997) gave an excellent discussion about which kind of reservoirs tend to be good candidates for time-lapse seismic projects. Some ideal reservoirs for time-lapse seismic will have the features listed in Table 3.1, Table 3.2 and Table 3.3.

Parameter	**Options**	**Ideal Cases**
Reservoir	Depth (ft)	shallow
	Overburden pressure (psi)	low
	Pore pressure (psi)	high
	Net pressure (psi)	low
	Temperature (°F)	high
	Unit thickness (ft)	high
Rocks	Dry bulk modulus (GPa)	low
	Dry density (g/cc)	low
	Porosity (%)	high

Table 3.1: Ideal parameters of reservoir and rocks in time-lapse seismic: Part I (Lumley et al., 1997)

Parameter	**Options**	**Ideal Cases**
Oil	Solution GOR (SCF/STB)	high
	Gravity (API)	high
	Density (g/cc)	low
	Bulk modulus (GPa)	low
Water	Salinity (ppm)	high
	Density (g/cc)	high
	Bulk modulus (GPa)	high
Gas	Density (g/cc)	low
	Bulk modulus (GPa)	low
4-D Fluids	Fluid saturation change (%)	high
	Fluid compression contrast (%)	high

Table 3.2: Ideal parameters of reservoir fluids in time-lapse seismic: Part II (Lumley et al., 1997)

Seismic	Ideal Cases
Dominant frequency (Hz)	high
Average resolution (ft)	low
Image quality (1:low, 5:high)	5
Fluid contact visibility (1:low, 5:high)	5
Predicted travel time changes (samples)	> 4
Predicted impedance change (%)	> 4

Table 3.3: Ideal parameters of seismic operations in time-lapse seismic: Part III (Lumley et al., 1997)

3.2.2 Repeatability study

In time-lapse seismic, repeatability does not mean that data from multiple seismic surveys should be as similar as possible everywhere; the most important purpose of time-lapse seismic is to emphasize the changes due to production. Thus, success requires that difference in regions where production has occurred should be maximized. Outside of the productive volume, the differences should be minimized. However, due to non-repeatable noise, such as source generated noise, ambient noise, and naturally induced noise, non-production areas always have different signals in time-lapse seismic surveys. The noise in the data will "blur" the real changes from production zones. The stronger the noise, the larger the signal is needed for meaningful interpretation (Eastwood et al., 1998).

To test how repeatable the time-lapse seismic data will be in a possible survey area, i.e., how strong the non-repeatable noise is, a **zero time repeatability study** (Porter-Hirsche and Hirsche, 1998) is sometimes employed. The idea is that the baseline survey and a monitor survey are both shot on the same day. This can be regarded as zero-lapse seismic survey in terms of production time scale. All survey-related parameters are kept same, such as acquisition geometry, seismic crew, and source type. Under this near ideal condition, any changes observed in the difference of the base-line survey and the monitor survey are most probably from uncontrollable

noise. This noise level can be regarded as a noise threshold. Any non-repeatable noise in data obtained from a real time-lapse seismic project conducted in that area will be higher than the threshold. On the other hand, by conducting reservoir simulation study combined with seismic wave field modelling, it is possible to predict the magnitude of time-lapse seismic changes that will result from production. If the magnitude of predicted seismic changes due to production do not even exceed the threshold noise, the possibility to have a successful time-lapse seismic survey is low.

3.2.3 Cross equalization

For a complete time-lapse seismic project designed from scratch, a feasibility study and a repeatability study provide strong assurance for its success. Many time-lapse seismic surveys conducted in fields were not purposely designed from the beginning to be repeated. The typical situation is that the base-line survey and the monitor survey are taken from two unrelated seismic surveys in the same field. It is not uncommon to see that acquisition systems are different with geometrical coordinates not even aligning and data processing use different parameters. Since it is impractical to re-shoot the surveys, the only feasible way to reduce those artificial distinctions is through re-processing of the data, applying **cross equalization**.

According to Ross et al. (1996) and Rickett and Lumley (2001), cross equalization is a term for match-filtering, amplitude scaling, and static corrections necessary for time-lapse seismic, to remove non-production changes from acquisition and processing done previously. Although different authors have different opinions about what should be done during the cross equalization process (Rickett and Lumley, 2001; Ross et al., 1996), generally, cross equalization should at least include the following three aspects,

- Realignment of geometry of acquisition system;
- Time, bandwidth, and phase equalization;
- Amplitude equalization.

Cross equalization is required when a time-lapse seismic project involves legacy data, but it also helps in a well designed project by adjusting some minor discrepancies between surveys.

3.3 Derivatives of seismic impedance with respect to pressure, saturation, permeability and porosity

In the adjoint equations, seismic impedance change data are integrated separately as two source term groups with opposite signs (Eq. 2.43 and Eq. 2.44). Hence, the two matrices, $\nabla_{y^n}\left[g(m)\right]^T$ and $\nabla_m[g(m)]^T$, involve derivatives of seismic impedance with respect to pressure, phase saturations, and reservoir model parameters (here permeability and porosity are chosen).

Using Eq. 3.4, if the shear wave velocity V_s is used, the explicit derivatives of seismic impedance with respect to pressure, saturations, and porosity are respectively,

$$\frac{\partial Z}{\partial P} = \frac{1}{2}\left(\rho K + \frac{4}{3}\rho^2 V_s^2\right)^{-1/2}\left(K\frac{\partial \rho}{\partial P} + \frac{8}{3}V_s^2\rho\frac{\partial \rho}{\partial P} + \rho\frac{\partial K}{\partial P} + \frac{8}{3}V_s\rho^2\frac{\partial V_s}{\partial P}\right), \tag{3.20}$$

$$\frac{\partial Z}{\partial S_o} = \frac{1}{2}\left(\rho K + \frac{4}{3}\rho^2 V_s^2\right)^{-1/2}\left(K\frac{\partial \rho}{\partial S_o} + \rho\frac{\partial K}{\partial S_o} + \frac{8}{3}V_s^2\rho\frac{\partial \rho}{\partial S_o}\right), \tag{3.21}$$

$$\frac{\partial Z}{\partial S_g} = \frac{1}{2}\left(\rho K + \frac{4}{3}\rho^2 V_s^2\right)^{-1/2}\left(K\frac{\partial \rho}{\partial S_g} + \rho\frac{\partial K}{\partial S_g} + \frac{8}{3}V_s^2\rho\frac{\partial \rho}{\partial S_g}\right), \tag{3.22}$$

and

$$\frac{\partial Z}{\partial \phi} = \frac{1}{2}\left(\rho K + \frac{4}{3}\rho^2 V_s^2\right)^{-1/2}\left(\left(K + \frac{8}{3}\rho V_s^2\right)\frac{\partial \rho}{\partial \phi} + \rho\frac{\partial K}{\partial \phi} + \frac{8}{3}\rho^2 V_s\frac{\partial V_s}{\partial \phi}\right). \tag{3.23}$$

Because there is no direct dependence between impedance and permeability, the derivative of impedance with respect to permeability is zero.

If the shear modulus G is used, the derivatives will be changed into,

$$\frac{\partial Z}{\partial P} = \frac{1}{2}\left(\rho K + \frac{4}{3}\rho G\right)^{-1/2}\left(K\frac{\partial \rho}{\partial P} + \rho\frac{\partial K}{\partial P} + \frac{4}{3}G\frac{\partial \rho}{\partial P} + \frac{4}{3}\rho\frac{\partial G}{\partial P}\right), \tag{3.24}$$

$$\frac{\partial Z}{\partial S_o} = \frac{1}{2}\left(\rho K + \frac{4}{3}\rho G\right)^{-1/2}\left(\left(K + \frac{4}{3}G\right)\frac{\partial \rho}{\partial S_o} + \rho\frac{\partial K}{\partial S_o}\right), \tag{3.25}$$

$$\frac{\partial Z}{\partial S_g} = \frac{1}{2}\left(\rho K + \frac{4}{3}\rho G\right)^{-1/2}\left(\left(K + \frac{4}{3}G\right)\frac{\partial \rho}{\partial S_g} + \rho\frac{\partial K}{\partial S_g}\right), \tag{3.26}$$

and

$$\frac{\partial Z}{\partial \phi} = \frac{1}{2}\left(\rho K + \frac{4}{3}\rho G\right)^{-1/2}\left(\rho\frac{\partial K}{\partial \phi} + K\frac{\partial \rho}{\partial \phi} + \frac{4}{3}\rho\frac{\partial G}{\partial \phi} + \frac{4}{3}G\frac{\partial \rho}{\partial \phi}\right). \tag{3.27}$$

It can be seen that whichever is used, V_s or G, the derivatives of the bulk modulus K with respect to P, S_o, S_g, and ϕ must be calculated. They can be obtained by applying the chain rule to the Gassmann equations. Similarly, the derivatives of G or V_s can be computed starting from the Han, Kuster and Toksöz equation, and Ramammorthy equations and then applying the chain rule.

3.3.1 Derivatives of the Gassmann equations

If Eq. 3.7 is plugged into Eq. 3.6, the Gassmann equations can be written as,

$$K = K_{\text{grain}}\frac{A}{B}, \tag{3.28}$$

where,

$$A = \phi K_{\text{frame}}K_{\text{grain}} - \phi K_{\text{frame}}K_{\text{fluid}} + K_{\text{fluid}}K_{\text{grain}} - K_{\text{fluid}}K_{\text{frame}}, \tag{3.29}$$

and

$$B = \phi K_{\text{grain}}^2 - \phi K_{\text{grain}}K_{\text{fluid}} + K_{\text{fluid}}K_{\text{grain}} - K_{\text{fluid}}K_{\text{frame}}. \tag{3.30}$$

Therefore, the derivative of the bulk modulus K with respect to pressure P is,

$$\frac{\partial K}{\partial P} = K_{\text{grain}}\frac{B\frac{\partial A}{\partial P} - A\frac{\partial B}{\partial P}}{B^2}, \tag{3.31}$$

where

$$\begin{aligned}\frac{\partial A}{\partial P} =& \frac{\partial K_{\text{frame}}}{\partial P}\left(\phi K_{\text{grain}} - \phi K_{\text{fluid}} - K_{\text{fluid}}\right) \\ &+ \frac{\partial \phi}{\partial P}\left(K_{\text{grain}}K_{\text{frame}} - K_{\text{fluid}}K_{\text{frame}}\right) \\ &+ \frac{\partial K_{\text{fluid}}}{\partial P}\left(K_{\text{grain}} - \phi K_{\text{frame}} - K_{\text{frame}}\right),\end{aligned} \tag{3.32}$$

and

$$\begin{aligned}\frac{\partial B}{\partial P} =& \frac{\partial \phi}{\partial P}\left(K_{\text{grain}}^2 - K_{\text{grain}}K_{\text{fluid}}\right) - K_{\text{fluid}}\frac{\partial K_{\text{frame}}}{\partial P} \\ &+ \frac{\partial K_{\text{fluid}}}{\partial P}\left(K_{\text{grain}} - \phi K_{\text{grain}} - K_{\text{frame}}\right) .\end{aligned} \tag{3.33}$$

There is no derivative of K_{grain} with respect to pressure because Eq. 3.13 is used. If Eq. 3.14 is used, the derivative of K_{frame} with respect to P is

$$\frac{\partial K_{\text{frame}}}{\partial P} = -4.25\ln(10)10^{\left(\log_{10}(K_{\text{grain}})-4.25\phi\right)}\frac{\partial \phi}{\partial P} . \tag{3.34}$$

Using Eq. 3.8, the derivative of K_{fluid} with respect to pressure is,

$$\frac{\partial K_{\text{fluid}}}{\partial P} = \left(\frac{S_w}{K_w} + \frac{S_o}{K_o} + \frac{S_g}{K_g}\right)^{-2}\left(\frac{S_w}{K_w^2}\frac{\partial K_w}{\partial P} + \frac{S_o}{K_o^2}\frac{\partial K_o}{\partial P} + \frac{S_g}{K_g^2}\frac{\partial K_g}{\partial P}\right) , \tag{3.35}$$

where derivatives of bulk modulli of three phases with respect to pressure are required. The isothermal compressibilities of oil, gas, and water are defined as

$$c_g = -\frac{1}{B_g}\frac{dB_g}{dP} , \tag{3.36}$$

$$c_w = -\frac{1}{B_w}\frac{dB_w}{dP} , \tag{3.37}$$

and

$$c_o = -\frac{1}{B_o}\frac{dB_o}{dP} + \frac{B_g}{B_o}\frac{dR_s}{dP} , \tag{3.38}$$

so the derivatives can be written as

$$\frac{\partial K_g}{\partial P} = -K_g^2\left(\frac{1}{B_g^2}\left(\frac{dB_g}{dP}\right)^2 - \frac{1}{B_g}\frac{d^2B_g}{dP^2}\right) , \tag{3.39}$$

$$\frac{\partial K_w}{\partial P} = -K_w^2\left(\frac{1}{B_w^2}\left(\frac{dB_w}{dP}\right)^2 - \frac{1}{B_w}\frac{d^2B_w}{dP^2}\right) , \tag{3.40}$$

and

$$\frac{\partial K_o}{\partial P} = -K_o^2\left(\frac{1}{B_o}\frac{dB_g}{dP}\frac{dR_s}{dP} + \frac{B_g}{B_o}\frac{d^2R_s}{dP^2} - \frac{B_g}{B_o^2}\frac{dR_s}{dP}\frac{dB_o}{dP} + \frac{1}{B_o^2}\left(\frac{dB_o}{dP}\right)^2 - \frac{1}{B_o}\frac{d^2B_o}{dP^2}\right) , \tag{3.41}$$

where $K_o = 1/c_o$, $K_g = 1/c_g$ and $K_w = 1/c_w$. Applying Eq. 3.34, Eq. 3.35, Eq. 3.39, Eq. 3.40, and Eq. 3.41, the derivative in Eq. 3.31 can be calculated.

Taking derivative in Eq. 3.28 with respect to oil saturation S_o gives the following equations,

$$\frac{\partial K}{\partial S_o} = K_{\text{grain}} \frac{B\frac{\partial A}{\partial S_o} - A\frac{\partial B}{\partial S_o}}{B^2}\,, \tag{3.42}$$

where, $\frac{\partial A}{\partial S_o}$ and $\frac{\partial B}{\partial S_o}$ are

$$\frac{\partial A}{\partial S_o} = \frac{\partial K_{\text{fluid}}}{\partial S_o}\left(K_{\text{grain}} - K_{\text{frame}} - \phi K_{\text{frame}}\right)\,, \tag{3.43}$$

and

$$\frac{\partial B}{\partial S_o} = \frac{\partial K_{\text{fluid}}}{\partial S_o}\left(K_{\text{grain}} - \phi K_{\text{grain}} K_{\text{frame}}\right)\,. \tag{3.44}$$

From Eq. 3.8, the derivative of bulk modulus of fluid with respect to S_o is

$$\frac{\partial K_{\text{fluid}}}{\partial S_o} = \left(\frac{S_o}{K_o} + \frac{S_g}{K_g} + \frac{1 - S_o - S_g}{K_w}\right)^{-2}\left(\frac{1}{K_w} - \frac{1}{K_o}\right)\,. \tag{3.45}$$

The derivative of bulk modulus with respect to gas saturation S_g has the same form as the derivative with respect to oil saturation (Eq. 3.42). The only difference is the derivative of bulk modulus of fluid, which becomes

$$\frac{\partial K_{\text{fluid}}}{\partial S_g} = \left(\frac{S_o}{K_o} + \frac{S_g}{K_g} + \frac{1 - S_o - S_g}{K_w}\right)^{-2}\left(\frac{1}{K_w} - \frac{1}{K_g}\right)\,. \tag{3.46}$$

The derivative of the bulk modulus K with respect to ϕ is

$$\frac{\partial K}{\partial \phi} = K_{\text{grain}} \frac{B\frac{\partial A}{\partial \phi} - A\frac{\partial B}{\partial \phi}}{B^2}\,, \tag{3.47}$$

where

$$\frac{\partial A}{\partial \phi} = \left(K_{\text{grain}} - K_{\text{fluid}}\right)\left(K_{\text{frame}} + \phi\frac{\partial K_{\text{frame}}}{\partial \phi}\right) - K_{\text{fluid}}\frac{\partial K_{\text{frame}}}{\partial \phi}\,, \tag{3.48}$$

and

$$\frac{\partial B}{\partial \phi} = K_{\text{grain}}^2 - K_{\text{grain}} K_{\text{fluid}} - K_{\text{fluid}}\frac{\partial K_{\text{frame}}}{\partial \phi}\,. \tag{3.49}$$

There is no dependence of K_{grain} on porosity. The derivative of K_{frame} with respect to ϕ is

$$\frac{\partial K_{\text{frame}}}{\partial \phi} = -4.25\ln(10)10^{\left(\log_{10}(K_{\text{grain}}) - 4.25\phi\right)}\,. \tag{3.50}$$

3.3.2 Derivatives of the equations for G and V_s

Whichever equation group is chosen, the Han equation, the Kuster and Toksöz equation, or the Ramammorthy equations, only derivatives of G or V_s with respect to pressure and porosity need to be computed because there is no direct dependence of G or V_s on S_o and S_g.

If the Han equation (Eq. 3.15) is used to compute the shear wave velocity V_s, the derivatives are

$$\frac{\partial V_s}{\partial P} = -4910.0 \times \frac{\partial \phi}{\partial P}\,, \tag{3.51}$$

and

$$\frac{\partial V_s}{\partial \phi} = -4910.0\,. \tag{3.52}$$

If the Kuster and Toksöz equation (Eq. 3.16) is used, G does not depend on pressure and porosity.

If the Ramammorthy equations (Eq. 3.17 and Eq. 3.18) are used, the derivatives are

$$\frac{\partial G}{\partial P} = G_{\text{grain}}\left(4.38\phi - 3.48\right)\frac{\partial \phi}{\partial P}\,, \tag{3.53}$$

and

$$\frac{\partial G}{\partial \phi} = G_{\text{grain}}\left(4.38\phi - 3.48\right)\,. \tag{3.54}$$

3.3.3 Some other derivatives required for computation

From Eq. 3.20 to Eq. 3.27, it can be seen that in addition to the derivatives of the modulus or the shear wave velocity with respect to pressure, saturation, and porosity, the derivatives of the body density ρ are also required. If Eq. 3.5 is used, these derivatives are

$$\begin{aligned}\frac{\partial \rho}{\partial P} = \phi\left(S_o\frac{\partial \rho_o}{\partial P} + \left(1.0 - S_o - S_g\right)\frac{\partial \rho_w}{\partial P} + S_g\frac{\partial \rho_g}{\partial P}\right)\\ + \left(\rho_o S_o + \rho_w\left(1.0 - S_o - S_g\right) + \rho_g S_g - \rho_{\text{solid}}\right)\frac{\partial \phi}{\partial P}\,,\end{aligned} \tag{3.55}$$

$$\frac{\partial \rho}{\partial S_o} = \phi \left(\rho_o - \rho_w \right) , \tag{3.56}$$

$$\frac{\partial \rho}{\partial S_g} = \phi \left(\rho_g - \rho_w \right) , \tag{3.57}$$

and

$$\frac{\partial \rho}{\partial \phi} = \rho_w \left(1 - S_o - S_g \right) + \rho_o S_o + \rho_g S_g - \rho_{\text{solid}} . \tag{3.58}$$

3.4 Sensitivity computation

The estimation of flow parameters may be complicated by uncertainty (and variability) in other properties that affect the impedance, such as shaliness and lithology. It is important to compare the sensitivity of impedance change from all possible effects. In this section, a sensitivity study is conducted using two synthetic models.

3.4.1 Predominant effect of phase saturation change in seismic impedance change

The purpose of using seismic impedance change data in history matching is to infer information about phase saturation change due to production. In practice, it is not clear that this can be done because other poorly known properties of the reservoir such as sand modulus, clay modulus, and shaliness may also affect the seismic impedance. Even if these parameters do not change with time, the model will include errors because spatially uniform values are usually assumed for these spatially varying parameters. Before using seismic impedance change data in automatic history matching, we must make sure that the change of phase saturation will be the predominant effect. In this investigation, some typical values are chosen for a sensitivity study to show that the effect from phase saturation change will be the dominant effect on seismic impedance change. Two cases are considered, one of which is an oil reservoir under water flood and the other is a solution gas drive reservoir. In both cases, the changes in impedance due to changes in saturation are computed for several values of rock parameters. The purpose is to determine if uncertainty in those parameters

will cause significant deviation in seismic impedance change for the same saturation changes. The base values of the reservoir parameters are shown in Table 3.4. In

Parameter	Value
Porosity	0.2
Shaliness	0.2
Sand modulus (Pa)	3.8×10^{10}
Clay modulus (Pa)	21.2×10^{9}
Density of solid (kg/m^3)	$2,650$
Density of gas (kg/m^3)	214
Density of water (kg/m^3)	986
Density of oil (kg/m^3)	707
Modulus of gas (Pa)	3.94×10^{7}
Modulus of water (Pa)	2.39×10^{9}
Modulus of oil (Pa)	6.71×10^{8}
Initial water saturation	0.2
Initial oil saturation	0.8
Initial gas saturation	0.0

Table 3.4: Base values in computation of sensitivity of phase saturation to seismic impedance change (water flood)

water flood case, upper and lower bounds for the sensitivity study are shown in Table 3.5. By varying each parameter, it is possible to study the "effect of uncertainty" in these parameters on the change in seismic impedance. By assuming different val-

Parameter	Lower Bound	Upper Bound
Water saturation	0.2	0.6
Shaliness	0.0	0.4
Clay modulus	1.0×10^{10}	3.0×10^{10}
Sand modulus	2.8×10^{10}	4.8×10^{10}

Table 3.5: Lower and upper bounds for reservoir parameters (water flood)

ues of other parameters, changing one parameter at a time, the impedance changes are recomputed. From Table 3.6, it can be seen that even if the value of the rock mineral parameters were greatly in error, the error in seismic impedance change due to water saturation change would be small. That is to say that the uncertainty of

Parameter	Seismic Impedance Change	Change Ratio
Base value	251978	3.6%
Shaliness in lower bound	242795	3.5%
Shaliness in upper bound	265121	3.8%
Clay modulus in lower bound	249037	3.6%
Clay modulus in upper bound	252823	3.6%
Sand modulus in lower bound	247481	3.5%
Sand modulus in upper bound	253692	3.6%

Table 3.6: Change in seismic impedance from changing water saturation in various reservoir rocks

shaliness, grain modulus, and shale modulus in the seismic impedance change data can be neglected.

In the solution gas drive case, the base values are the same as the water flood (Table 3.4). The bounds on parameter values for the sensitivity study are shown in Table 3.7. Using the same methods described previously, the results are shown in

Parameter	Lower Bound	Upper Bound
Gas saturation	0.0	0.5
Shaliness	0.0	0.4
Clay modulus	1.0×10^{10}	3.0×10^{10}
Sand modulus	2.8×10^{10}	4.8×10^{10}

Table 3.7: Lower and upper bounds for reservoir parameters (solution gas drive)

Table 3.8. It is clear that in solution gas drive, the phase saturation change is still the most important effect. Given these results, it appears that the uncertainty in mineralogy can be dealt with as part of modelling error and that its effect on change in impedance is small compared to those parameters that affect the phase saturation, such as permeability and porosity.

3.4.2 Synthetic results

In order to test the computation of the sensitivity of impedance change to permeability and porosity, two synthetic models were created. Both of them use a $15 \times 15 \times 1$ grid

Parameter	Seismic Impedance Change	Change Ratio
Base value	−526631	−7.5%
Shaliness in lower bound	−502306	−7.2%
Shaliness in upper bound	−562770	−8.0%
Clay modulus in lower bound	−528152	−7.5%
Clay modulus in upper bound	−525463	−7.5%
Sand modulus in lower bound	−528241	−7.5%
Sand modulus in upper bound	−523081	−7.5%

Table 3.8: Change in seismic impedance from changing gas saturation in various reservoir rocks

with $\triangle x = \triangle y = 40$ ft and $\triangle z = 30$ ft. The porosity field is homogenous and equal to 0.22. The permeability field is heterogenous and isotropic. The mean of the log horizontal permeability, $\ln(k)$, is 3.95 (52 md) and the variance is 0.52.

In one model, there are five wells. An injector is in gridblock $(8, 8)$ and four producers are located symmetrically in gridblocks $(3, 3)$, $(3, 13)$, $(13, 3)$, and $(13, 13)$ (see white circles in Fig. 3.3(a)). This model is used to simulate a water flood case where the initial pressure in the oil reservoir is $4,500$ psi, which is slightly above the initial bubble point pressure, $4,417$ psi. Each producer produces at total fluid rate 220 RB/D. The minimum bottom hole pressure for each producer is 50 psi and the maximum permitted WOR for each producer is 0.49. For the injector, the maximum water injection rate is 550 RB/D. Initial oil saturation is 0.8 and the initial water saturation is equal to irreducible water saturation $S_{wc} = 0.2$.

The other model has one producer in gridblock $(3, 3)$ (see white circle in Fig. 3.3(b)). It is used to simulate production by solution gas drive. This producer produces at total fluid rate 700 RB/D. The minimum bottom hole pressure is 50 psi and the maximum permitted WOR is 0.49. All initial reservoir pressure, initial bubble point pressure, oil saturation, and water saturation are the same as those in the water flood case.

In both cases, the sensitivities are computed of seismic impedance change in grid-blocks $x = 5, y = 4$ and $x = 10, y = 6$ (see black rectangles in Fig. 3.3) to log horizontal permeability and porosity at the 30th day. Also the corresponding water and gas saturation distribution maps and pressure maps are output for reference.

From these maps, some observations can be drawn as following,

1. In the water flood case, the seismic impedance change map (Fig. 3.5) has the same features as the water saturation change map (Fig. 3.4(a)). In the solution gas drive case, there is also great similarity between the seismic impedance change map and the gas saturation change map (Fig. 3.6 and Fig. 3.4(b)). In this case the change in seismic impedance is mainly due to the change in fluid saturation due to production. Using the seismic impedance change, it would be feasible to qualitatively monitor the reservoir production.

2. From the sensitivity of seismic impedance change to log permeability in the water flood case (Fig. 3.7(a) and Fig. 3.8(a)) and the solution gas drive case (Fig. 3.7(b) and Fig. 3.8(b)), it can be seen that seismic impedance change has sensitivity dependence on reservoir permeability because the change in reservoir permeability will affect the change in phase saturation. So seismic impedance change is clearly "sensitive" to the change in permeability.

3. In addition to the direct effect of porosity on impedance change, the seismic impedance change also has an indirect dependence on porosity, which can be understood from the phase saturation equation:

$$\frac{\partial S}{\partial t} + \left(\frac{U_T}{\phi} \frac{df}{dS} \right) \frac{\partial S}{\partial x} = 0 \,, \tag{3.59}$$

where the term in parenthesis is called the "phase velocity", which describes the rate of advance of the phase saturations. Because this velocity includes porosity ϕ, we see that the seismic impedance change must also be sensitive to porosity through the effect on saturation.

4. The shapes of the maps of sensitivity to porosity in the water flood case (Fig. 3.7(c) and Fig. 3.8(c)) and the solution gas drive case (Fig. 3.7(d) and Fig. 3.8(d)) do not look at all like the shapes of the maps of sensitivity to log permeability. The reason is that the sensitivity can be divided into two terms as follows:

$$\frac{\partial J}{\partial \phi} = \frac{\partial Z}{\partial \phi} + \frac{\partial f}{\partial \phi}\lambda \tag{3.60}$$

where $\partial Z/\partial\phi$ is the direct derivative term and $\lambda\partial f/\partial\phi$ is the contribution to the derivative from the flow equations. In porosity sensitivity, the direct term is very large compared to the effect from the flow equations. This is different from permeability sensitivity because seismic impedance change has no direct dependence on permeability. Thus, the seismic impedance change data are more sensitive to porosity than to permeability.

5. A comparison of the sensitivity of seismic impedance change to log permeability and porosity from the perturbation method and the adjoint method shows that the different methods give almost identical results for the water flood case (Fig. 3.9) and the solution gas drive case (Fig. 3.10). The relative errors between the two methods are generally on the order of 10^{-4} (Fig. 3.11, Fig. 3.12, Fig. 3.13 and Fig. 3.14).[1]

6. In Fig. 3.7(a), it can be seen that the most obvious sensitivities are distributed along the path from the center-located injection well to the production well at the lower-left corner because gridblock $(4, 5)$ is in that path. Between gridblock $(4, 5)$ and the injection well, high permeability values tend to make water flow fast, resulting in large seismic impedance increase, so the sensitivity coefficients are positive. Around the production well, however, high permeability values will make small pressure difference, which can reduce the seismic impedance

[1]The relative error is defined as $\epsilon = \frac{|\sigma_p - \sigma_a|}{\sigma_p}$, where σ_p is the sensitivity computed using the perturbation method and σ_a is the sensitivity from the adjoint method.

change, so the sensitivity coefficients are negative. For the solution gas drive (Fig. 3.8(b)), the major sensitivities are around the production well at the lower-left corner, where low permeability values give high pressure drop, resulting in large impedance change arising from gas saturation increase, so the sensitivity coefficients are negative. Since the sensitivity of seismic impedance change with respect to porosity is dominated by the direct dependence term (Eq. 3.60), gridblocks $(4, 5)$ and $(6, 10)$ are emphasized respectively in Figs. 3.7(c), 3.7(d), 3.8(c), and 3.8(d).

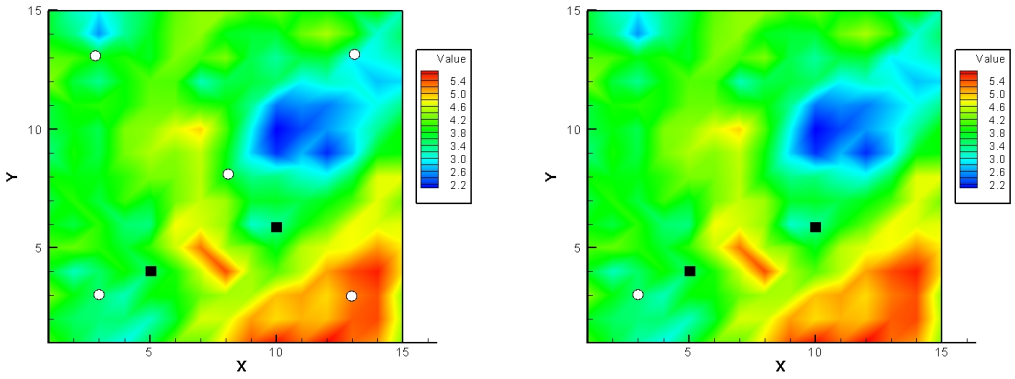

(a) Water flood (b) Solution gas drive

Figure 3.3: Reference $\ln(k)$ field and well locations

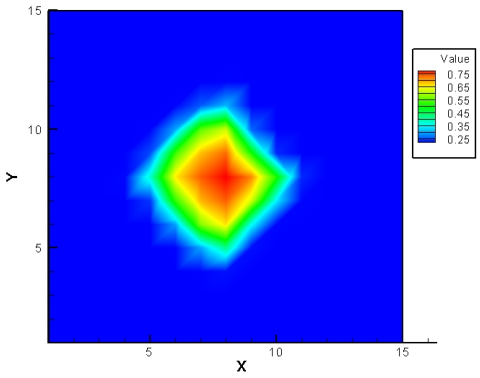

(a) Water saturation for water flood

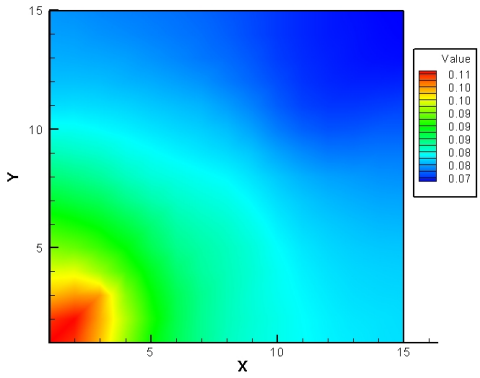

(b) Gas saturation for solution gas drive

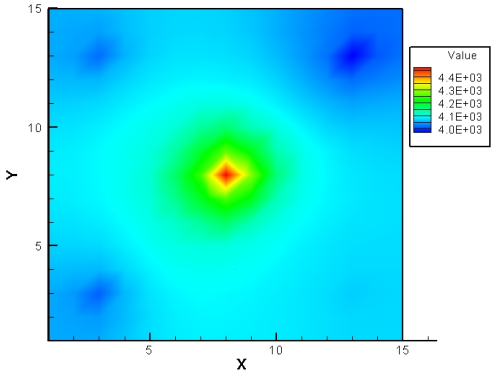

(c) Pressure for water flood

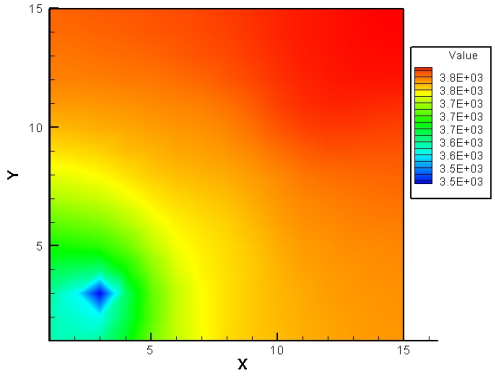

(d) Pressure for solution gas drive

Figure 3.4: Water, gas saturation and pressure distributions at the 30th day

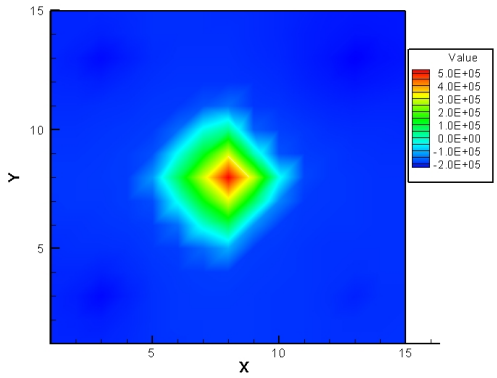

Figure 3.5: Seismic impedance change at the 30th day (water flood)

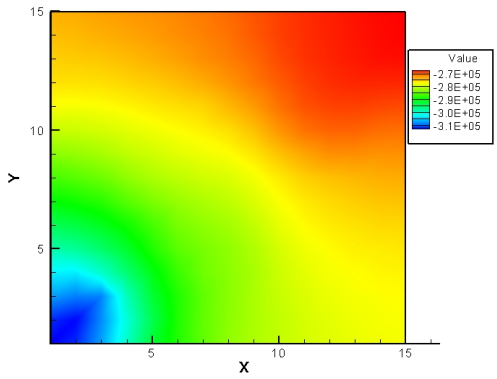

Figure 3.6: Seismic impedance change at the 30th day (solution gas drive)

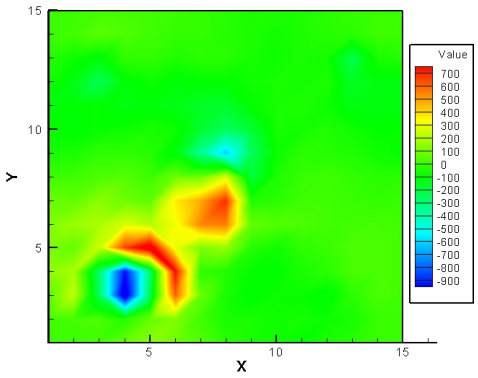

(a) Sensitivity to $\ln(k)$ for water flood

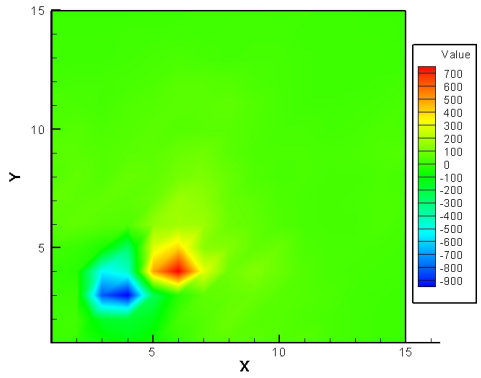

(b) Sensitivity to $\ln(k)$ for solution gas drive

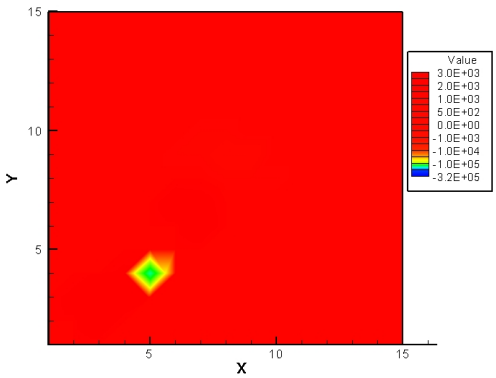

(c) Sensitivity to ϕ for water flood

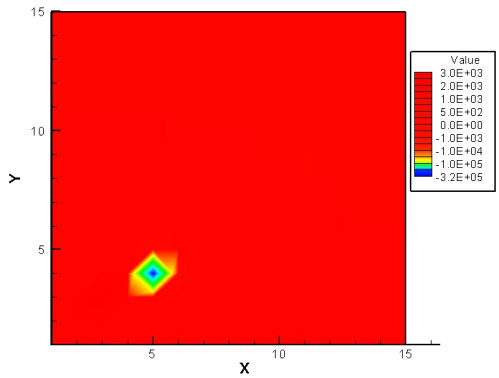

(d) Sensitivity to ϕ for solution gas drive

Figure 3.7: Sensitivity of seismic impedance change in gridblock $(4, 5)$ to $\ln(k)$ and ϕ at the 30th day

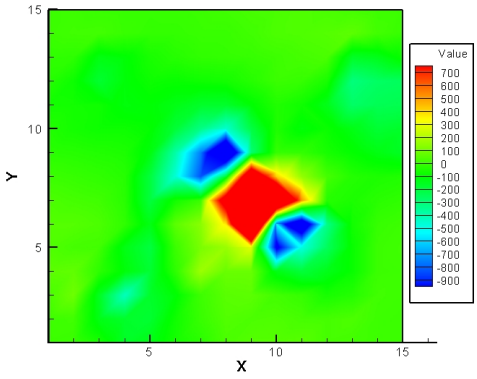

(a) Sensitivity to $\ln(k)$ for water flood

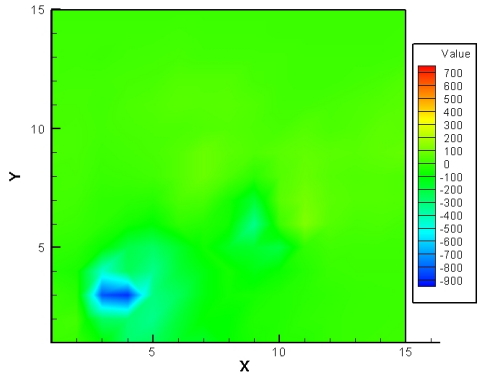

(b) Sensitivity to $\ln(k)$ for solution gas drive

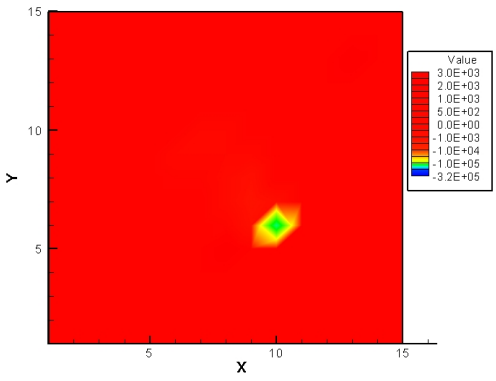

(c) Sensitivity to ϕ for water flood

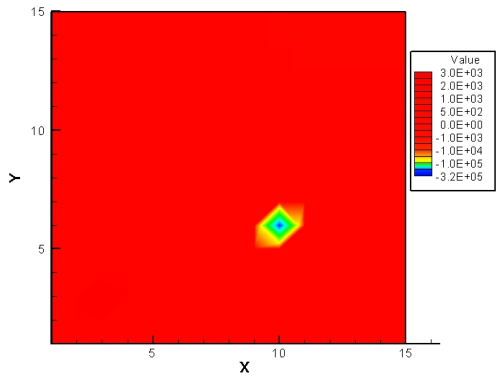

(d) Sensitivity to ϕ for solution gas drive

Figure 3.8: Sensitivity of seismic impedance change in gridblock $(6, 10)$ to $\ln(k)$ and ϕ at the 30th day

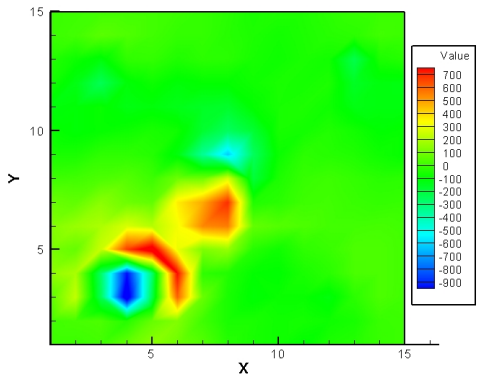

(a) Sensitivity to $\ln(k)$ by adjoint method

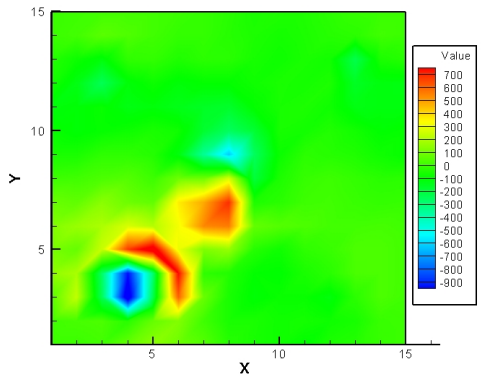

(b) Sensitivity to $\ln(k)$ by perturbation method

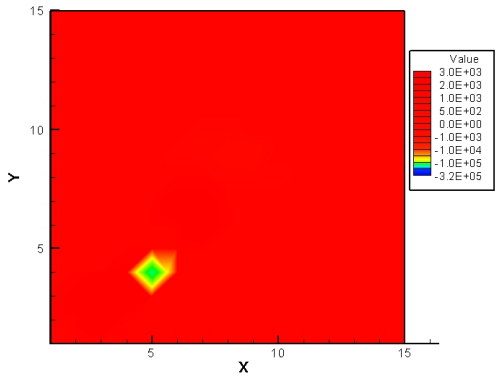

(c) Sensitivity to ϕ by adjoint method

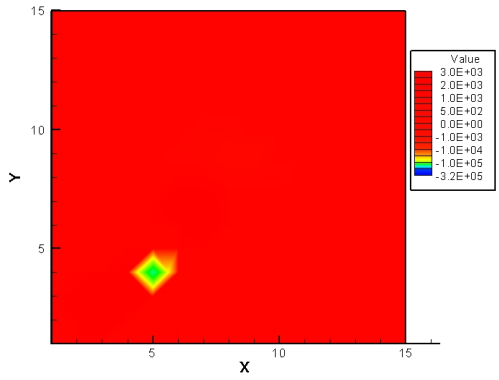

(d) Sensitivity to ϕ by perturbation method

Figure 3.9: Comparison between the adjoint method and the perturbation method in computing sensitivity of seismic impedance change in gridblock $(4, 5)$ to $\ln(k)$ and ϕ at the 30th day (water flood)

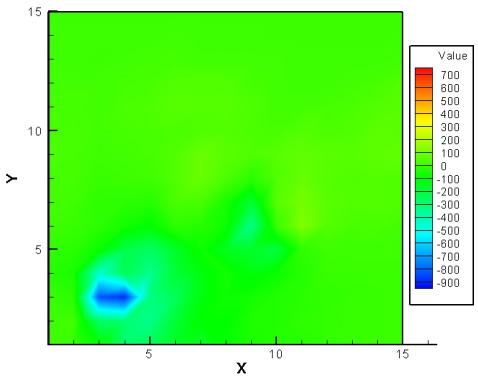

(a) Sensitivity to $\ln(k)$ by adjoint method

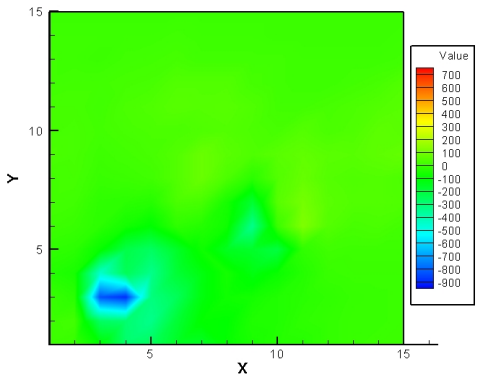

(b) Sensitivity to $\ln(k)$ by perturbation method

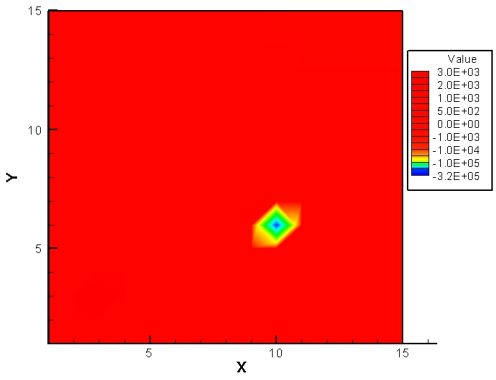

(c) Sensitivity to ϕ by adjoint method

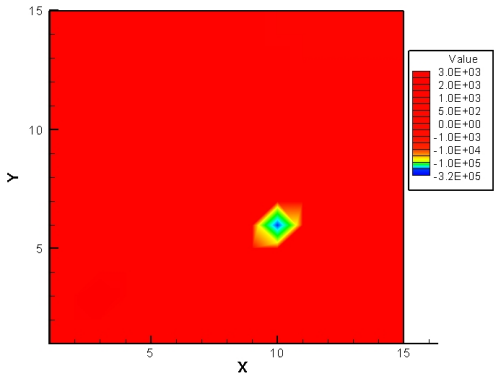

(d) Sensitivity to ϕ by perturbation method

Figure 3.10: Comparison between the adjoint method and the perturbation method in computing sensitivity of seismic impedance change in gridblock $(6, 10)$ to $\ln(k)$ and ϕ at the 30th day (solution gas drive)

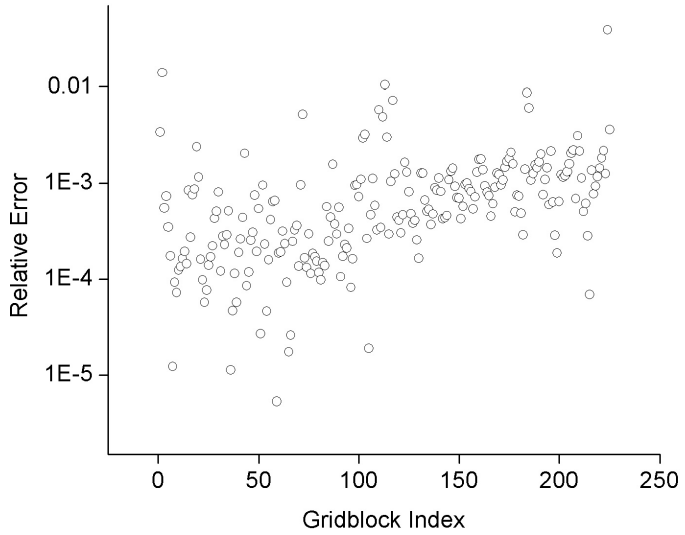

Figure 3.11: Relative error between the adjoint method and the perturbation method in computing sensitivity of seismic impedance change in gridblock $(4, 5)$ to $\ln(k)$ at the 30th day (water flood)

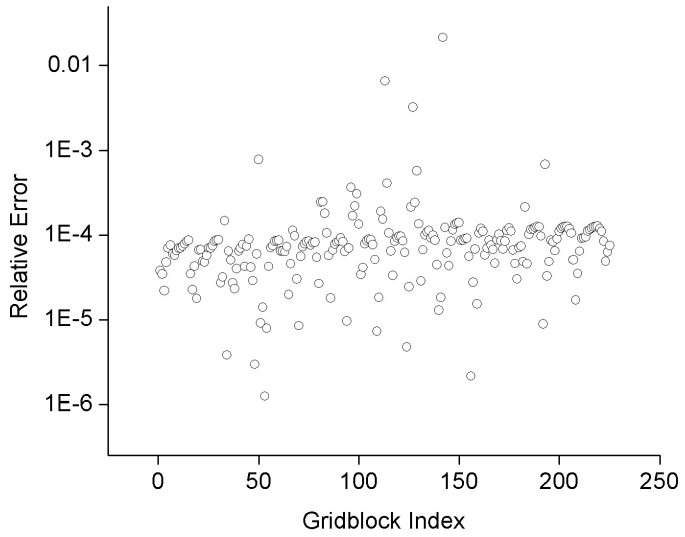

Figure 3.12: Relative error between the adjoint method and the perturbation method in computing sensitivity of seismic impedance change in gridblock $(4, 5)$ to ϕ at the 30th day (water flood)

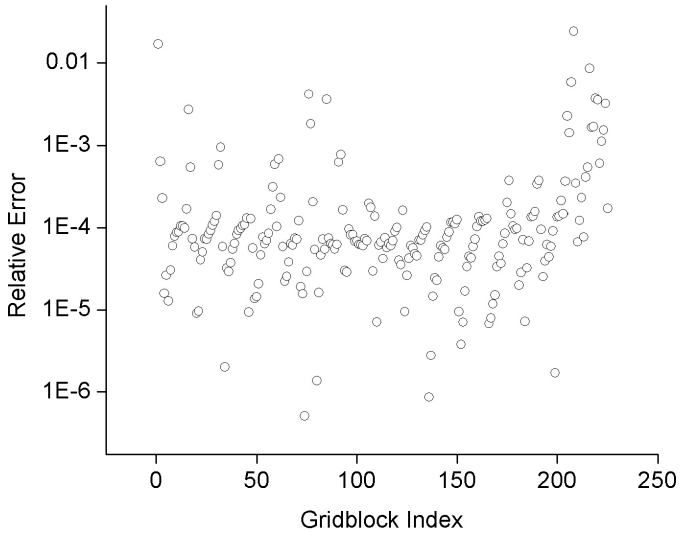

Figure 3.13: Relative error between the adjoint method and the perturbation method in computing sensitivity of seismic impedance change in gridblock $(6, 10)$ to $\ln(k)$ at the 30th day (solution gas drive)

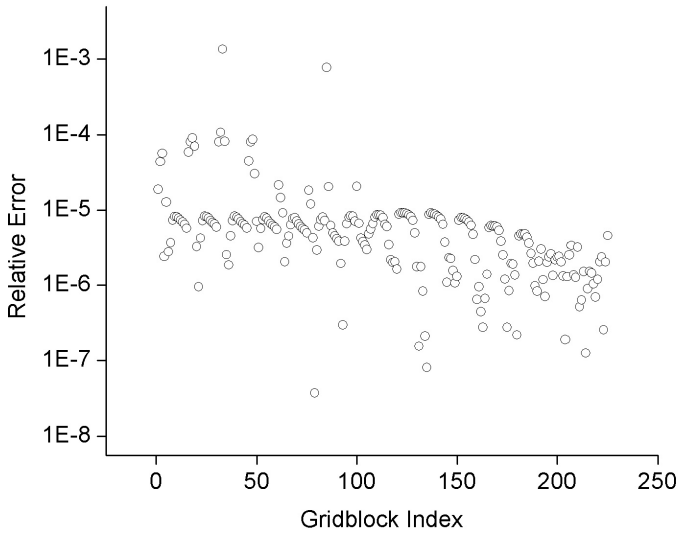

Figure 3.14: Relative error between the adjoint method and the perturbation method in computing sensitivity of seismic impedance change in gridblock $(6, 10)$ to ϕ at the 30th day (solution gas drive)

CHAPTER IV

SYNTHETIC AND SEMI-SYNTHETIC CASE STUDIES

As seen from Chapter 3, the seismic impedance change data are dependent on permeability and porosity, which provides the physical basis for integration of seismic impedance change data into automatic history matching. In this chapter, a complete estimation procedure using both seismic impedance change data and production data will be demonstrated through two case studies. One is a small synthetic model and the other one is a medium-sized semi-synthetic model generated from the Tengiz field, Kazakhstan.

The minimization process derived from automatic history matching involves two computationally demanding tasks. One is the gradient computation, which has been described in Chapter 2 and Chapter 3. The other is the search direction calculation, for which the LBFGS method is used.

4.1 LBFGS method

To minimize the objective function for history matching, Eq. 2.7, requires iterative updating due to its high non-linearity. In general form, this iteration procedure can be written as

$$m_{k+1} = m_k + \delta m_{k+1}\,, \tag{4.1}$$

where k is the iteration index, m_k is the model parameter vector at iteration step k and δm_{k+1} is the model updating vector, which is called the search direction. Computation of the search direction is the crucial problem for any minimization algorithm.

Since the gradient of the objective function is available, one natural choice is to use the negative direction of the gradient as the search direction, as in the Steepest Descent method. The equation is (Nocedal and Wright, 1999)

$$m_{k+1} = m_k - \alpha_k \nabla O(m_k)\,, \tag{4.2}$$

where α_k is the step size, i.e., how far to go along the search direction, and $\nabla O(m_k)$ is the gradient, which is

$$\nabla O(m_k) = C_M^{-1}\left(m_k - m_{\text{prior}}\right) + G_k^T C_D^{-1}\left(g(m_k) - d_{\text{obs}}\right)\,. \tag{4.3}$$

The matrix G_k in Eq. 4.3 is the sensitivity coefficient matrix, whose entry is

$$g_{i,j} = \frac{\partial g_i}{\partial m_j}\,. \tag{4.4}$$

Note that Eq. 4.3 is only used in derivation. The gradient is actually computed directly using the adjoint method so the sensitivity coefficient matrix in Eq. 4.4 is never formed. The Steepest Descent method is easy to implement, but its convergence rate is only linear. Therefore, a large number of iteration steps are required for convergence, although the initial reduction can be substantial. For the realistic problems in history matching, the Steepest Descent method is impractical.

If not only the gradient but also the Hessian matrix (the second derivative) are computed, the widely used Gauss-Newton method can be used. It computes the search direction using Eq. 4.5,

$$H(m_k)\delta m_{k+1} = -\nabla O(m_k)\,, \tag{4.5}$$

where $H(m_k)$ is the approximate Hessian matrix,[1]

$$H(m_k) = C_M^{-1} + G_k^T C_D^{-1} G_k\,, \tag{4.6}$$

[1]The true Hessian matrix has a term involving the derivative of the sensitivity coefficient matrix G_k, but the approximate Hessian matrix drops off that term. In this dissertation, "the Hessian matrix" is used exclusively to denote the matrix shown in Eq. 4.6.

where G_k is the same sensitivity coefficient matrix as the one in Eq. 4.4. If a damping factor is added to the left hand side of Eq. 4.5, to prevent the estimated model from over-matching the data mismatch term at the first few iteration steps, the Gauss-Newton method can be converted into the Levenberg-Marquardt algorithm. The choice of an appropriate damping factor is crucial to the success of Levenberg-Marquardt algorithm. Some successful schemes can be found in Abacioglu et al. (2001) and Li (2001).

Since the bottleneck with the Gauss-Newton method is the computation of the Hessian matrix, one possible alternate way is to consider methods that only use the gradient of the objective function. A number of methods belong to that category, such as the Conjugate Gradient method, the Preconditioned Conjugate Gradient method, and the quasi-Newton family. According to the investigations of Zhang and Reynolds (2002) and Zhang (2002), the limited memory Broyden-Fletcher-Goldfarb-Shanno (LBFGS) method (Nocedal, 1980) is the most successful method for our automatic history matching problems. Therefore, in this work, only the LBFGS method is used to minimize the objective function.

The LBFGS method is a member of the quasi-Newton family. Remember that the Gauss-Newton method uses the Hessian matrix to compute the search direction, which is

$$d_{k+1} = -H_k^{-1} g_k \,. \tag{4.7}$$

Here, to be consistent with the literatures about the quasi-Newton methods, d_k and g_k are used to denote the search direction and the gradient. The quasi-Newton methods, however, use an approximation to the inverse Hessian matrix to calculate the search direction,

$$d_{k+1} = -\tilde{H}_k^{-1} g_k \,, \tag{4.8}$$

where $\tilde{H}_k$ is the Hessian matrix approximation. Since the search directions are computed iteratively, there must be a scheme to update $\tilde{H}_{k+1}^{-1}$ from $\tilde{H}_k^{-1}$. In addition, the

following quasi-Newton condition must be satisfied by the updating scheme,

$$\tilde{H}_{k+1}^{-1} y_k = s_k \,, \tag{4.9}$$

where

$$y_k = g_{k+1} - g_k \,, \tag{4.10}$$

and

$$s_k = m_{k+1} - m_k \,. \tag{4.11}$$

Among a number of schemes, a very successful one was given independently by Broyden (1970), Fletcher (1970), Goldfarb (1970) and Shanno (1970), which is

$$\tilde{H}_{k+1}^{-1} = \tilde{H}_k^{-1} + \frac{s_k s_k^T y_k^T \tilde{H}_k^{-1} y_k}{y_k^T s_k y_k^T s_k} + \frac{s_k s_k^T}{y_k^T s_k} - \frac{s_k y_k^T \tilde{H}_k^{-1}}{y_k^T s_k} - \frac{\tilde{H}_k^{-1} y_k s_k^T}{y_k^T s_k} \,. \tag{4.12}$$

Eq. 4.12 can also be written as

$$\tilde{H}_{k+1}^{-1} = \left(I - \rho_k s_k y_k^T\right) \tilde{H}_k^{-1} \left(I - \rho_k y_k s_k^T\right) + \rho_k s_k s_k^T \,, \tag{4.13}$$

where,

$$\rho = \frac{1}{y_k^T s_k} \,. \tag{4.14}$$

To start the algorithm, an initial guess for the Hessian matrix approximation should be given to Eq. 4.12. Then, the Hessian matrix approximation can be updated from step to step. Although Eq. 4.12 avoids computing the true Hessian matrix, it still forms the Hessian approximation explicitly, which will occupy a large amount of storage if model size becomes big. This weakness was overcome by Nocedal (1980), who introduced a scheme to reformulate Eq. 4.13. Using his scheme, only L vectors obtained from previous iteration steps are stored, including the gradient and model parameter vector. The Hessian matrix approximation at each iteration step is not constructed explicitly any more. Instead, the multiplications of the Hessian approximation with some matrices are formed by using the L vectors (Nocedal, 1980). The length L can be decided according to different cases. The rule of thumb is that the

larger L is, the more previous information is used. For a fixed L, the scheme used when iteration step k is less than L and the scheme when $k+1 > L$ are different. If $k < L$, the scheme is,

$$\begin{aligned}\tilde{H}_{k+1}^{-1} = & V_k^T V_{k-1}^T \cdots V_0^T \tilde{H}_0^{-1} V_0 \cdots V_{k-1} V_k \\ & + V_k^T V_{k-1}^T \cdots V_1^T \rho_0 s_0 s_0^T V_1 \cdots V_{k-1} V_k \\ & \vdots \qquad\qquad\qquad\qquad\qquad\qquad , \\ & + V_k^T \rho_{k-1} s_{k-1} s_{k-1}^T V_k \\ & + \rho_k s_k s_k^T\end{aligned} \tag{4.15}$$

where,

$$V_k = I - \rho_k y_k s_k^T . \tag{4.16}$$

If $k+1 > L$, only the L most recent vectors are used:

$$\begin{aligned}\tilde{H}_{k+1}^{-1} = & V_k^T V_{k-1}^T \cdots V_{k-L+1}^T \tilde{H}_0^{-1} V_{k-L+1} \cdots V_{k-1} V_k \\ & + V_k^T V_{k-1}^T \cdots V_{k-L+2}^T \rho_0 s_0 s_0^T V_{k-L+2} \cdots V_{k-1} V_k \\ & \vdots \qquad\qquad\qquad\qquad\qquad\qquad . \\ & + V_k^T \rho_{k-1} s_{k-1} s_{k-1}^T V_k \\ & + \rho_k s_k s_k^T\end{aligned} \tag{4.17}$$

Since what is needed is the search direction d_{k+1}, in Eq. 4.15 and Eq. 4.17, $\tilde{H}_0^{-1} g_0$ is computed instead of $\tilde{H}_0^{-1}$. Also, Nocedal (1980) gave a very efficient algorithm to transform Eq 4.15 and Eq. 4.17 into vector multiplications, which avoids unwieldy matrix computations.

In Eq. 4.1, the step size is equal to 1. In many cases, the optimal step size is smaller, and a 1-D minimization problem is used to find the step size after the search direction is obtained. For non-linear objective functions, the line search is also very complicated. In this work, the step size is calculated using one iteration of the Newton-Raphson method, followed by a quadratic fit if necessary. This procedure requires one additional simulation run (Zhang, 2002).

4.2 A small synthetic case

To preliminarily test effects on automatic history matching results with integration of seismic impedance change data, a small synthetic case study was conducted.

4.2.1 Model description

This small synthetic model has 2 layers. Each layer has 10×10 gridblocks with size equal to 40 ft. The vertical size of each gridblock is 30 ft. The only model parameter that was adjusted is log of horizontal permeability. The vertical permeability is 0.1 times the horizontal permeability. The porosity value is fixed at the true value 0.2 in every gridblock, so the total number of model parameters is equal to 200, which is the number of gridblocks. To compare matching results before and after integration of seismic impedance change data, each layer is divided into three different zones of different permeability. In each zone, horizontal permeability is homogeneous. Since there are very obvious edges among these three zones, it is easy to decide if one matching result is better than another. If a method is performing well, such edges would presumably be clearer. In this example, the well rates are fixed, total reservoir rate for production well and total injection rate for injection well, and only bottom hole pressures are used as production data. The true values of log permeability in three zones are 4.0 (54.6 md), 4.2 (66.7 md), and 4.6 (99.5 md), which can be seen from Fig. 4.1. In the lower-left corner, there is a production well (white circles in Fig. 4.1(a) and Fig. 4.1(b)) and in the upper-right corner is an injection well (black circles in Fig. 4.1(a) and Fig. 4.1(b)). The injection fluid is water. The wells are completed in both layers. This is a 3-phase flow problem. Total production time is 300 days. The production well produces both oil and free gas, but has no water breakthrough.

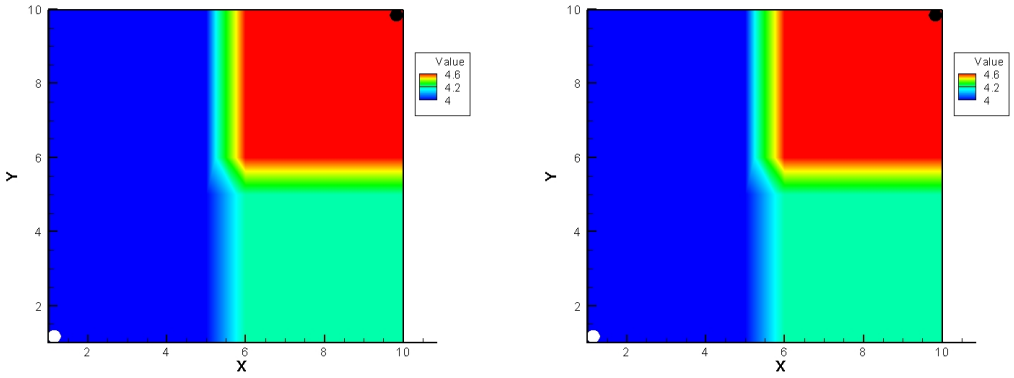

(a) Top layer (b) Bottom layer

Figure 4.1: True log horizontal permeability field

4.2.2 Matching production data only

In each well, 10 pressure data are used to do the history matching so that 20 pressure data have been used to estimate 200 model parameters. A homogeneous value, 4.0, is used as the initial guess and the prior model. Final matching results are in Fig. 4.2. From Fig. 4.2, it can be seen that from this production data alone, it is not possible to obtain a good estimate of the permeability field. The boundary between the high and low permeability regions is more like an arc than a straight line, which simply reflects the symmetry of the problem and the area of water saturation change from the injection well in that corner.

4.2.3 Combination of seismic and production data

In this section, the improvement in the estimate after the integration of seismic impedance change data for the same problem is investigated. The permeability estimate from integration of both seismic impedance change data and production data (Fig. 4.3) is better than the estimate obtained from only using production data. In particular, the boundaries of the homogeneous regions are much clearer. Compared with Fig. 4.2 and Fig. 4.1, the permeability estimate from integration of both seismic impedance change data and production data is better than the estimate obtained

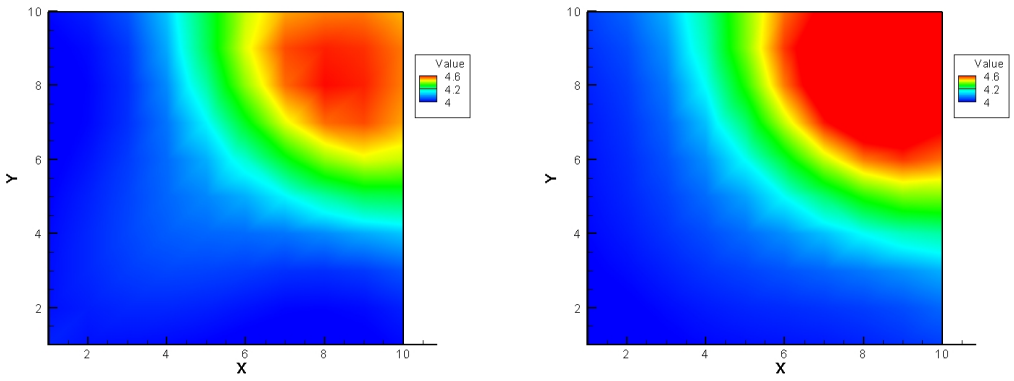

(a) Top layer (b) Bottom layer

Figure 4.2: Estimated log horizontal permeability field using production data only

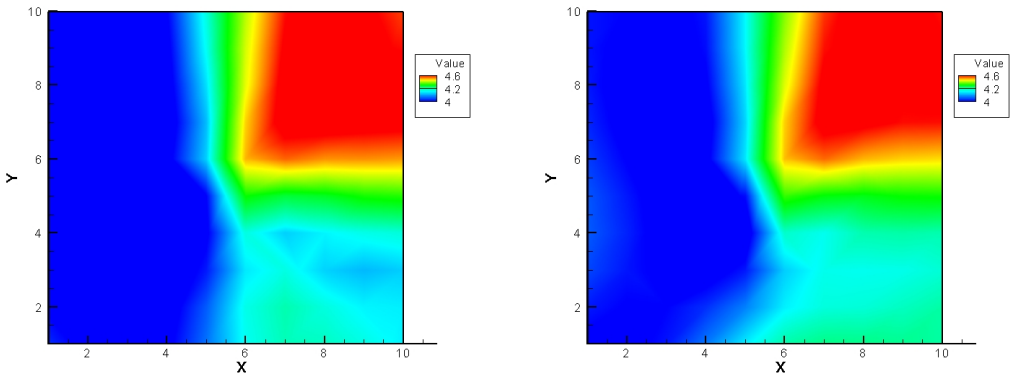

(a) Top layer (b) Bottom layer

Figure 4.3: Estimated log horizontal permeability field using seismic and production data

from only using production data. Moreover, it is much closer to the true field, especially its boundary of the homogeneous regions is much clearer. The reason for the improvement is that the spatial density of seismic impedance change data provides more constraints in gridblocks that are far from well locations. Obviously, seismic impedance change data makes the possible solution space narrower and can provide much better estimates of properties. In summary, adding seismic impedance change data into automatic history matching is feasible and provides improved estimates.

4.3 A semi-synthetic case

Automatic history matching typically becomes more difficult when the size of the model and the amount of data are both large. In this section, the results will be given by applying the method with seismic impedance data to a much larger model than the small synthetic one discussed before.

4.3.1 Model generation

Firstly, we offer an explanation for the use of the term "semi-synthetic". The ultimate goal is to apply the method to a field problem (Bay Marchand field in Chapter 5), but as an intermediate step, we applied the method to a "field-scale" problem rather than just using it on small synthetic model. One possible candidate is the model from Tengiz field provided by Chevron-Texaco to the **U**niversity of **T**ulsa **P**etroleum **R**eservoir **E**xploitation **P**rojects (TUPREP). When TUPREP obtained that data, the initial aim was to test automatic history matching on a large scale single-phase real field problem. At this time, the purpose is to investigate if seismic impedance change data can give reasonable estimates of properties in history matching problems. This goal requires comparison with a true field. The first five layers of the reservoir created by Chevron-Texaco was used as the true geological model. The reservoir properties would presumably be unknown, except for observations at well locations. The true model was also used to generate the observed seismic impedance change

data. Using a covariance estimated from the Chevron-Texaco model, a new synthetic model was generated by **S**equential **G**aussian **S**imulation (SGS). A comparison of the Chevron-Texaco model of Tengiz field with the generated model can be seen from Table 4.1, where C-T is used to stand for Chevron-Texaco and S-S denotes Semi-Synthetic. Tengiz field has a very high initial reservoir pressure and relatively low

Parameters	**C-T Model**	**S-S Model**
True model	N/A	From C-T
Prior model	Synthetic model	Generated by SGS
Well locations	Actual	Same as C-T model
Well rates	Variable	Constant
Number of wells	40	30
Well completion	Partially perforated	Fully perforated
Initial reservoir pressure	$11,950$ psi	$4,000$ psi
Bubble point pressure	$3,586$ psi	$3,586$ psi
Number of layers	9	5
Gridblocks in each layer	59×49	59×49
Gridblock size	Variable (actual)	Same as C-T model
Production time	Actual	$3,600$ days

Table 4.1: Comparison between Tengiz field and the semi-synthetic model

bubble point pressure. Under such conditions, it would remain single-phase even after a long production period. If only the pressure changes in the reservoir, then the seismic impedance change will be very small, and the field would not be a good candidate for time-lapse seismic. In order to make the model a viable candidate for time-lapse seismic, the initial reservoir pressure was changed to be slightly above the bubble point pressure, to ensure that a gas phase develops soon after production begins. Among the three fluid phases, oil, water, and gas, the gas phase has the smallest bulk modulus; usually two orders lower than that of oil or water. The low bulk modulus for gas results in a significant effect on seismic impedance change.

SGS was used to generate the prior porosity field, which also served as the initial guess. The prior horizontal permeability field was generated directly from the porosity

field using a functional relationship. The correlation equation,

$$\ln k_h = 2.41073 - 7.3652 \times \exp\left(-\frac{\phi}{0.04419}\right), \tag{4.18}$$

is generated from a cross plot of porosity and horizontal permeability in well locations in the reference model. This functional relationship fits better than standard linear relationship between $\ln k_h$ and ϕ. The prior horizontal permeability field was computed directly from Eq. 4.18 once the porosity field had been simulated. The relationship between vertical and horizontal permeability was also estimated from a cross plot. A satisfactory relationship is provided by

$$k_v = a \times k_h\,, \tag{4.19}$$

where, a is a constant multiplier. In this semi-synthetic model, 0.002 was used to compute the vertical permeability field.

The true log horizontal permeability field and porosity field from layer 1 to layer 4 are shown in Fig. 4.4 and Fig. 4.5. The true log horizontal permeability field and porosity field at the 5th layer are shown in Fig. 4.6. From the true permeability and porosity fields, we can see an obvious discontinuity in properties between the left lower part and the right upper part of the reservoir in each layer. This is a depth effect; higher porosities and permeabilities occur at shallower depths. The prior porosity field from layer 1 to layer 5 is shown in Fig. 4.7. No information was added about the depth effect when the prior model was generated so there is no discontinuity in Fig. 4.7. Because the prior log horizonal permeability field was generated from the prior porosity field using Eq. 4.18, it has the same features as those in the prior porosity field so they are not shown here. Most of the wells are located in the plateau area, which gives more gas after production than in the low permeability and porosity area. This difference makes the seismic impedance change quite different in these two areas, which can be seen in Fig. 4.8. In the deeper region, because of lower gas saturation, the seismic impedance change value is low. The region on the right side

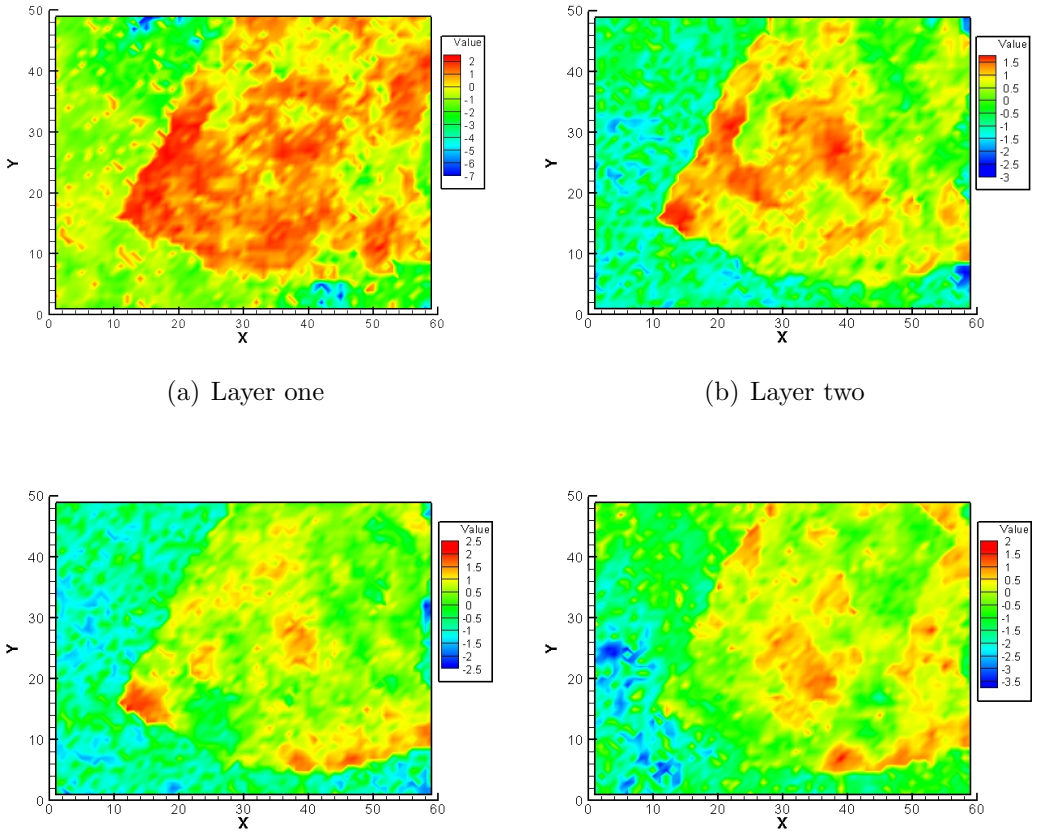

(a) Layer one

(b) Layer two

(c) Layer three

(d) Layer four

Figure 4.4: True log horizontal permeability field from layer 1 to layer 4

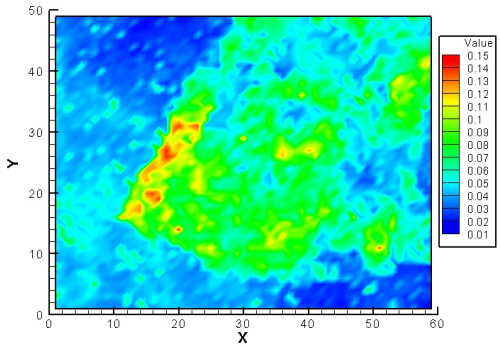

(a) Layer one

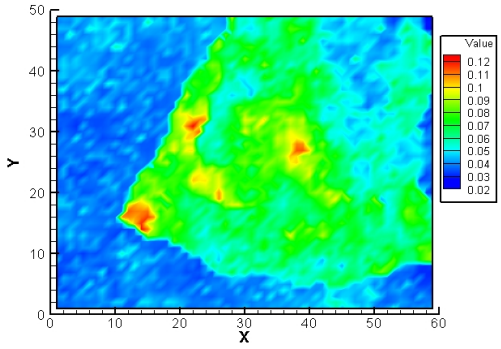

(b) Layer two

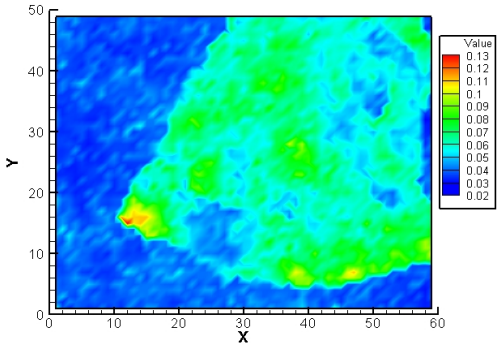

(c) Layer three

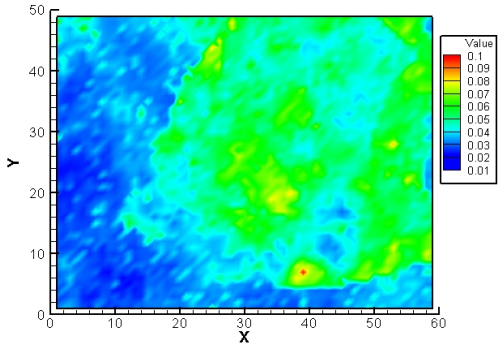

(d) Layer four

Figure 4.5: True porosity field from layer 1 to layer 4

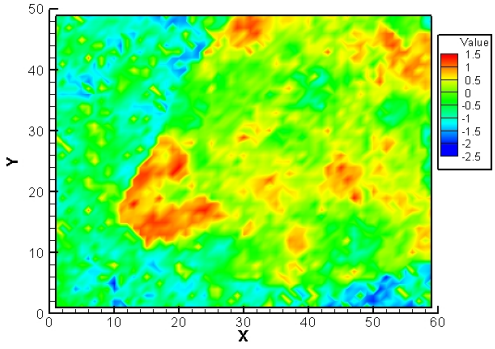

(a) Log permeability

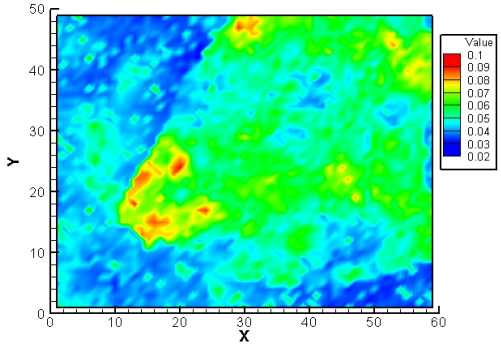

(b) Porosity

Figure 4.6: True log horizontal permeability and porosity fields at layer 5

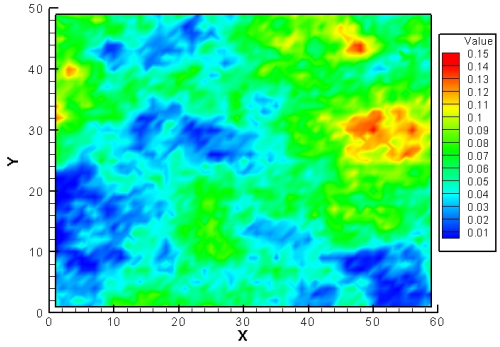

(a) Layer one

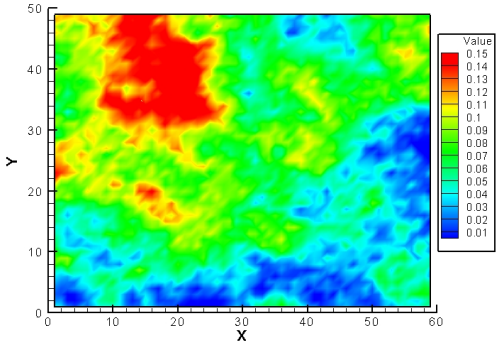

(b) Layer two

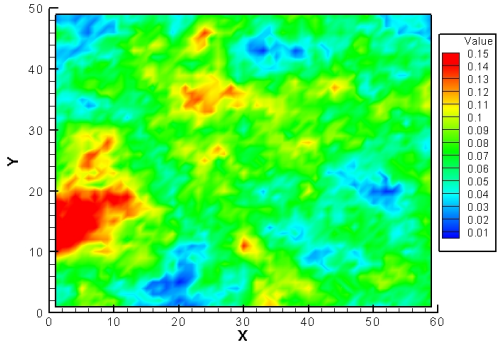

(c) Layer three

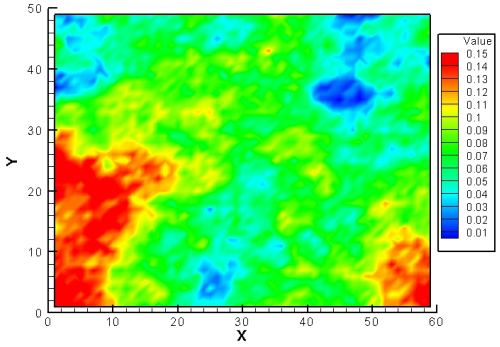

(d) Layer four

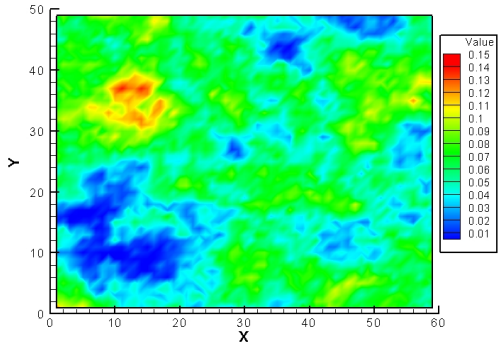

(e) Layer five

Figure 4.7: Prior porosity field from layer 1 to layer 5

has a higher value because of higher gas saturation. Moreover, with increase of depth, reservoir pressure becomes higher, which makes it more difficult for gas to come out of solution, so seismic impedance change is smaller in the deeper layers. The observed seismic impedance change data were computed based on the true saturations and pressures using the Gassmann and Han equations. The required mineral parameters, such as shaliness, bulk modulus of sand and bulk modulus of clay, used the typical values shown in Table 3.4. Since same values of the parameters were used for both history matching phase and observation generation, there is no model error for time-lapse seismic data, which is also an advantage of synthetic case study. The first seismic survey was assumed to be "shot" before the production began and the second survey was assumed to be "shot" at the last day of the history matching period (day 3600). Since an impedance change value could be computed for each simulation gridblock, according to the pressure and saturation in that gridblock, up-scaling or downscaling was not necessary. This is one difference between a synthetic case and a real field case, where up-scaling and downscaling are almost inevitable (Aanonsen et al., 2003; Gosselin et al., 2003).

There are four sub-matrices in the model covariance matrix C_M. They are $C_{\phi\phi}$, $C_{\phi k}$, $C_{k\phi}$ and C_{kk}. Due to symmetry, $C_{\phi k}$ is same as $C_{k\phi}^T$. Since a positive correlation coefficient, 0.6, was used for the horizontal permeability and the porosity in this case, the C_M matrix is not block diagonal. $C_{\phi\phi}$ and C_{kk} were constructed using the same variogram function with different sill values. The cross-covariance parts, $C_{k\phi}$ and $C_{\phi k}$, also have the same variogram structure, but needed to be multiplied by the correlation coefficient (Xu et al., 1992).

In this semi-synthetic model, there are 30 wells. All of them are produced with constant total reservoir rates as targets, $4,000$ BBL/Day, and minimum bottomhole pressure as constraints, $1,200$ psia. All the wells have free gas produced but none have water breakthrough. Therefore, available production data include pressure P_{wf}

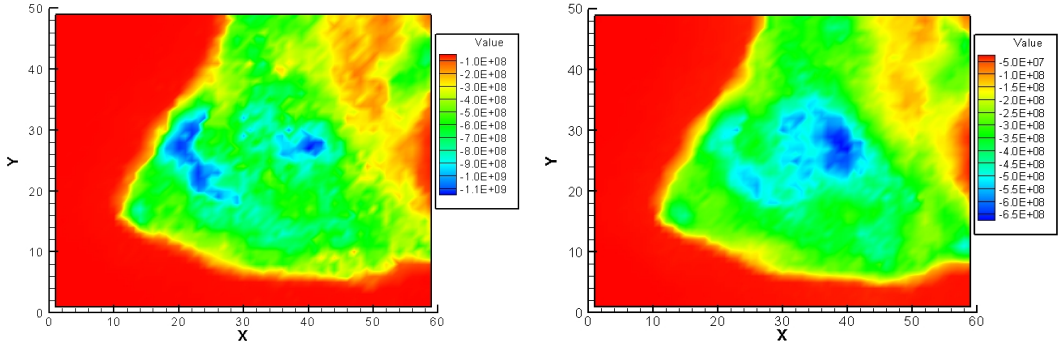

(a) Layer one

(b) Layer two

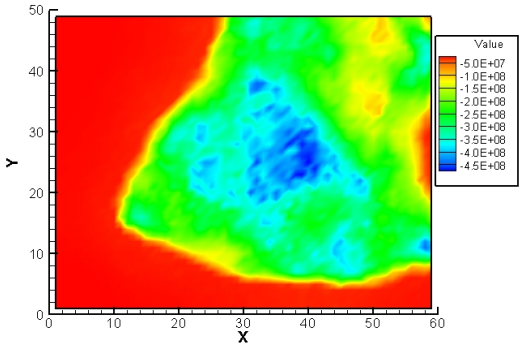

(c) Layer three

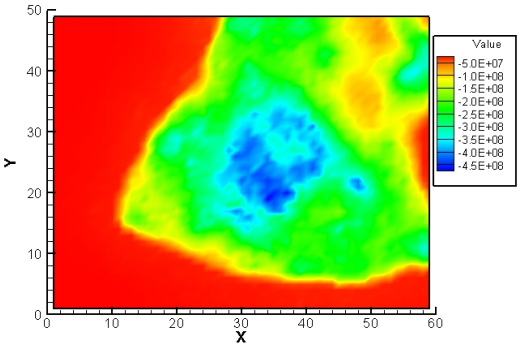

(d) Layer four

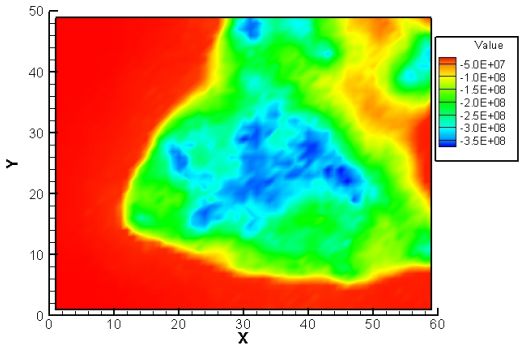

(e) Layer five

Figure 4.8: Observed seismic impedance change from layer 1 to layer 5

and GOR. To show the effects from integration of seismic impedance change data, two history matching studies were conducted. One used P_{wf} and seismic impedance change data. The other used P_{wf}, GOR, and seismic impedance change data. We will see that in this case, only when seismic data are used can the features of the true field be recovered, regardless of how many types of production data are used.

4.3.2 History matching with P_{wf} and seismic data

The model parameters include porosity and horizontal permeability at each gridblock. In total, there are $28,910$ parameters. The number of seismic impedance change data is equal to the number of gridblocks, $14,455$. In each well, there are three P_{wf} data, so totally the number of observation data is $14,545$, which is still less than the number of model parameters.

In Fig. 4.9, Fig. 4.10, and Fig. 4.11, porosity and log horizontal permeability estimations at all 5 layers are shown. Compared with the prior fields and the true fields, it is obvious that integration of only P_{wf} data does not provide satisfactory estimation. The important boundary between the plateau area and the left region with low permeability and porosity can not be recovered because few constraints are available for that area. After seismic impedance change data are integrated as well as P_{wf} data, the estimated results are totally different, see Fig 4.12, Fig. 4.13, and Fig. 4.14. The estimates capture some important features of the true models, including the boundaries between the high value region and the low value region in both the permeability field and the porosity field. From layer 1 to 5, both the permeability and the porosity fields are resolved better in the plateau area because the true seismic impedance changes have higher values there due to the depth effect. Since no any prior information was added about the reduction of porosity and permeability with depth, such differences are obviously from the different seismic impedance change data at these two regions.

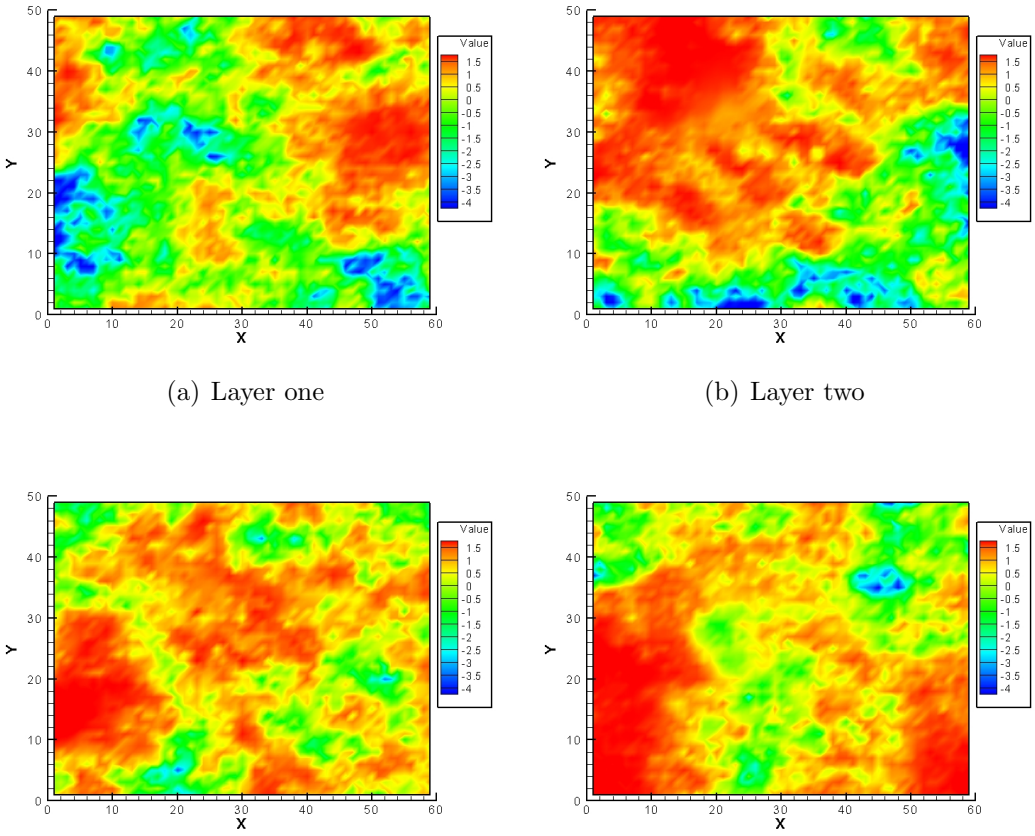

(a) Layer one

(b) Layer two

(c) Layer three

(d) Layer four

Figure 4.9: Estimated log horizontal permeability field from layer 1 to layer 4 using P_{wf} data only

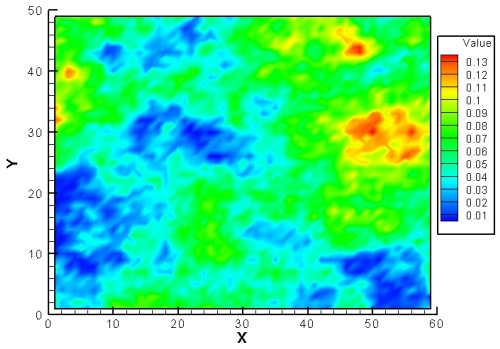

(a) Layer one

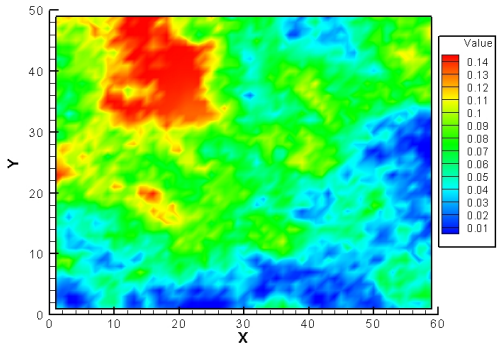

(b) Layer two

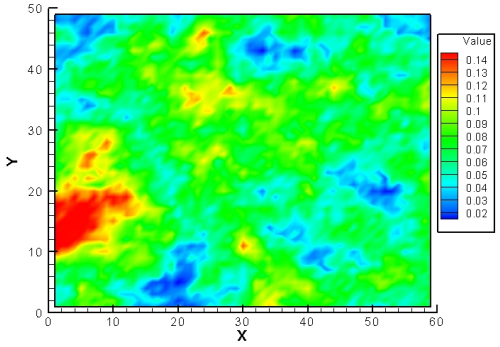

(c) Layer three

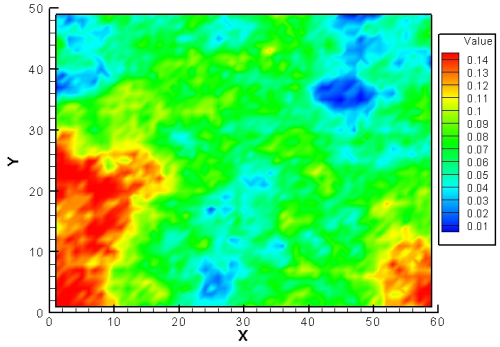

(d) Layer four

Figure 4.10: Estimated porosity field from layer 1 to layer 4 using P_{wf} data only

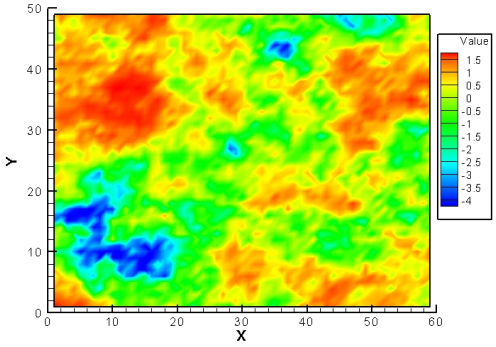

(a) Log permeability

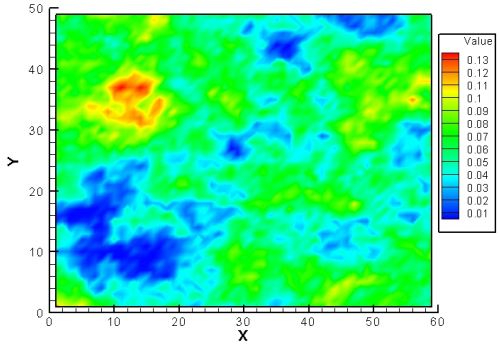

(b) Porosity

Figure 4.11: Estimated log horizontal permeability and porosity fields at layer 5 using P_{wf} data only

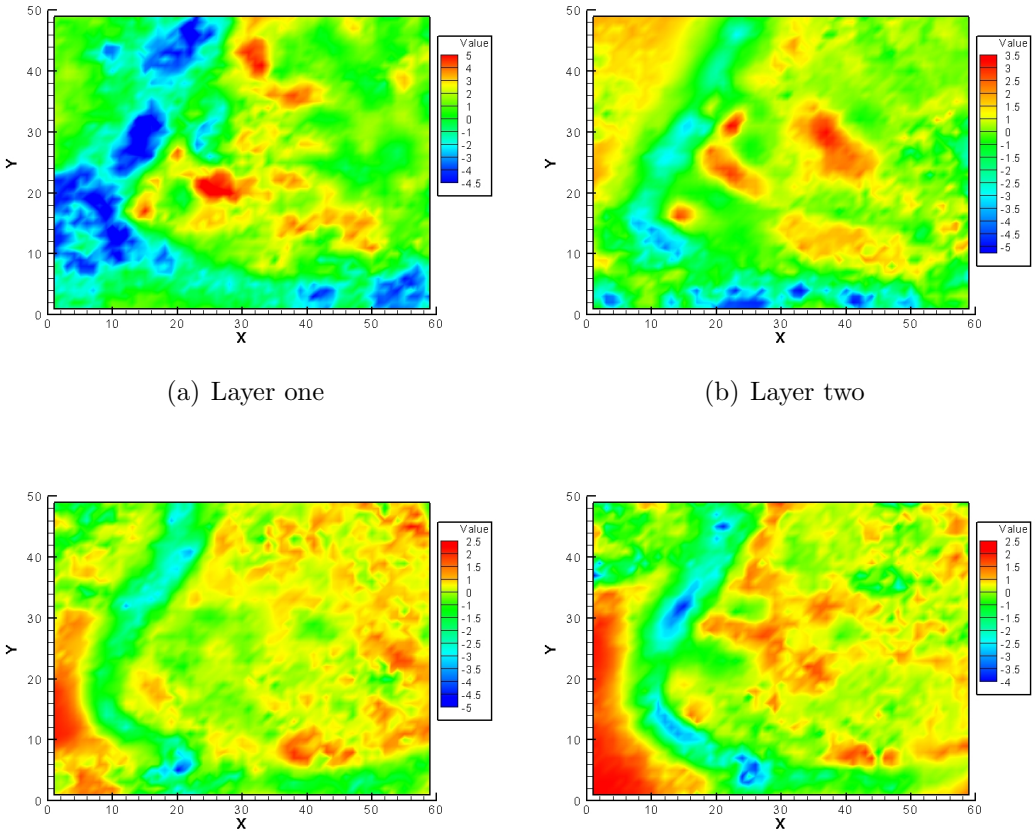

(a) Layer one

(b) Layer two

(c) Layer three

(d) Layer four

Figure 4.12: Estimated log horizontal permeability field from layer 1 to layer 4 using seismic impedance change data and P_{wf} data

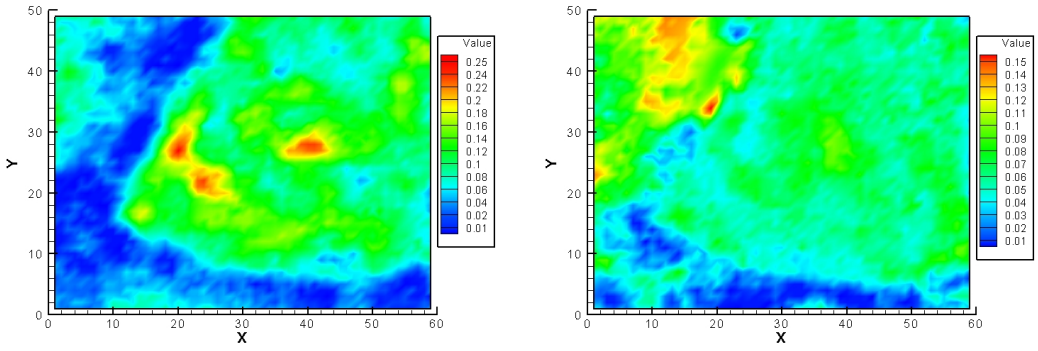

(a) Layer one

(b) Layer two

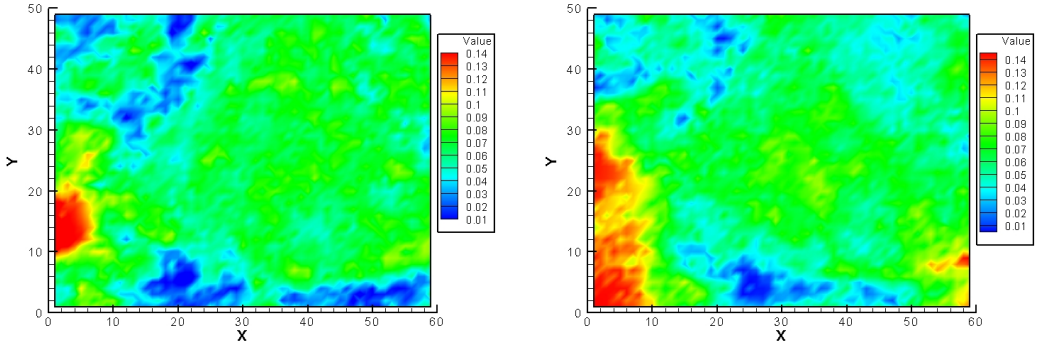

(c) Layer three

(d) Layer four

Figure 4.13: Estimated porosity field from layer 1 to layer 4 using seismic impedance change data and P_{wf} data

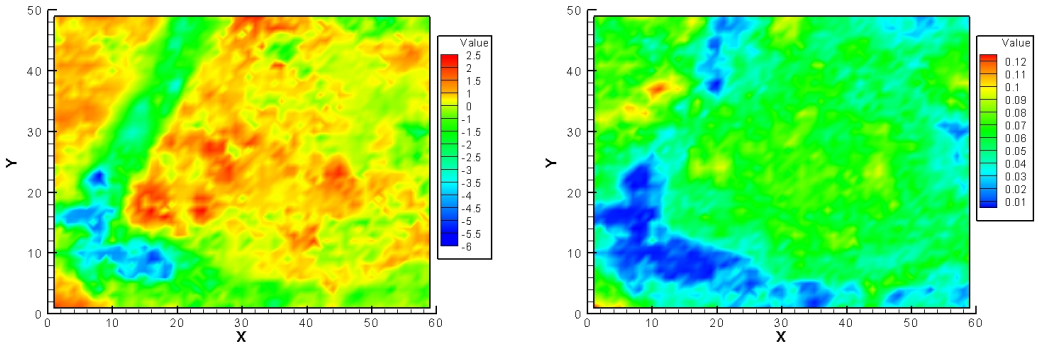

(a) Log permeability

(b) Porosity

Figure 4.14: Estimated log horizontal permeability and porosity fields at layer 5 using seismic impedance change data and P_{wf} data

The computational seismic impedance change data after history matching are shown in Fig. 4.15. The history matched seismic impedance change data are very similar to the observed impedance change data (Fig. 4.8), in both the field scale structures, for example the boundary, and the detailed features within the plateau area. The difference between the computed and the observed seismic impedance change data is much smaller than that between the estimated models (Fig 4.12, Fig. 4.13, and Fig. 4.14) and the true models (Fig. 4.4, Fig. 4.5, and Fig. 4.6).

To show the estimation quality more clearly, cross plots are shown in Fig. 4.16, between estimated permeability, porosity and computed impedance, and the true permeability, porosity and observed impedance at layer 1 and 5. The red lines in the cross plots are linear regression lines, which all have the same form as,

$$Y = A + B * X \,, \tag{4.20}$$

where Y denotes the computational or estimated values and X stands for the observation or true values. The values of A, B, and the correlation coefficient R of the regression lines are listed in Table 4.2. From Table 4.2, it can be seen that the results

Parameters	A	B	R
Log horizontal permeability at layer 1	0.39226	0.83298	0.54722
Log horizontal permeability at layer 5	0.02615	0.76684	0.4170
Porosity at layer 1	0.00644	1.58662	0.73467
Porosity at layer 5	0.02416	0.58047	0.3102
Seismic impedance change at layer 1	-1.6772×10^6	0.97934	0.99286
Seismic impedance change at layer 5	3.3583×10^6	0.98658	0.99392

Table 4.2: Parameters of regression lines and correlation coefficients for cross plots of log horizontal permeability, porosity, and seismic impedance change at layer 1 and layer 5 (seismic impedance change data and P_{wf} data)

in layer 1 are better than the results in layer 5, but the correlation between the truth and the estimates is only marginal in all cases. It is also clear from the plots and from the correlation coefficients (Table 4.2) that the automatic history matching procedure

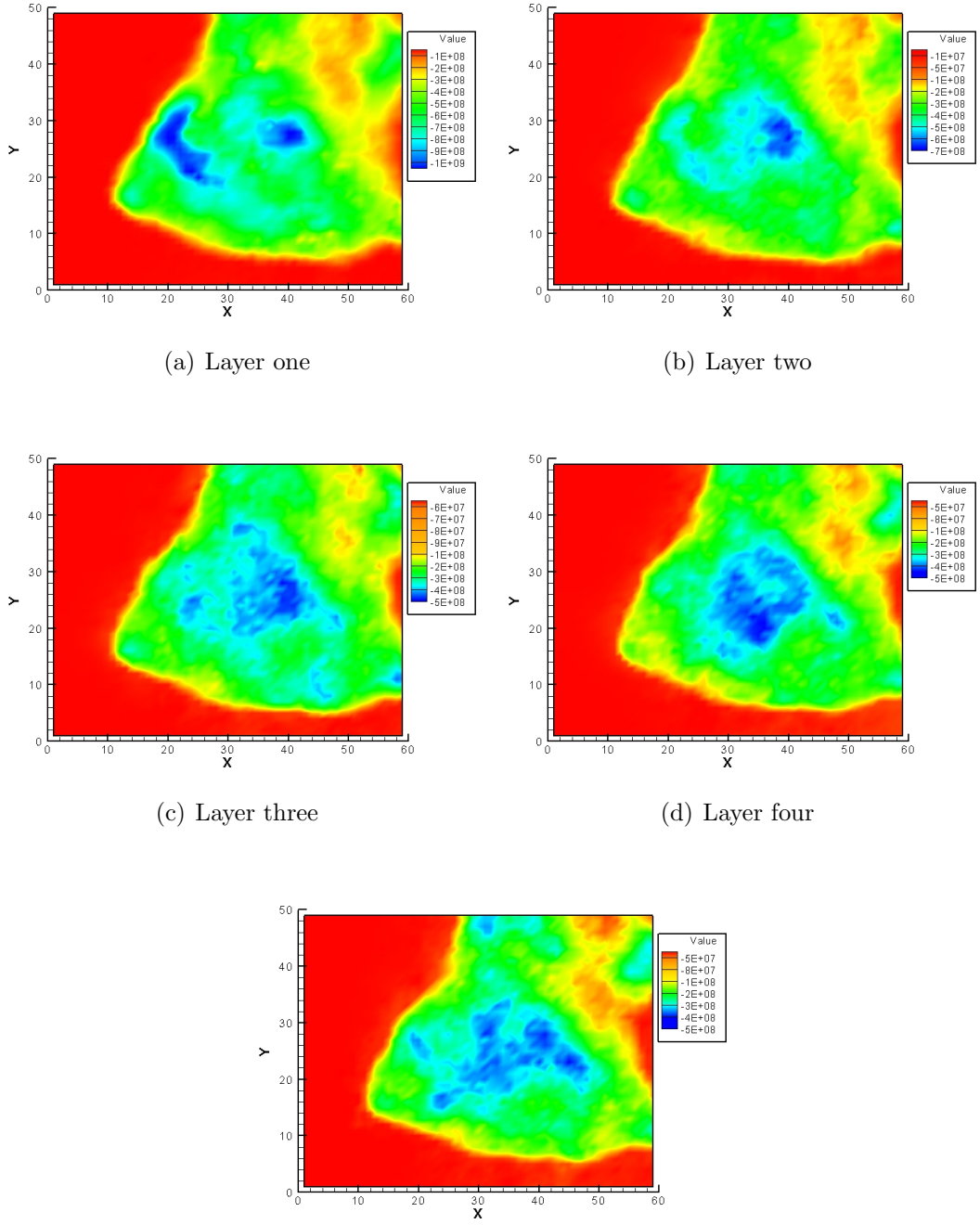

(a) Layer one

(b) Layer two

(c) Layer three

(d) Layer four

(e) Layer five

Figure 4.15: Computational seismic impedance change data from layer 1 to layer 5

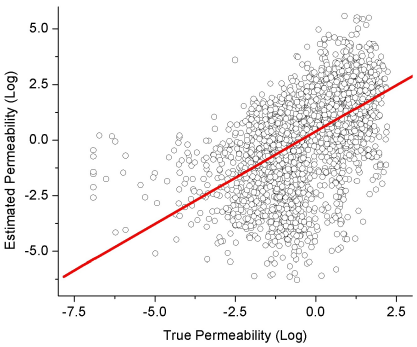

(a) Log horizontal permeability at layer 1

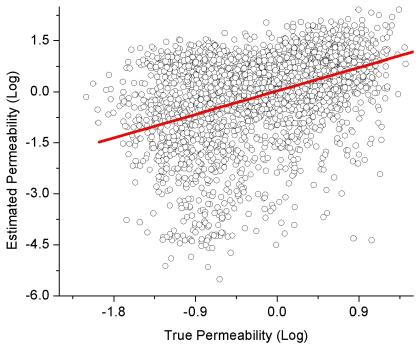

(b) Log horizontal permeability at layer 5

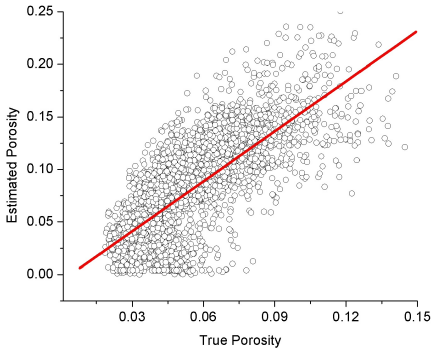

(c) Porosity at layer 1

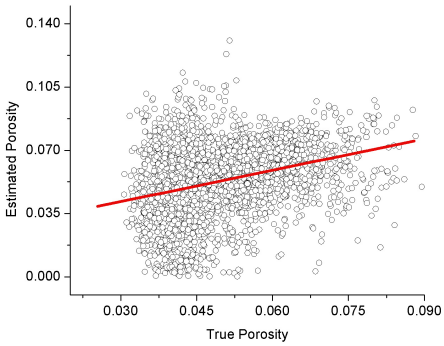

(d) Porosity at layer 5

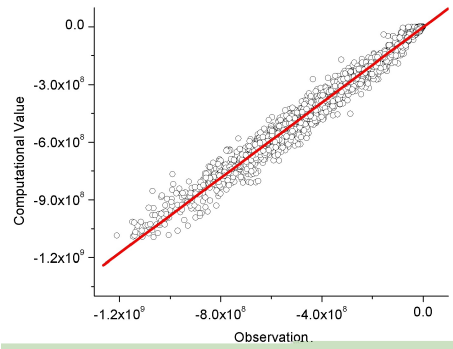

(e) Impedance change at layer 1

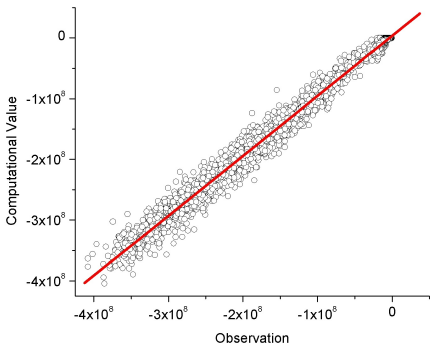

(f) Impedance change at layer 5

Figure 4.16: Cross plots of log horizontal permeability, porosity, and seismic impedance change at layer 1 and layer 5

has done an excellent job of matching the seismic impedance change data in layers 1 and 5. On the other hand, the relatively poor correlations between the estimated and the true permeability and porosity demonstrate the non-uniqueness in the problem of estimating reservoir parameters, even from high quality synthetic time-lapse seismic data.

It is clear in Fig. 4.16(a), Fig. 4.16(b), Fig. 4.16(c), and Fig. 4.16(d) that the maximum values of the estimated fields are larger than the maximum values of the true fields. The problem of over-shooting, has been noted previously in automatic history matching (Gao and Reynolds, 2004). In their investigation, over-shooting problems were effectively depressed by using suitable transforms.

To show the effect of seismic impedance change data more clearly, GOR and oil rate predictions are compared in Fig. 4.17, where "Production" denotes that the curve is generated from the model after integration of only P_{wf} data, and "Seismic & Production" denotes that the curve is generated from the model after integration of both seismic impedance change data and P_{wf} data. All models were run in the reservoir simulator to $6,000$ days. During the first $3,600$ days, which is also the history matching period, all wells were produced at constant total rate, $4,000$ BBL/Day, and were also constrained to a minimum bottom hole pressure of $1,200$ psia. From $3,600$ days to $6,000$ days, all wells produced at fixed bottom hole pressures equal to the values at $3,600$ days. From Fig. 4.17, it can be seen that the oil rate and GOR value predictions from both estimated models are closer to the true model than the initial model. Furthermore, the prediction from integration of both seismic impedance change data and production data is better than the prediction from the history match of production data only.

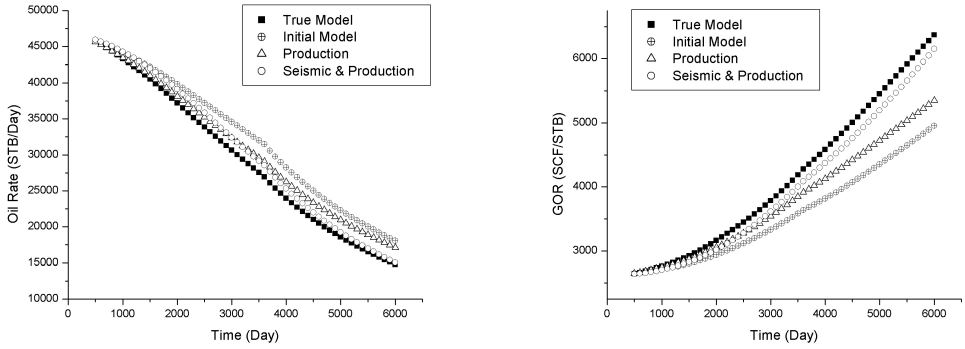

(a) Oil production rate (b) GOR

Figure 4.17: Predictions of oil production rate and GOR using the true model, initial model, P_{wf} data history matched model, and seismic and P_{wf} data history matched model

4.3.3 History matching with P_{wf}, GOR, and seismic data

In this scenario, GOR data as well as P_{wf} data are integrated. Each well has three GOR data and three P_{wf} data so the total number of production data is 180. The true model, the initial model, and the seismic impedance change observations are not shown here because they are the same as that used in the previous section.

Figs. 4.18 to 4.20 show estimates obtained using only P_{wf} data and GOR data. Although the results in layer 2 and layer 3 (Fig. 4.18(b) and Fig. 4.18(c)) are different from their counterparts using P_{wf} data only (Fig. 4.9(b) and Fig. 4.9(c)), neither were effective at recovering the depth effect in the true field, see Fig. 4.4(b) and Fig. 4.4(c). The porosity fields have similar problems.

After seismic impedance change data are integrated, however, the estimates of log horizontal permeability and porosity are greatly improved, see Fig. 4.21, Fig. 4.22, and Fig. 4.23. The most important and obvious changes are that the boundary between the shallow and deep regions is recovered well, especially in layer 1. In this example, it can be seen that seismic is still crucial for capturing the features of the true models. There are two main reasons for the poor results for automatic history matching with integration of production data only. One is that the number of

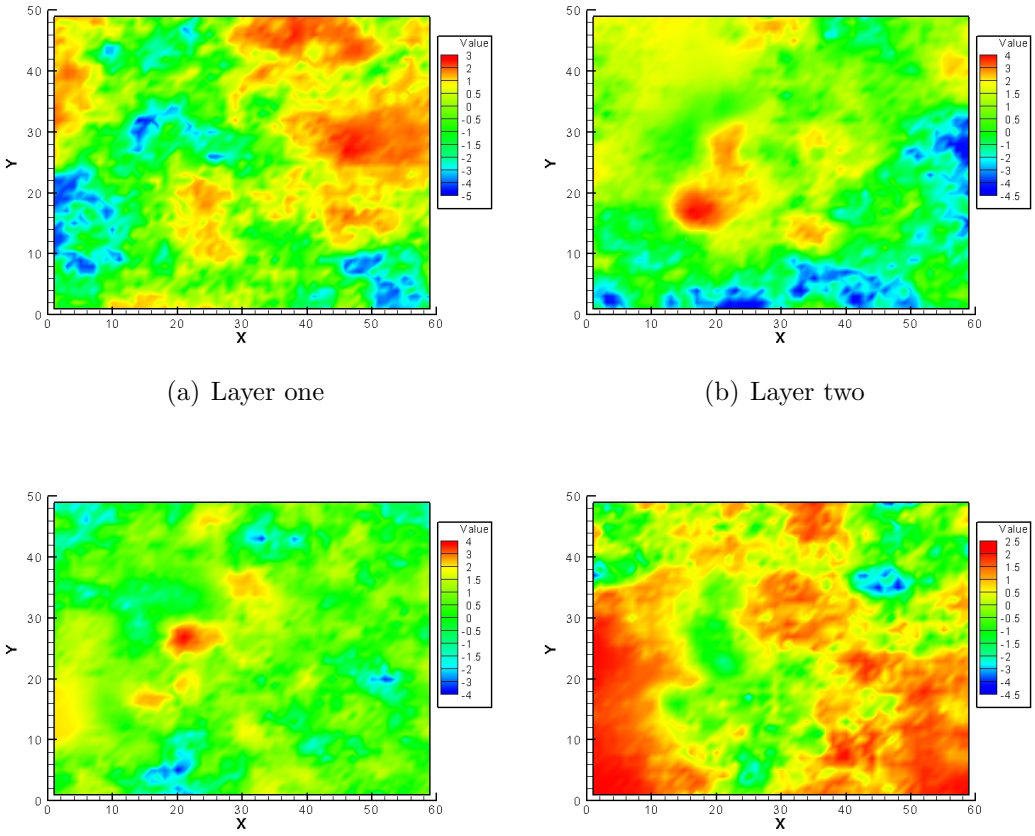

(a) Layer one

(b) Layer two

(c) Layer three

(d) Layer four

Figure 4.18: Estimated log horizontal permeability field from layer 1 to layer 4 using P_{wf} and GOR data only

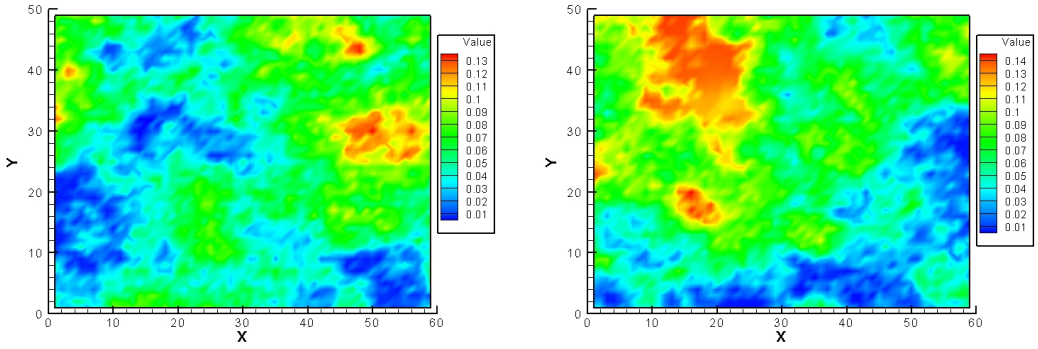

(a) Layer one

(b) Layer two

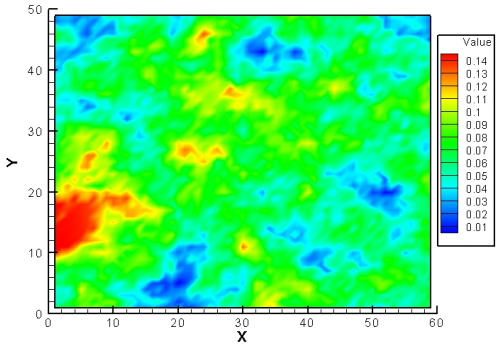

(c) Layer three

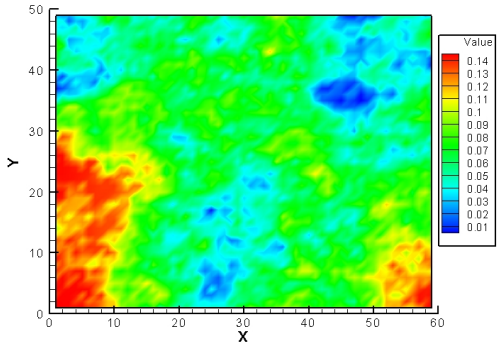

(d) Layer four

Figure 4.19: Estimated porosity field from layer 1 to layer 4 using P_{wf} and GOR data only

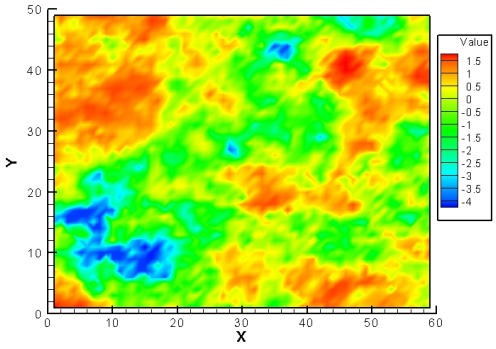

(a) Log permeability

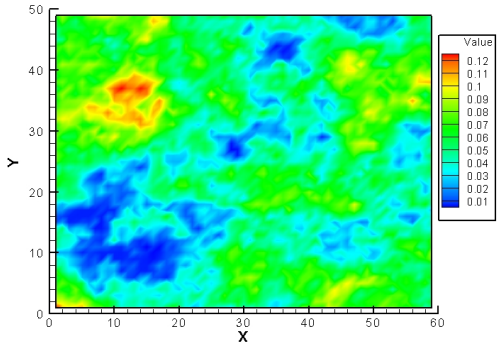

(b) Porosity

Figure 4.20: Estimated log horizontal permeability and porosity fields at layer 5 using P_{wf} and GOR data only

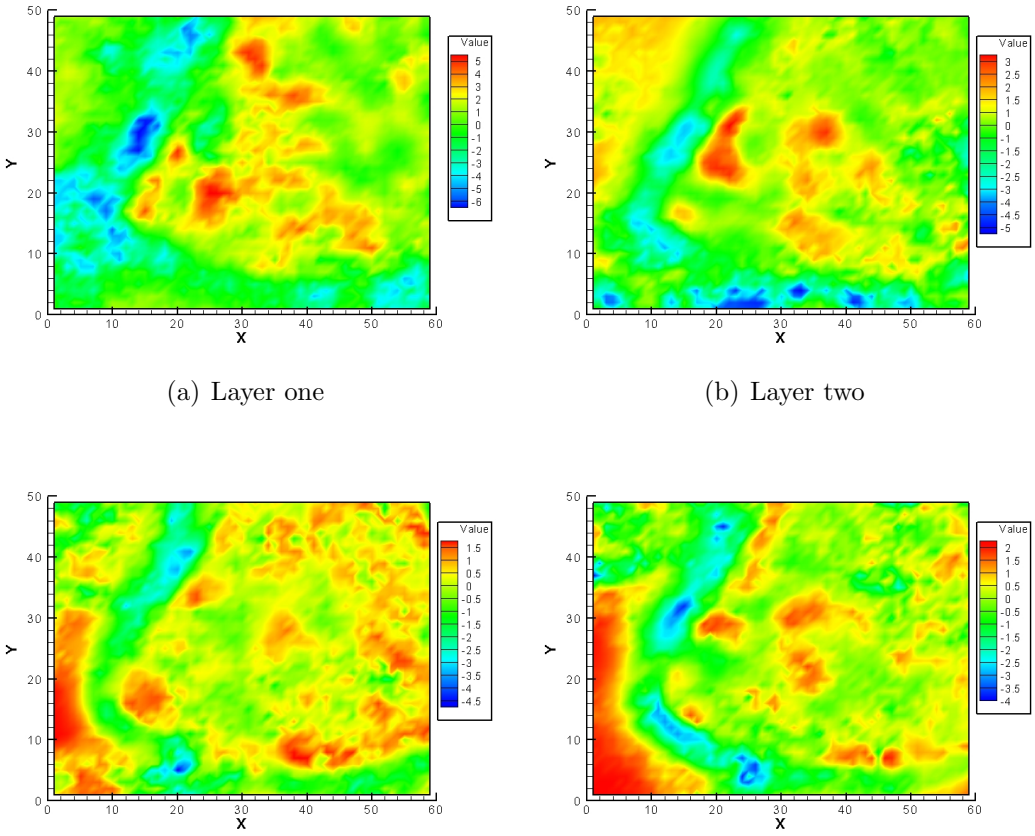

(a) Layer one

(b) Layer two

(c) Layer three

(d) Layer four

Figure 4.21: Estimated log horizontal permeability field from layer 1 to layer 4 using seismic impedance change data, P_{wf}, and GOR data

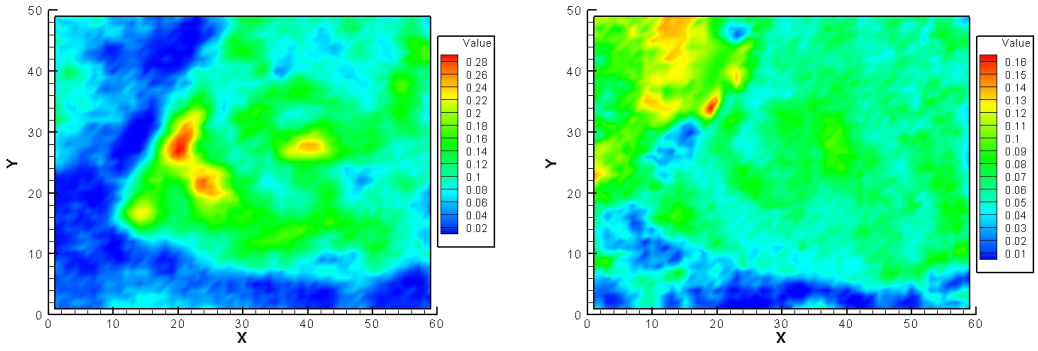

(a) Layer one

(b) Layer two

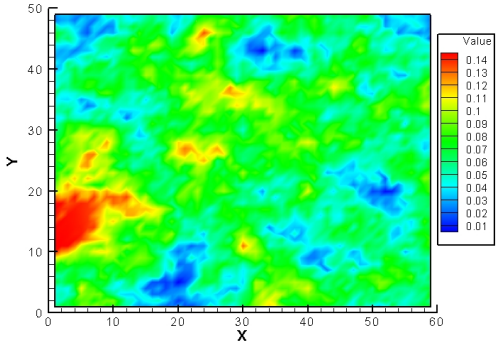

(c) Layer three

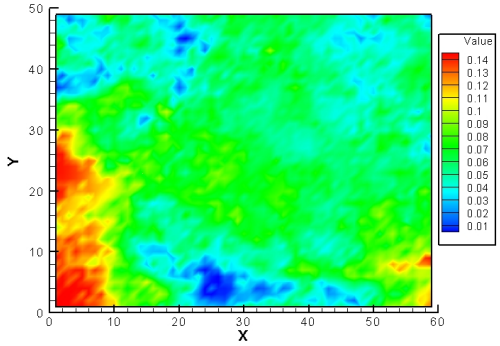

(d) Layer four

Figure 4.22: Estimated porosity field from layer 1 to layer 4 using seismic impedance change data, P_{wf}, and GOR data

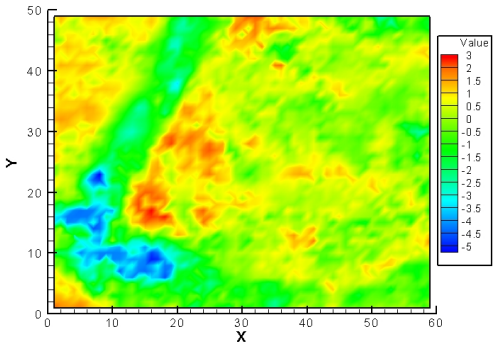

(a) Log permeability

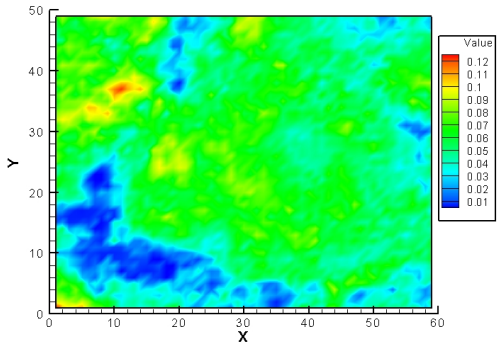

(b) Porosity

Figure 4.23: Estimated log horizontal permeability and porosity fields at layer 5 using seismic impedance change data, P_{wf}, and GOR data

production data is small compared with the number of model parameters. The other is that the wells are located close to each other in the plateau area, which makes the regions to the left of the boundary lack of constraints.

The computational seismic impedance change data at the last iteration step are shown in Fig. 4.24. The computed impedances in all layers match well with the observed seismic impedance (Fig. 4.8), in terms of both the boundary between high permeability/porosity region and the low permeability/porosity region, and the detailed structures within the plateau area. Cross plots of computed and observed values are shown in Fig. 4.25. A regression line, $Y = A + B * X$, is used to fit the scatter points. The coefficients, A and B, and the correlation coefficients R of the regression analysis are listed in Table 4.3. It can be seen that porosity field has been

Parameters	A	B	R
Log horizontal permeability at layer 1	0.42014	0.85549	0.55021
Log horizontal permeability at layer 5	-0.0437	0.66576	0.38373
Porosity at layer 1	-0.01556	1.82009	0.76161
Porosity at layer 5	0.02606	0.52942	0.2916
Seismic impedance change at layer 1	-2.77013×10^6	0.97332	0.99177
Seismic impedance change at layer 5	3.33676×10^6	0.99004	0.99413

Table 4.3: Parameters of regression lines and correlation coefficients for cross plots of log horizontal permeability, porosity, and seismic impedance change at layer 1 and layer 5 (seismic impedance change data, P_{wf} data, and GOR data)

better estimated than the permeability field because the seismic impedance change data are more sensitive to porosity than to permeability. The shallower layer is better estimated because the seismic impedance change there is larger. Also, the seismic impedance change data have been honored very well, while the correlations between the estimated model parameters and the true model parameters are still marginal. Thus, the history matched models shown here are just one of many possible solutions.

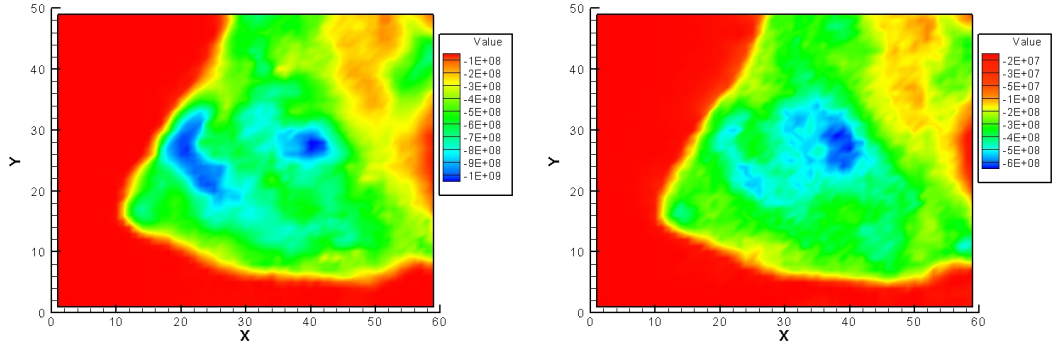

(a) Layer one

(b) Layer two

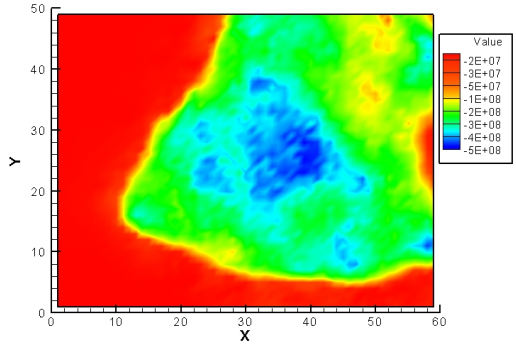

(c) Layer three

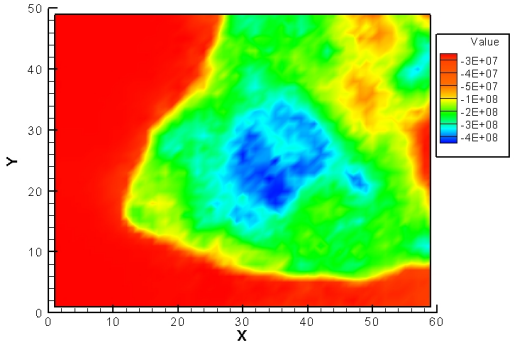

(d) Layer four

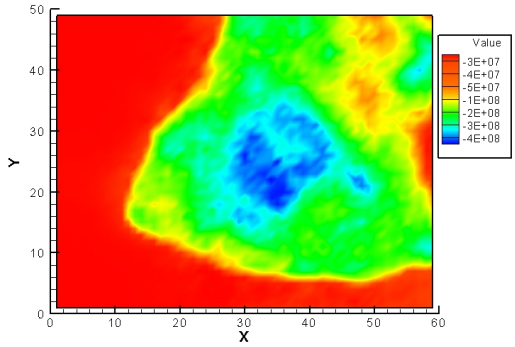

(e) Layer five

Figure 4.24: Computational seismic impedance change data from layer 1 to layer 5

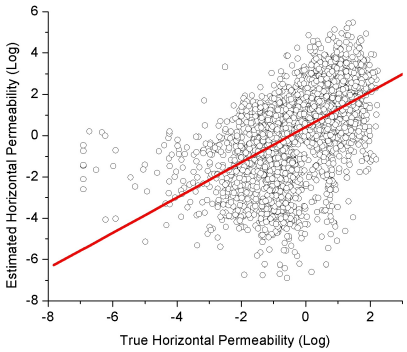

(a) Log horizontal permeability at layer 1

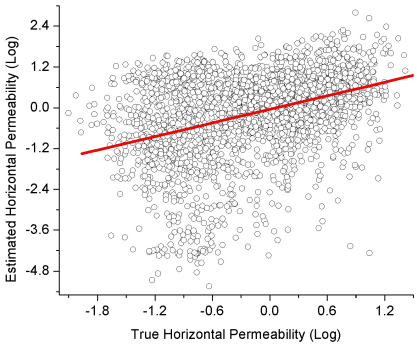

(b) Log horizontal permeability at layer 5

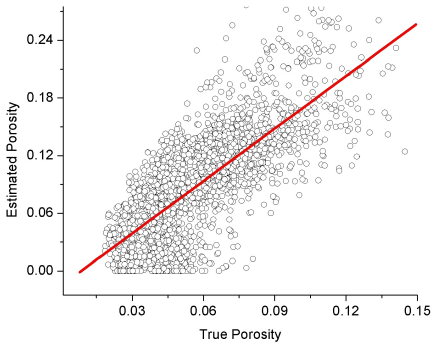

(c) Porosity at layer 1

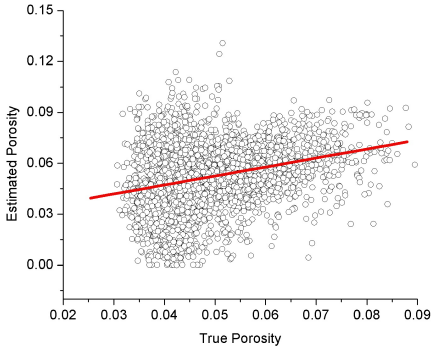

(d) Porosity at layer 5

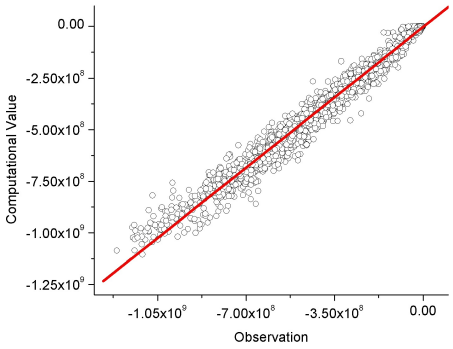

(e) Impedance change at layer 1

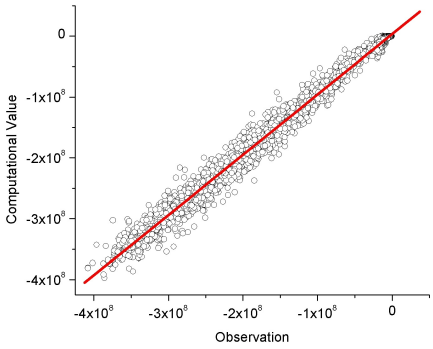

(f) Impedance change at layer 5

Figure 4.25: Cross plots of log horizontal permeability, porosity, and seismic impedance change at layer 1 and layer 5 (seismic impedance change data, P_{wf} data, and GOR data are used)

4.4 Summary

In this chapter, a procedure has been presented for automatically adjusting the permeability and porosity of grid cells to honor both time-lapse seismic data and production data. One of the rock physics models, which had been embedded into CLASS, was used to compute the seismic impedance. The LBFGS method used for minimization provided rapid minimization without the need to compute the Hessian matrix, which is very expensive in large-scale problems. The adjoint method allowed efficient computation of the gradient of the objective function with respect to model parameters when both the number of model parameters $(28,910)$ and the number of data (around $14,455$) are large. Because the reservoir simulator was used, the resulting pressure and saturation distributions were forced to honor flow equations and material balance. A small synthetic case showed that the inclusion of seismic impedance change data (from time-lapse seismic) in automatic history matching helped resolve the edges between zones with different properties. A much larger example derived from Tengiz field showed the potential for application to field-scale problems. The boundaries between different zones were captured at the estimated models. Although the data (change in impedance) were matched very well, the model variables (porosity and horizontal permeability) were not well constrained. P-wave impedance change with production data is clearly insufficient to resolve the property field. However, by comparing the prediction behavior using true model and estimated models, it was clear that integration of seismic impedance change data provided improved estimates of future prediction.

CHAPTER V

A REAL CASE STUDY FROM BAY MARCHAND FIELD, GULF OF MEXICO

Located 65 to 70 miles south of New Orleans with water depths ranging from 10 to 50 ft, the Bay Marchand field is a mature field in the Gulf of Mexico (Abriel et al., 1991). The Bay Marchand field has a series of complex faults with a salt dome nearby. Production in the field started in 1949. In late 1960's and early 1970's, the field reached its production peak. According to reports by Abriel et al. (1991) and Behrens et al. (2002), its peak production rate was around $75,000$ BOPD.[1] When the first seismic survey was conducted by Chevron in 1987, the field production had been reduced to about $18,000$ BOPD. But the successful drilling plan that followed the seismic survey boosted the production rate back up to $40,000$ BOPD in 1991 (Abriel et al., 1991; Behrens et al., 2002). Before the second seismic survey was shot in 1998 by Geco-Prakla, which is now WesternGeco, there were over 800 wells in the field. These two 3-D seismic surveys consist of the data used for the time-lapse seismic project in the Bay Marchand field although they were not designed on purpose for that aim. In this work, the main focus is on the the 7100 Sand, which is one of the many reservoirs in the north flank of the Bay Marchand field. The reservoir temperature is about 176°F and the oil gravity (API) is 19°.

A fine grid reservoir simulation model with $140 \times 53 \times 57$ gridblocks was provided by Chevron-Texaco. The porosity field extracted from layer 22 is shown in Fig. 5.1. It is obvious that the region at right side has good porosity values, while the left

[1]BOPD denotes **B**arrels **O**il **P**er **D**ay. 1 BOPD equals to 0.15897 m^3/day oil.

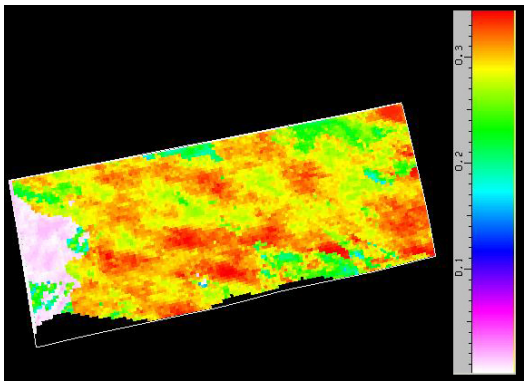

Figure 5.1: Porosity field at layer 22 extracted from the fine simulation grid

part is very tight with low porosities due to channel sand diminution (Behrens et al., 2002). The average porosity in the channel sand area for the whole 7100 Sand is around 0.3 (see Fig. 5.2). The secondary peak located at the left are from the very

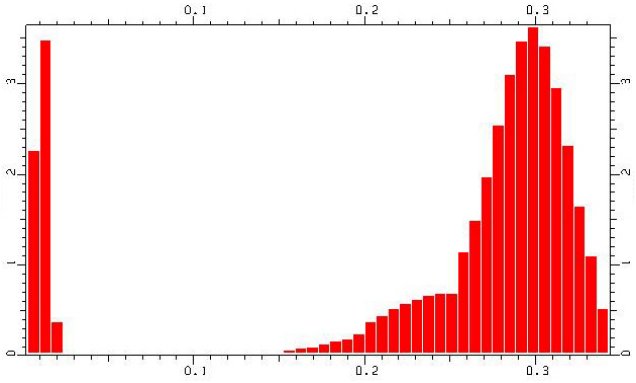

Figure 5.2: Porosity histogram of the 7100 Sand computed from the fine simulation grid (Counts are multiples of $10,000$)

tight, non-productive zones (Fig. 5.1). Chevron-Texaco up-scaled the fine grid to a model with $53 \times 18 \times 23$ gridblocks, which was used as starting point for this work.

Vasco et al. (2003) described automatic history matching work that incorporated both time-lapse seismic data and production data for this field. They up-scaled the 23-layer model to a 1-layer model and used a streamline simulator to do the history matching. The magnitude of their objective function decreased by about 1 order.

5.1 Reservoir simulation model analysis

Although it would be good to capture fluid flow features in fine scale if the 23-layer model could be used, stability issues resulting from running in history matching mode made the use of the 23-layer model impractical. Thus, it was decided to up-scale the 23-layer model to a 3-layer model.

Although up-scaling and down-scaling are important issues to be considered when multi-scale data, such as geological data, seismic data, and production data, are integrated into the model, to appropriately up-scale or down-scale a reservoir simulation model together with attached properties is a complex problem (Wen et al., 1998; Aanonsen et al., 2002, 2003; Gosselin et al., 2003; Zhang et al., 2003; Aanonsen, 2005). In this work, however, to up-scale the 23-layer model to a 3-layer model is one of many steps required by the automatic history matching process, and was not considered a key part of the research, therefore, the up-scaling was done by simply averaging the gridblocks vertically. The composition of fine-grid layers into the up-scaled 3 layers are chosen based on the relative permeability zones at different layers. There are 3 sets of relative permeability curves, as shown in Fig. 5.3. Curves for zone 1 and zone 2 are used for areas where oil, gas, and water co-exist. Zone 3 is specially allocated to the aquifer. In the vertical direction, the distribution of the relative permeability zones is well correlated. Those layers with similar relative permeability curves are averaged. Vertically, 3 zones are chosen with their start and end layer indices listed in Table 5.1.

	Start Layer Index	**End Layer Index**
Layer 1	1	6
Layer 2	7	18
Layer 3	19	23

Table 5.1: Start and end layer indices to up-scale the 23-layer simulation model to the 3-layer model

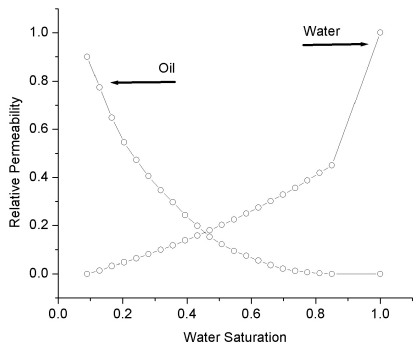

(a) Oil-water at zone 1

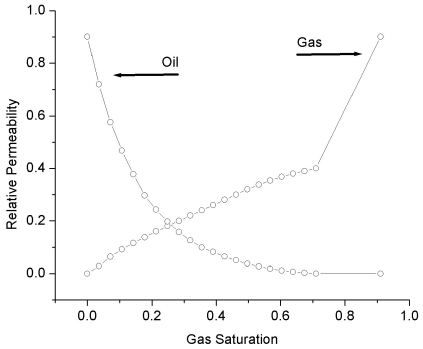

(b) Oil-gas at zone 1

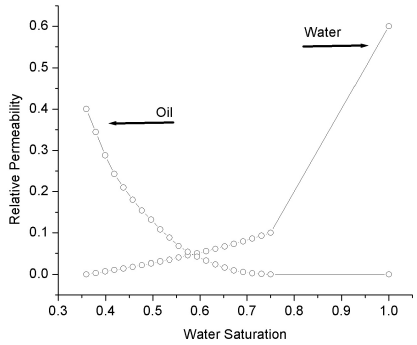

(c) Oil-water at zone 2

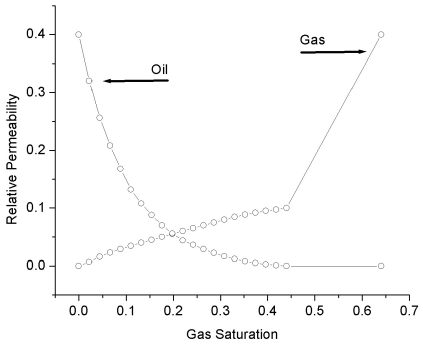

(d) Oil-gas at zone 2

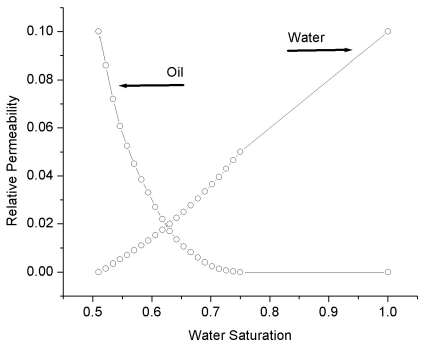

(e) Oil-water at zone 3

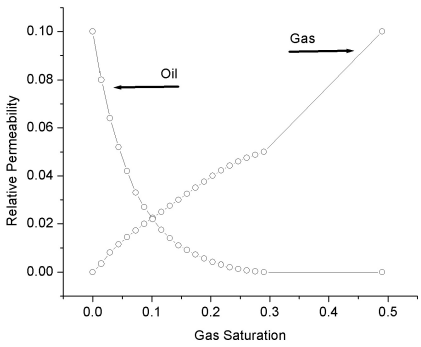

(f) Oil-gas at zone 3

Figure 5.3: Relative permeability curves of oil, gas, and water of the 3 different relative permeability zones

Before up-scaling, most of the gridblocks in the 23-layer model have sizes varying from 400 ft to 100 ft along X and Y directions, while the sizes along Z direction are more variable with some gridblocks less than 1 ft in thickness. In the up-scaled 3-layer model, the gridblock sizes along X and Y direction change little, but most gridblocks have their thickness over 10 ft along Z direction. The permeability and porosity at each gridblock are also up-scaled to the 3-layer model (Fig. 5.4). The up-

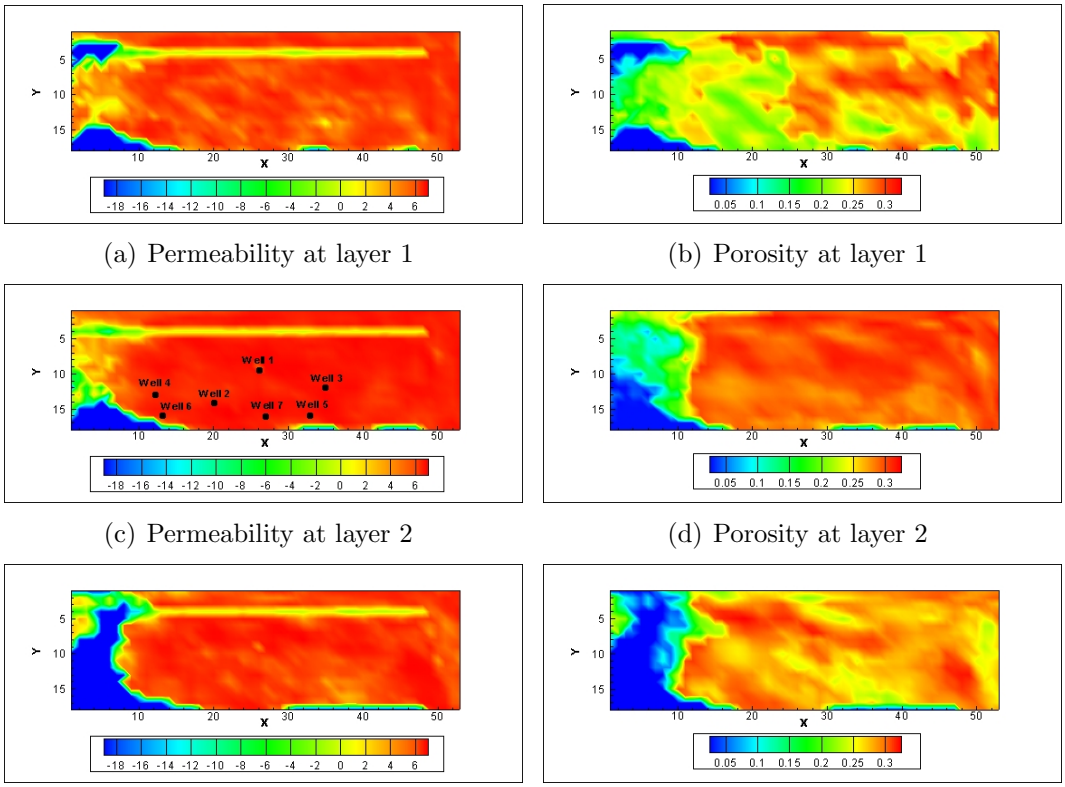

(a) Permeability at layer 1

(b) Porosity at layer 1

(c) Permeability at layer 2

(d) Porosity at layer 2

(e) Permeability at layer 3

(f) Porosity at layer 3

Figure 5.4: Initial log horizontal permeability and porosity fields at all 3 layers

scaled properties were used as the initial model for history matching. In Figs. 5.4(a), 5.4(c), and 5.4(e), there are linear features with low permeability. This feature was added manually by Chevron-Texaco to decrease water influx from the aquifer. The 7 black points in Fig. 5.4(c) denote the well locations, whose grid indices are listed in Table 5.2. Wells 1, 2, 3, and 4 were all drilled in early 1960's. The rest were infill wells drilled after the first seismic survey in 1987. The daily oil production rate histories

Well Index	I	J	K Top	K Bottom
Well 1	26	9	2	2
Well 2	20	14	1	2
Well 3	35	12	2	2
Well 4	12	13	1	2
Well 5	33	16	1	2
Well 6	13	16	1	3
Well 7	27	16	1	2

Table 5.2: Gridblock indices of the 7 wells

at the 7 wells are shown in Fig. 5.5 and Fig. 5.6. Of the four wells drilled in 1960's, wells 1 and 3 were shut in after 1975, and wells 2 and 4 produced until 1995.

In order to ensure that changes to the simulation model are plausible during the history matching stage, it is necessary to characterize the permeability and porosity correlation structure. This can be done from the starting model (Fig. 5.4). The permeability field taken from one layer was used for variogram analysis. A spherical model was selected to fit the anisotropic experimental variogram in the two principal directions, 30° and 120°, see Fig. 5.7. The unit of the distance axis in Fig. 5.7 is ft. The azimuth angle is used and the degree is counted clockwise from Y direction, whose degree is 0° (Deutsch and Journel, 1992). The fitting parameters are listed in Table 5.3. The same variogram model was used for porosity and for the

Direction	Range (ft)	Sill
120°	1,397	4.04
30°	1,124	4.30

Table 5.3: Variogram fitting parameters of the log horizontal permeability field

cross-correlation (Xu et al., 1992). The correlation coefficient between porosity and horizontal permeability was assumed to be 0.5 for history matching.

A map of the top of the reservoir in the 3-layer model is shown in Fig. 5.8. The black region denotes the small gas cap and the light blue region denotes the aquifer. The initial water oil contact is 7,001 ft and the initial gas oil contact is 6,755 ft.

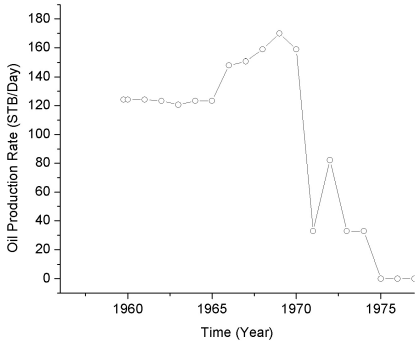

(a) Well 1

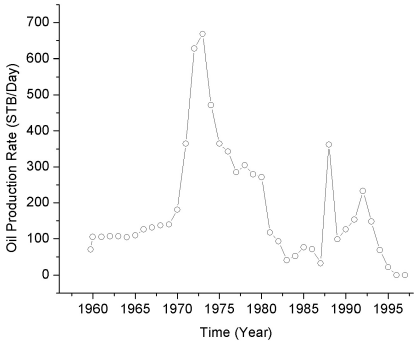

(b) Well 2

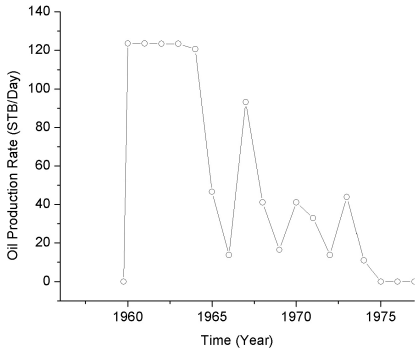

(c) Well 3

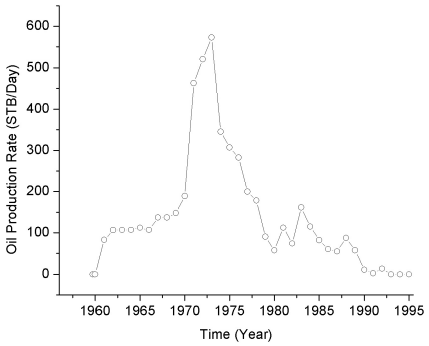

(d) Well 4

(e) Well 5

Figure 5.5: Daily oil production rate histories at wells 1 to 5

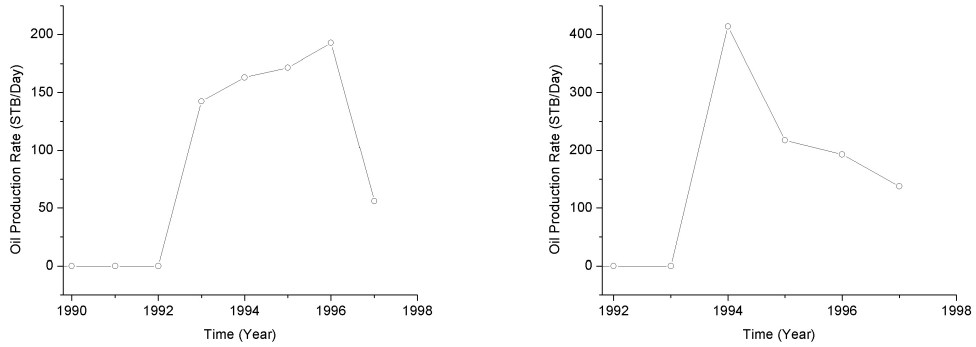

(a) Well 6 (b) Well 7

Figure 5.6: Daily oil production rate histories at wells 6 to 7

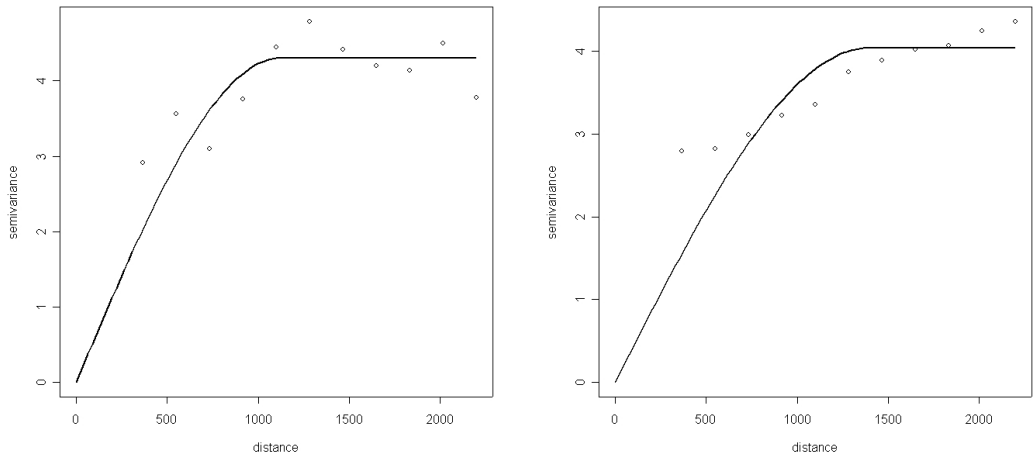

(a) 30° direction (b) 120° direction

Figure 5.7: Fitted and experimental variograms along two principal directions of the initial log horizontal permeability field at one layer

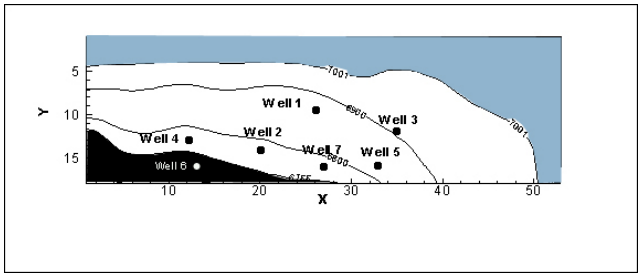

Figure 5.8: Top depth of the 3-layer model

5.2 Rock physics model analysis

A set of rock physics model parameters were provided by Chevron-Texaco, some of which were also used in Behrens et al. (2002) when they modelled the time-lapse seismic response. Based on those rock physics model parameters, the seismic impedance is computed using

$$Z = \sqrt{\rho \left(K + \frac{4}{3} G \right)}, \tag{5.1}$$

which requires the body density ρ, the bulk modulus K, and the shear modulus G. The body density ρ can be computed using

$$\rho = (\rho_o S_o + \rho_w S_w + \rho_g S_g)\phi + (1 - \phi)\rho_{\text{solid}}\,, \tag{5.2}$$

where the phase saturations are from the reservoir simulator and the grain density ρ_{solid} is equal to $2,750\ kg/m^3$.

The bulk modulus K is still computed using the Gassmann equations

$$K = K_{\text{grain}} \frac{K_{\text{frame}} + Q}{K_{\text{grain}} + Q}\,, \tag{5.3}$$

and

$$Q = \frac{K_{\text{fluid}} \left(K_{\text{grain}} - K_{\text{frame}} \right)}{\phi \left(K_{\text{grain}} - K_{\text{fluid}} \right)}\,. \tag{5.4}$$

They require computing the bulk moduli of dry frame, grain, and pore fluid. The bulk modulus of pore fluid is computed using

$$\frac{1}{K_{\text{fluid}}} = \frac{1.0 - S_o - S_g}{K_w} + \frac{S_g}{K_g} + \frac{S_o}{K_o}\,, \tag{5.5}$$

where the phase saturations are from the simulator. The bulk moduli of oil and water are constants, 1.363 GPa and 3.434 GPa respectively (Behrens et al., 2002). The bulk modulus of gas can be computed using two different ways. One is to use correlation equations (Batzle and Wang, 1992), which was the approach chosen by Behrens et al. (2002) in their work. The other approach, which was used in this work, calculates

the bulk modulus of gas using the isothermal compressibility of gas, which is defined as

$$c_g = -\frac{1}{B_g}\frac{dB_g}{dP}\,, \tag{5.6}$$

where B_g is formation volume factor. The isothermal compressibility of gas is just the reciprocal of the bulk modulus of gas and can be computed according to the fluid property tables input into the reservoir simulator. The bulk modulus of grain, K_{grain}, is assumed to be 38 GPa in all calculations. The bulk modulus of the dry frame is computed using the following relation,

$$K_{\text{frame}} = a_0 + a_1 P_{\text{diff}} + a_2\sqrt{P_{\text{diff}}} + \left(b_0 + b_1 P_{\text{diff}} + b_2\sqrt{P_{\text{diff}}}\right)\phi\,, \tag{5.7}$$

where ϕ is porosity, a through b are empirically determined coefficients, and P_{diff} is the pressure difference between overburden pressure and pore pressure. The unit of pressure is psia and the unit of K_{frame} is GPa. 1 psia/ft was used to compute the overburden pressure.

The shear modulus of dry frame is computed using Eq. 5.8,

$$G = c_0 + c_1 P_{\text{diff}} + c_2\sqrt{P_{\text{diff}}} + \left(d_0 + d_1 P_{\text{diff}} + d_2\sqrt{P_{\text{diff}}}\right)\phi\,, \tag{5.8}$$

where c through d are empirically determined coefficients. Again, the unit of pressure is psia and the unit of shear modulus is GPa. Since the influence of fluid saturation on shear modulus is small, the shear modulus of dry frame is also used as shear modulus of fluid saturated rock in Eq. 5.1.

Changes of shear modulus G and bulk modulus of dry frame K_{frame} with respect to changes in pressure difference and porosity for some typical values are shown in Fig. 5.9.

Since the equations used to compute K_{frame} and G are different from those shown in Chapter 3, the derivatives of seismic impedance with respect to pressure, phase saturations, and porosity are slightly different. The new derivatives can be easily achieved by applying the chain rule to Eq. 5.7 and Eq. 5.8.

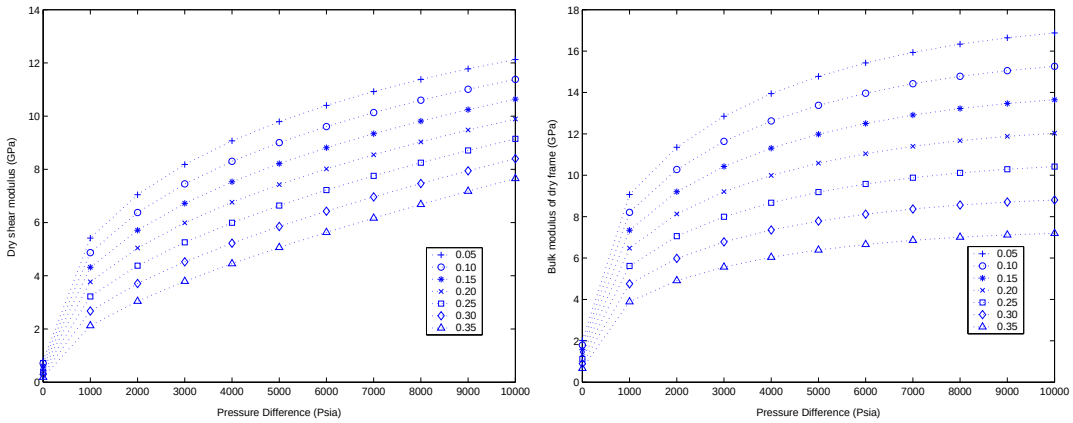

(a) Shear modulus of dry frame

(b) Bulk modulus of dry frame

Figure 5.9: Changes in shear modulus and bulk modulus of dry frame with respect to changes in porosity and pressure difference

5.3 Observed seismic impedance change data

Due to the strong aquifer support, there are no injection wells in this reservoir. The major displacement mechanism comes from water influx. Hence, the seismic impedance change is mainly a result of the replacement of oil with water, which causes an increase in seismic impedance because both the bulk modulus and the density of water are larger than those of oil. Although there is a small amount of gas, the effect is expected to be limited to a very small area so that negative impedance changes should be relatively uncommon. The impedance change data were generated directly from the seismic reflection coefficient at the interface between the 7100 Sand and the upper shale. The seismic reflection coefficient at one interface between two layers is defined as,

$$R = \frac{Z_2 - Z_1}{Z_2 + Z_1}\,, \tag{5.9}$$

where Z_2 is seismic impedance of the layer below the interface and Z_1 is seismic impedance of the layer above the interface. Eq. 5.9 assumes that wave propagates perpendicular to the interface. For arbitrary angle of incidence, the reflection coefficient equation becomes much more complicated (Yilmaz and Doherty, 1987).

The reflection coefficients at the sand-shale interface in 1987 and 1998 are shown in Fig. 5.10. Based on the coefficients, the following values can be computed,

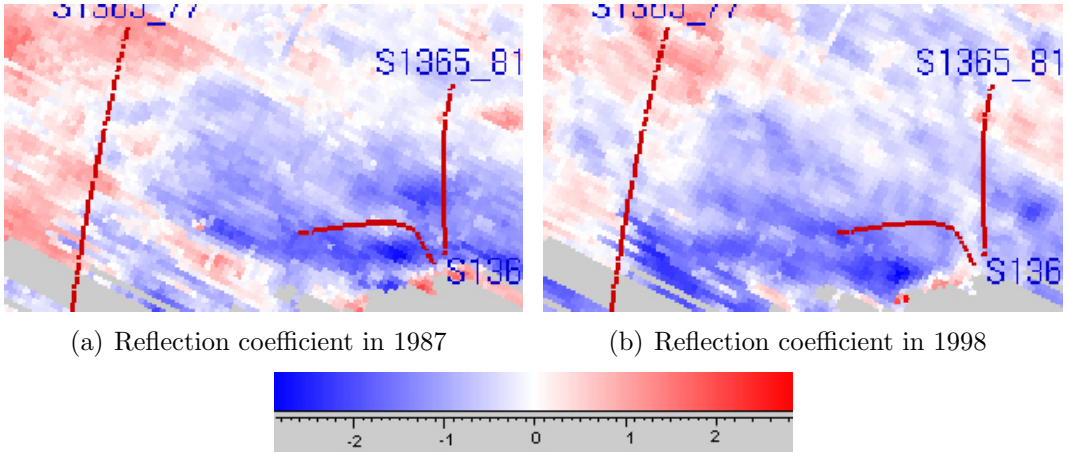

(a) Reflection coefficient in 1987 (b) Reflection coefficient in 1998

Figure 5.10: Reflection coefficients at the interface between the 7100 Sand and the upper shale in 1987 and 1998

$$R^{+} = \frac{R_1 + R_2}{2} \times \alpha \,, \tag{5.10}$$

and

$$\triangle R = (R_2 - R_1) \times \alpha \,, \tag{5.11}$$

where R_1 is the reflection coefficient in 1987, R_2 is the reflection coefficient in 1998, and α is a scalar used by Chevron-Texaco to balance the reflection coefficient difference. Using R^{+} and $\triangle R$, the impedance change can be computed using Eq. 5.12,

$$\triangle Z = \frac{2\triangle R}{1 - (R^{+})^2} \times Z_{\text{shale}} \,, \tag{5.12}$$

where Z_{shale} is the seismic impedance of the upper shale. Fig. 5.11 shows $\triangle Z / Z_{\text{shale}}$ at the interface between the 7100 Sand and the upper shale. Despite the obvious acquisition artifacts, the impedance changes are predominantly positive. The region of negative impedance change at the lower right corner is consistent with the Fig. 13 in Behrens et al. (2002).

To compute the impedance change using Eq. 5.12 requires the shale impedance, Z_{shale}. Behrens et al. (2002) gave some typical values of rock properties of the

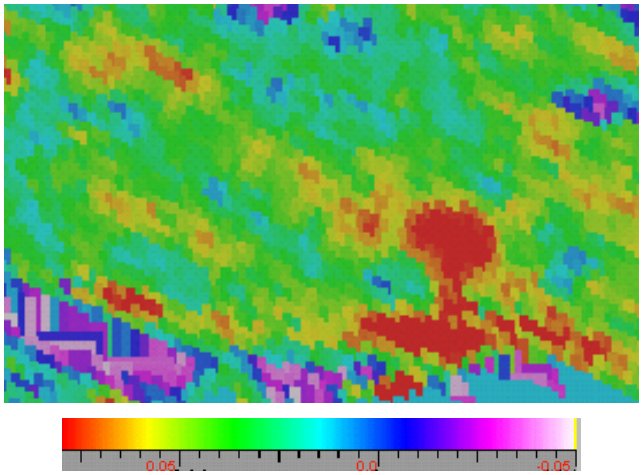

Figure 5.11: $\triangle Z/Z_{\text{shale}}$ at the interface between the 7100 Sand and the upper shale

shale above the 7100 Sand. Substituting these values into Eq. 5.1, Z_{shale} is equal to $7.039 \times 10^6\ kg/(m^3 \cdot s)$. Using this value in Eq. 5.12, the magnitude of the computed impedance change is inconsistent with that of predicted seismic impedance change from the reservoir simulator. There are two ways to solve this problem. One is to modify the rock physics model or model parameters. The other approach, which is used here, is to tune the shale impedance, Z_{shale}. It is assumed that the observation noise in the impedance change data can be approximated by a normal distribution with mean equal to 0. By subtracting the noise from the observed impedance change data, the "true" signal can be uncovered. To adjust Z_{shale} is to make the mean of the "true" signal equal to the mean of the computed impedance change from the simulator. After adjusting Z_{shale}, the histogram of the observed impedance change is shown in Fig. 5.12. The unit of the X-axis is $10^5\ kg/(m^3 \cdot s)$ and the Y-axis is count.

The impedance change computed from reflection coefficient change at the top of the reservoir is a 2-D data sheet that is influenced by fluid saturation changes from the whole 7100 Sand. To use the 2-D impedance change observation, it is necessary to account for the sensitivity of reflection coefficient to the predicted impedance change in gridblocks within the reservoir. We assume a linear weighting such that the 2-D

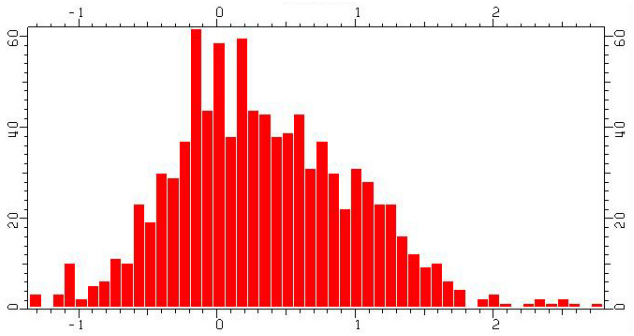

Figure 5.12: Histogram of the observed seismic impedance change computed using the reflection coefficient change and the shale impedance

data is given by

$$g(m) = \triangle Z = \frac{1}{N_z} \begin{bmatrix} \sum_{k=1}^{N_z} \beta_k \triangle Z_{1,1,k} \\ \sum_{k=1}^{N_z} \beta_k \triangle Z_{2,1,k} \\ \vdots \\ \sum_{k=1}^{N_z} \beta_k \triangle Z_{N_x,N_y,k} \end{bmatrix}, \tag{5.13}$$

where N_z is the number of gridblocks in the Z direction. If $g(m)$ in Eq. 5.13 is used as a source term in the adjoint equations to compute sensitivity with respect to permeability and porosity, the derivatives at each layer will be computed accordingly. β_k in Eq. 5.13 is the weighting assigned to each layer, which determines how much each of the 3 layers contributes. To choose an optimal β for each layer probably requires forward modelling of the seismic wave field. In this work, β is selected through history matching experiments, considering 3 aspects: 1) objective function reduction; 2) top layer should contribute more because it is closer to the interface; 3) the magnitude of averaged predicted impedance change should be consistent with that of the observed impedance change. The final ratio for vertical average is, $\beta_1 = 0.9$, $\beta_2 = 0.1$, and $\beta_3 = 0.0$.

In contrast to the synthetic case study, where the impedance change observations are computed at each gridblock, the observed impedance change data in this real case study have correlated noise. To appropriately weight the data mismatch term in the objective function (Eq. 2.7), a non-diagonal data noise covariance matrix C_D must be

set up (Aanonsen et al., 2002, 2003). Although it might be possible to estimate the noise structure through careful analysis of the seismic data processing work flow, such calculation is impractical due to its high complexity. Therefore, the noise covariance structure is evaluated from the impedance change observation directly.

At the aquifer of the 7100 Sand, the observed seismic impedance change is presumably due to non-repeatable noise because the changes in pressure and saturation are negligible. Variogram analysis is applied to the seismic impedance change at the aquifer to capture the noise correlation structure. Fig. 5.13 shows the fitted and experimental variograms along two principal directions. The theoretical variogram

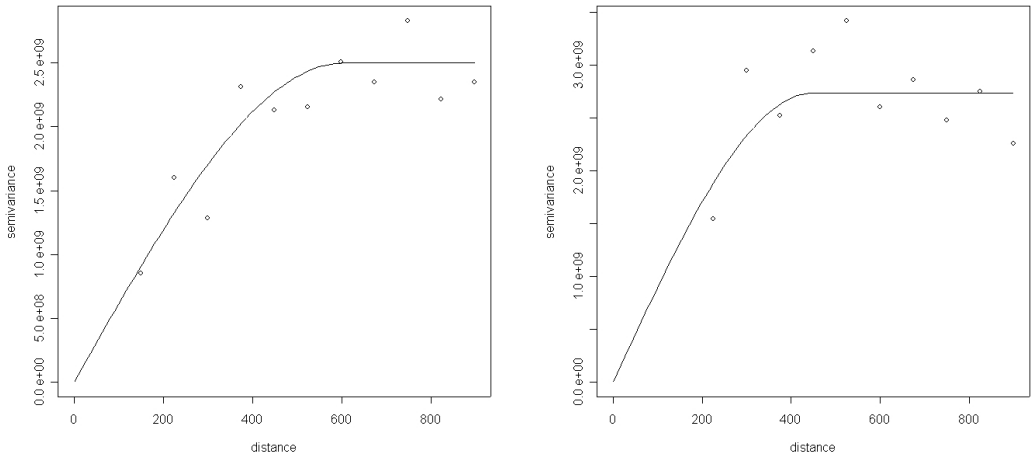

(a) 75° direction (b) 165° direction

Figure 5.13: Fitted and experimental variograms along two principal directions of the seismic impedance change data noise

model used for fitting is a spherical model and its fitting parameters are listed in Table 5.4. The arithmetic average of the two sills shown in Table 5.4 was used to

Direction	Range (ft)	Sill
75°	605	2.5×10^9
165°	450	2.7×10^9

Table 5.4: Variogram fitting parameters of the seismic impedance change noise

construct the covariance matrix C_D in history matching stage.

5.4 Automatic history matching results

In our synthetic case studies, the base-line survey was always assumed to be shot before production started. This gave initial condition with no uncertainty in saturation or pressure and provided the maximum seismic impedance change. In this real case study, however, the first seismic survey was shot in 1987, which is 27 years after production began. It turned out to be quite difficult to simultaneously match both the seismic impedance change data and the production data using the initial model provided by Chevron-Texaco due to uncertainties in distributions of pressure and phase saturations when the first survey was conducted. So the first step in history matching phase is to match the production data only. The result can then be used as an initial model to match the seismic data.

5.4.1 Matching production data only

The 7100 Sand has very strong aquifer support so the average reservoir pressure did not change much during production (Behrens et al., 2002). The primary seismic changes are due to the advancement of water into the field, so attention has been focused on matching the water breakthrough time and the water cut afterwards at all 7 wells. Although GOR data were also used as observations, they were given relatively low weighting in the objective function. Each of the 7 wells has different start and end dates of production, so the observed WOR and GOR data are not uniformly distributed (see Table 5.5 and Table 5.6). In Tables 5.5 and 5.6, "–" means that no datum is available. The total number of WOR and GOR data used for history matching is 51. Note that the WOR and GOR data were calculated using the oil, gas, and water production rates at the 7 wells. Because the rates were given as yearly averaged values, the minimum interval between two WOR or GOR data is approximately 365 days.

Fig. 5.14 shows the objective function reduction for matching the WOR data and

Time (Day)	**Well** 1	**Well** 2	**Well** 3	**Well** 4	**Well** 5	**Well** 6	**Well** 7
187	–	–	0.333	–	–	–	–
1,552	–	–	0.636	–	–	–	–
1,917	–	–	4.353	–	–	–	–
3,012	10^{-6}	–	5.733	–	–	–	–
3,377	10^{-6}	–	9.833	–	–	–	–
3,742	0.034	–	–	–	–	–	–
4,107	0.167	–	–	–	–	–	–
4,472	1.800	–	–	–	–	–	–
4,837	3.083	0.090	–	0.321	–	–	–
5,202	–	0.965	–	0.881	–	–	–
6,297	–	–	–	1.630	–	–	–
6,662	–	–	–	2.692	–	–	–
7,027	–	1.657	–	4.848	–	–	–
7,392	–	3.697	–	8.333	–	–	–
7,757	–	8.209	–	–	–	–	–
8,122	–	9.471	–	–	–	–	–
1,0677	–	–	–	9.333	–	–	–
11,412	–	–	–	–	0.049	–	–
11,772	–	–	–	–	2.203	–	–
12,142	–	12.833	–	–	7.663	8.212	–
12,507	–	20.840	–	–	12.544	10.027	0.686
12,867	–	28.375	–	–	15.214	12.291	6.257
13,232	–	–	–	–	15.214	12.291	8.675
13,597	–	–	–	–	19.089	15.652	14.736

Table 5.5: Observed WOR data at the 7 wells

Time (Day)	**Well** 1	**Well** 2	**Well** 3	**Well** 4	**Well** 5	**Well** 6	**Well** 7
2,647	–	–	264.7	–	–	–	–
3,012	–	–	533.3	–	–	–	–
4,107	500.0	–	–	–	–	–	–
4,837	1000.0	–	–	–	–	–	–
10,312	–	–	–	156.3	–	–	–
10,677	–	–	–	381.0	–	–	–
12,507	–	–	–	–	–	–	122.7
12,867	–	–	–	–	–	–	516.0

Table 5.6: Observed GOR (SCF/STB) data at the 7 wells

GOR data at all 7 wells. We can see that the objective function reduces more than

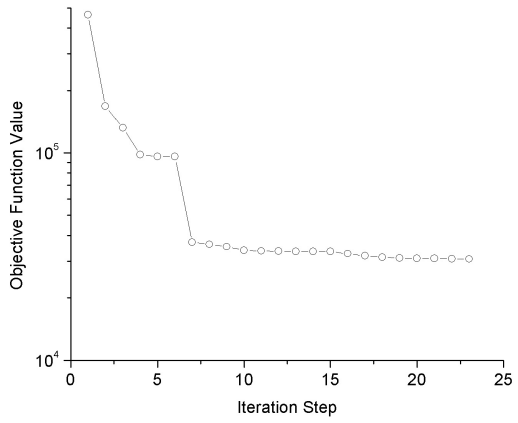

Figure 5.14: Objective function reduction when matching production data only

1 order of magnitude. After production data matching, most of the 7 wells have improvements in their water cut changes, in terms of closeness to the observed water cut curves, see Fig. 5.15 and Fig. 5.16. The production history matched permeability and porosity fields are shown in Fig. 5.17. Compared with the initial model (Fig. 5.4), the field scale features do not change greatly after matching the production data, but some regions near the wells have substantial changes in rock properties, see Fig. 5.18. The 7 wells are denoted using black dots in Fig. 5.18(c). It can be seen that in Fig. 5.18(c), the area to upper right of the well 1 has permeability reduction in the middle layer. From Fig. 5.8, we know that a permeability barrier is located between the well 1 and the aquifer. Because the initial model has too fast water breakthrough in the well 1, the permeability reduction in that region was required to delay the water breakthrough time, see Fig. 5.15(a). The porosity values at the same area show a small decrease, which mainly comes from the positive correlation coefficient between the permeability and porosity.

Although 5 wells are completed in the top layer (Table 5.1), only 2 of them, i.e., wells 5 and 7, have obvious improvements in their water cut curves through matching

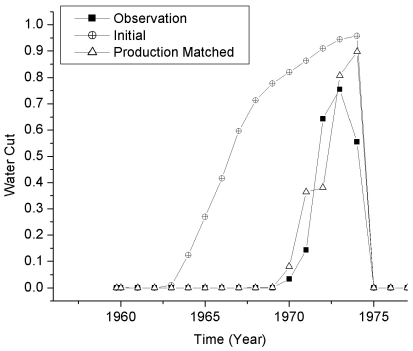

(a) Well 1

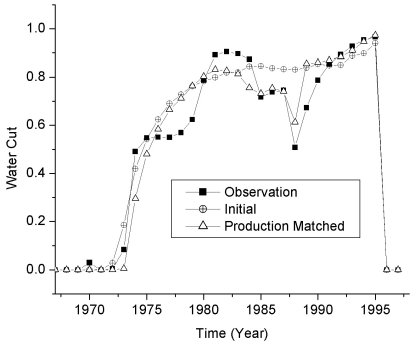

(b) Well 2

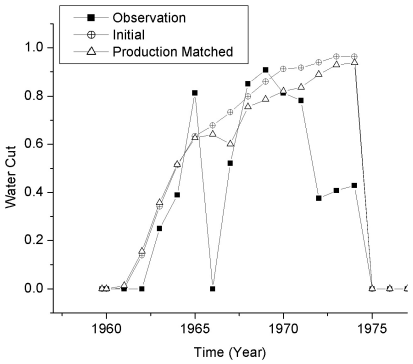

(c) Well 3

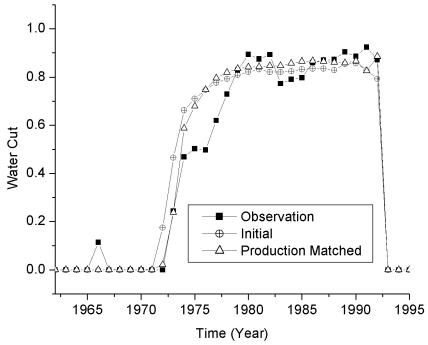

(d) Well 4

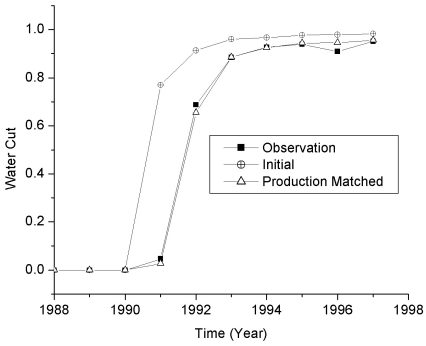

(e) Well 5

Figure 5.15: Water cut comparison among the true, initial, and production data matched models at wells 1 to 5

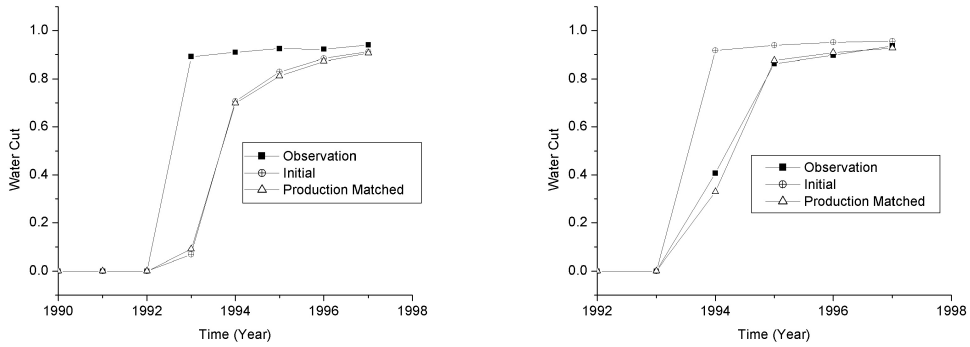

(a) Well 6 (b) Well 7

Figure 5.16: Water cut comparison among the true, initial, and production data matched models at wells 6 to 7

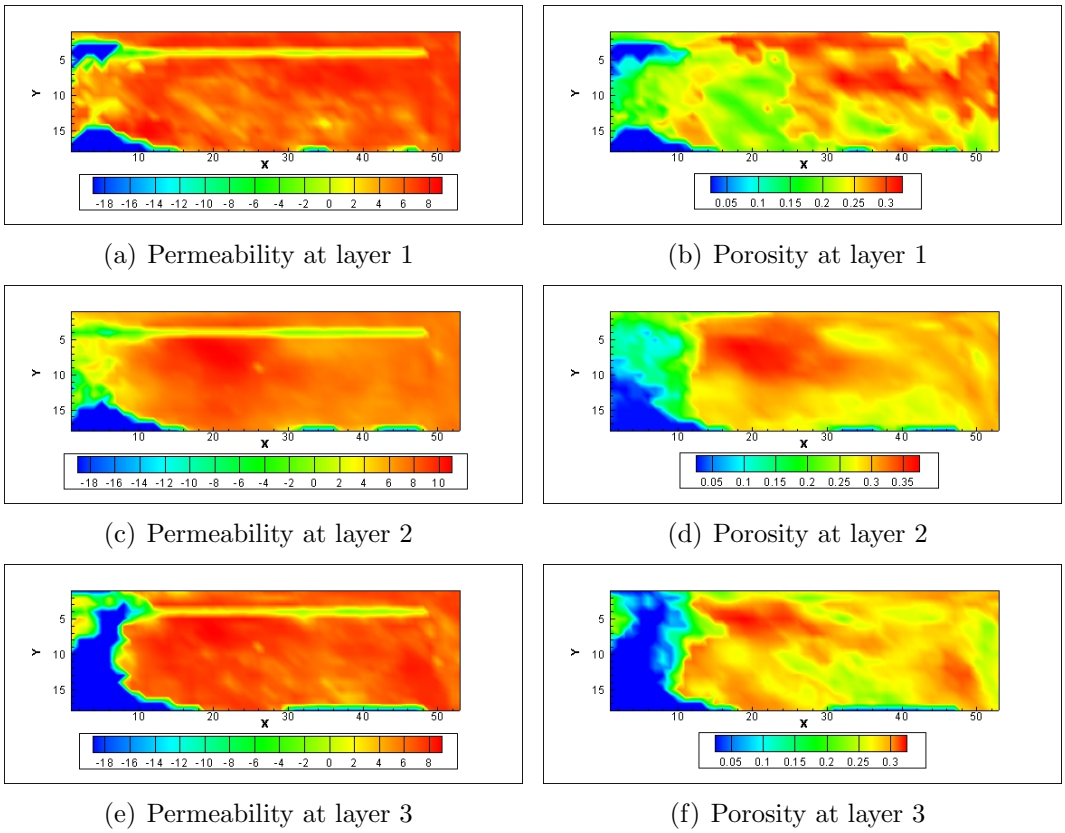

(a) Permeability at layer 1 (b) Porosity at layer 1

(c) Permeability at layer 2 (d) Porosity at layer 2

(e) Permeability at layer 3 (f) Porosity at layer 3

Figure 5.17: Log horizontal permeability and porosity fields at all 3 layers after matching the production data only

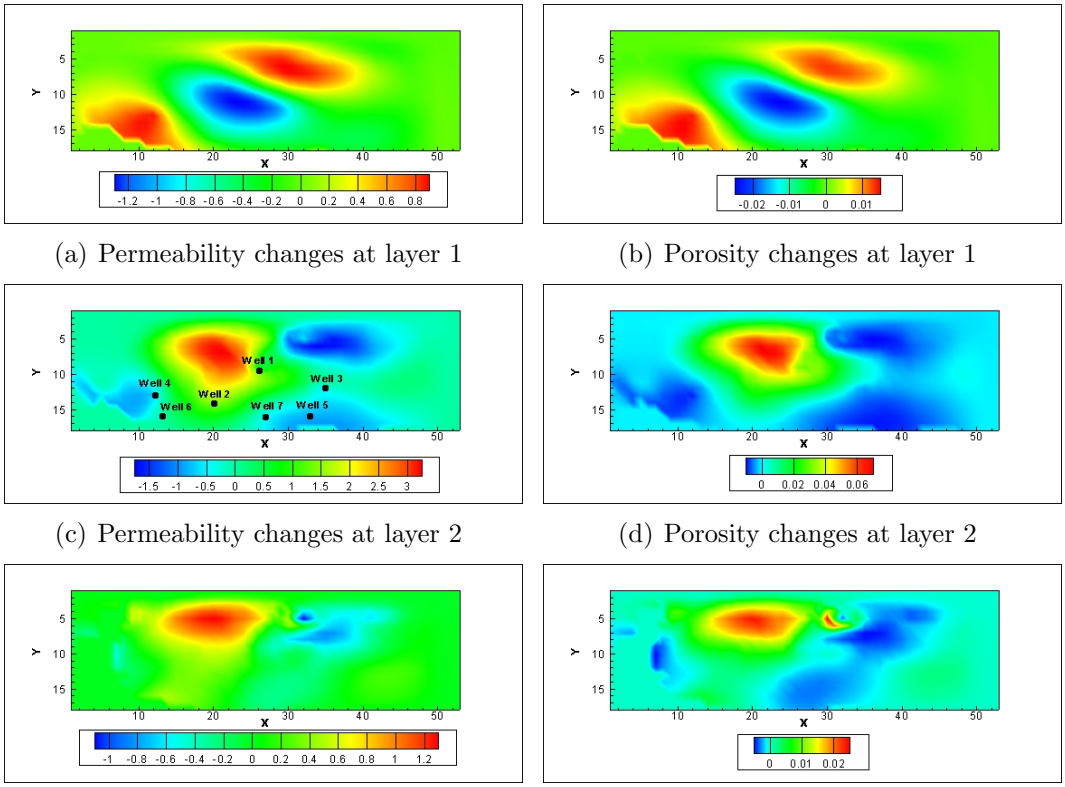

(a) Permeability changes at layer 1

(b) Porosity changes at layer 1

(c) Permeability changes at layer 2

(d) Porosity changes at layer 2

(e) Permeability changes at layer 3

(f) Porosity changes at layer 3

Figure 5.18: Log horizontal permeability and porosity changes at all 3 layers after matching the production data only

the production data, see Fig. 5.15(e) and Fig. 5.16(b). The initial model gives correct water breakthrough time but produces too much water. The production data matched model decreases the water cut, which mainly comes from the permeability reductions in the gridblocks around the two wells.

The pattern of change in the permeability field at layer 1 (Fig. 5.18(a)) is very similar as that of the porosity field at the same layer (Fig. 5.18(b)), which results from the positive correlations between the permeability and porosity. At layer 3, the magnitude of changes is much smaller because only well 6 has completion in that layer.

5.4.2 Matching seismic impedance change data

There are $53 \times 18 = 954$ data points converted from the reflection coefficient changes at the interface between the 7100 Sand and the upper shale, but the changes at the aquifer were not used because they are from non-repeatable noise. In addition, there are some inactive gridblocks due to changes in facies (Behrens et al., 2002). The seismic impedance change data at those gridblocks were not used as observations either.

The estimated property fields after matching the production data are used as the initial model for matching the seismic impedance change data. Fig. 5.19 shows water saturation and gas saturation changes between the two seismic surveys using the production data matched model as input for the simulator. Obviously, there are major changes in water saturation. In contrast, gas saturation changes only at a small number of gridblocks in layer 1. As discussed in Chapter 3, the magnitude of K_g is usually two orders smaller than the magnitudes of K_o and K_w. Therefore, even small changes in gas saturation can result in large changes in seismic impedance. Table 5.7 shows I and J indices of those outliers as well as the computed seismic impedance change at those locations. The unit of impedance change in Table 5.7 is $kg/(m^2 \cdot s)$.

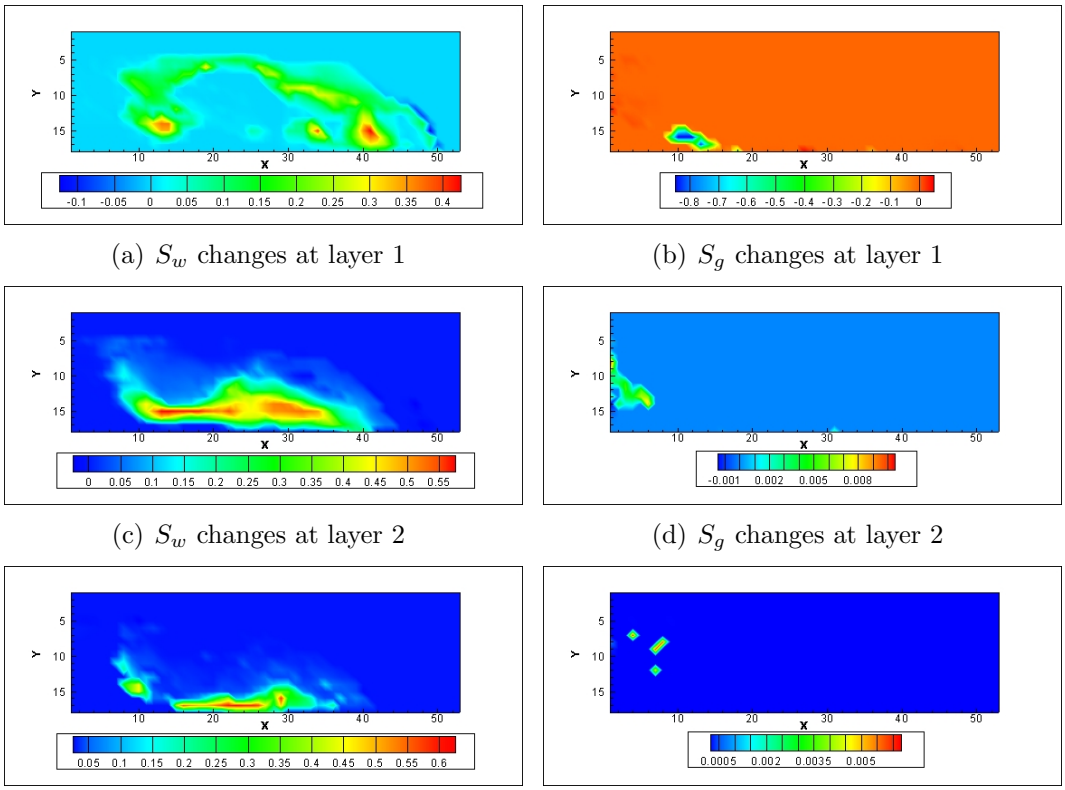

(a) S_w changes at layer 1

(b) S_g changes at layer 1

(c) S_w changes at layer 2

(d) S_g changes at layer 2

(e) S_w changes at layer 3

(f) S_g changes at layer 3

Figure 5.19: Water saturation and gas saturation changes between the seismic surveys using the production data matched model as input for the reservoir simulator

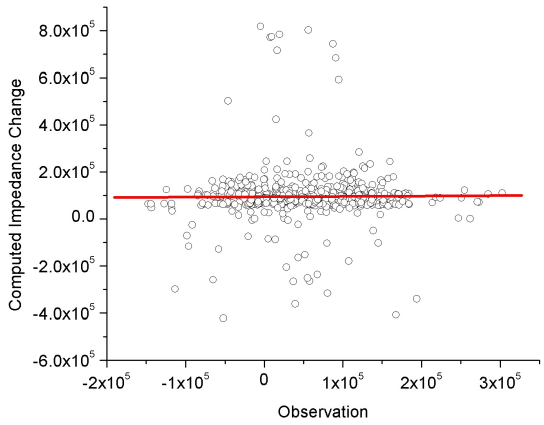

Figure 5.20: Cross plot of the initial computed seismic impedance change and the observation with outliers from gas saturation changes

I	J	Computed Impedance Change	Observation
4	5	-2.37×10^5	6.75×10^4
1	7	-3.16×10^5	8.06×10^4
1	11	-2.98×10^5	-10.13×10^4
2	11	-4.22×10^5	-5.18×10^4
5	11	-2.59×10^5	-6.53×10^4
10	15	7.15×10^5	1.66×10^4
11	15	7.71×10^5	0.78×10^4
12	15	4.23×10^5	1.51×10^4
9	16	8.17×10^5	-0.48×10^4
10	16	7.73×10^5	0.95×10^4
11	16	7.83×10^5	1.95×10^4
13	16	7.43×10^5	8.75×10^4
14	17	6.83×10^5	9.11×10^4
36	18	5.02×10^5	-4.61×10^4

Table 5.7: Outliers' locations and their initial computed seismic impedance change values

The positive values are due to gas saturation decrease.

Unfortunately, like any other least-square methods, the objective function derived from the Bayesian framework (Eq. 2.7) is strongly affected by outliers during the minimization process, i.e., the model parameters for gridblocks with data outliers tend to be over-adjusted to decrease data mismatches. Considering that water influx is the main driving mechanism in the Bay Marchand field, the seismic impedance change observations at the gridblocks where gas saturation has changed significantly between the two seismic surveys were not used in the objective function. Thus, the number of observed impedance change data used for history matching is 485. Its distribution is shown in Fig. 5.21. In Fig. 5.21(a), the impedance change values are shown, with non-used gridblocks filled with 0s. Since there are also negative impedance changes, the gridblocks with 0 values are not obvious. So Fig. 5.21(b) is used to show the locations, where only impedance changes at the red color filled blocks are used as observations.

The objective function reduction when matching seismic impedance change data

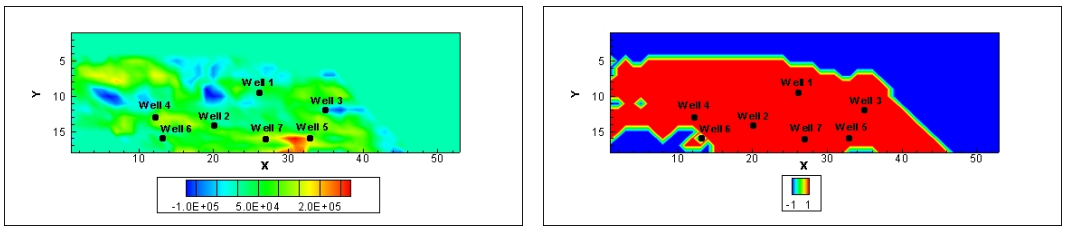

(a) Seismic impedance observation (b) Location distribution

Figure 5.21: Observed seismic impedance change data and their location distributions

is shown in Fig. 5.22. Due to relatively low data quality, the objective function

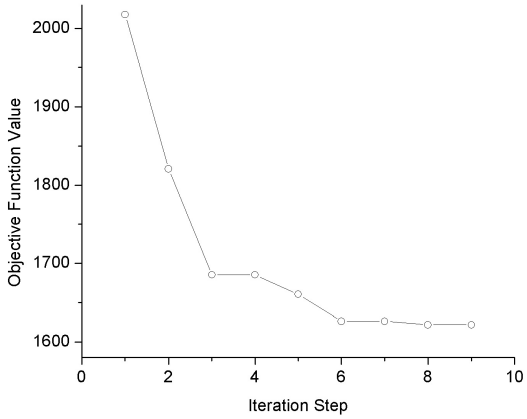

Figure 5.22: Objective function reduction when matching seismic impedance change data

does not gain 1 magnitude reduction as the production data matching does. The water cut curves at all 7 wells after matching the seismic impedance change data are shown in Fig. 5.23 and Fig. 5.24. To have clearer comparison, the water cut curves from the production data matched models are plotted as well. Because the water breakthrough times at all wells have been matched fairly well by integrating only production data, the seismic data does not obviously improve the breakthrough time matching. But water cut matching after breakthrough at some wells benefit from the seismic impedance change data, for example, wells 2, 4, and 6.

The computed seismic impedance change data at the last minimization step have

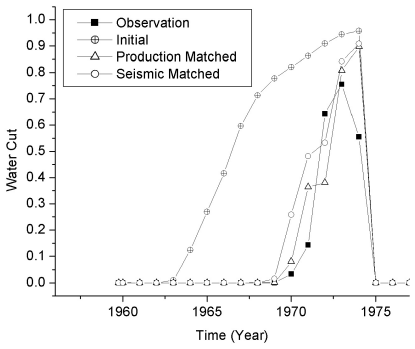

(a) Well 1

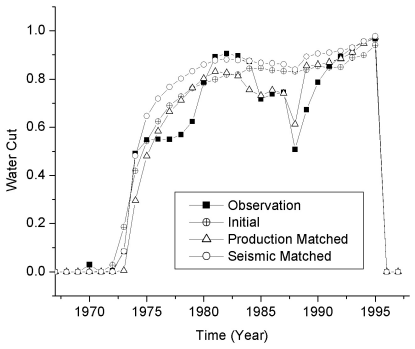

(b) Well 2

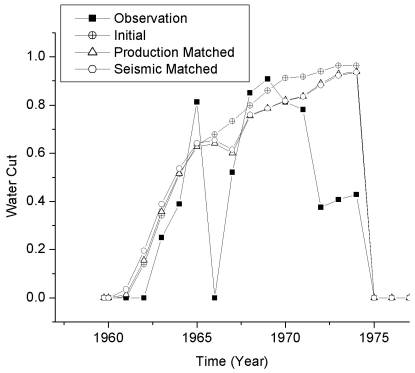

(c) Well 3

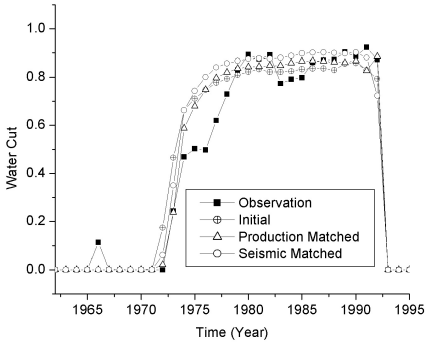

(d) Well 4

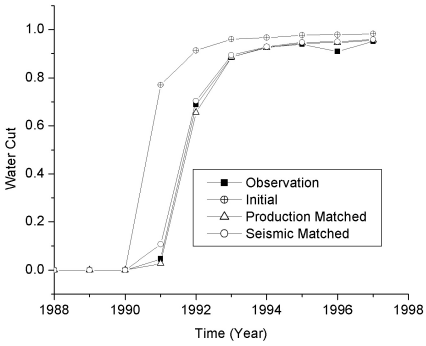

(e) Well 5

Figure 5.23: Water cut comparison among the true, initial, production data matched, and seismic data matched models at wells 1 to 5

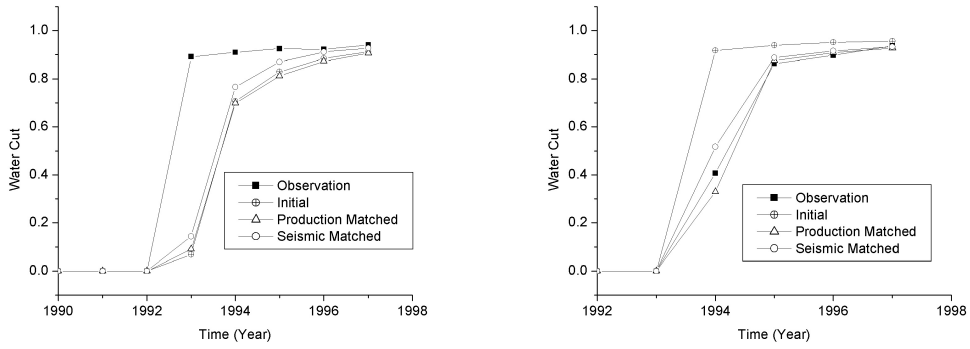

(a) Well 6 (b) Well 7

Figure 5.24: Water cut comparison among the true, initial, production data matched, and seismic data matched models at wells 6 to 7

better correlation with the observed impedance change data than that at the first step does, see Fig. 5.25. The red lines in Fig. 5.25(a) and Fig. 5.25(b) are regression

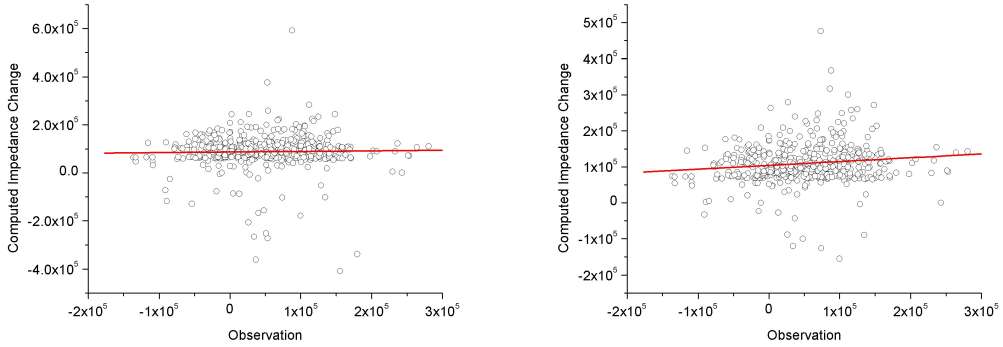

(a) First step (b) Last step

Figure 5.25: Cross plots of the observed and computed impedance change data at the first and last minimization steps

lines with form $Y = A + B * X$, where Y denotes the computed data and X denotes the observation. Some data points that have large mismatch from the observations at the first step (Fig. 5.25(a)) reduce their mismatch during history matching, which contributes to the correlation improvements at the last step (Fig. 5.25(b)). However, many points with small impedance change do not move much, and some points that are over-adjusted during minimization become outliers. Therefore, the correlation

coefficient at the last step is still very low, see Table 5.8.

	A	B	R
First step	0.87×10^5	0.024	0.0198
Last step	1.04×10^5	0.11	0.10

Table 5.8: Regression parameters of the computed and observed impedance change data at the first and last minimization steps

The log horizontal permeability and porosity fields after matching the seismic impedance change data are shown in Fig. 5.26. Compared with the initial model

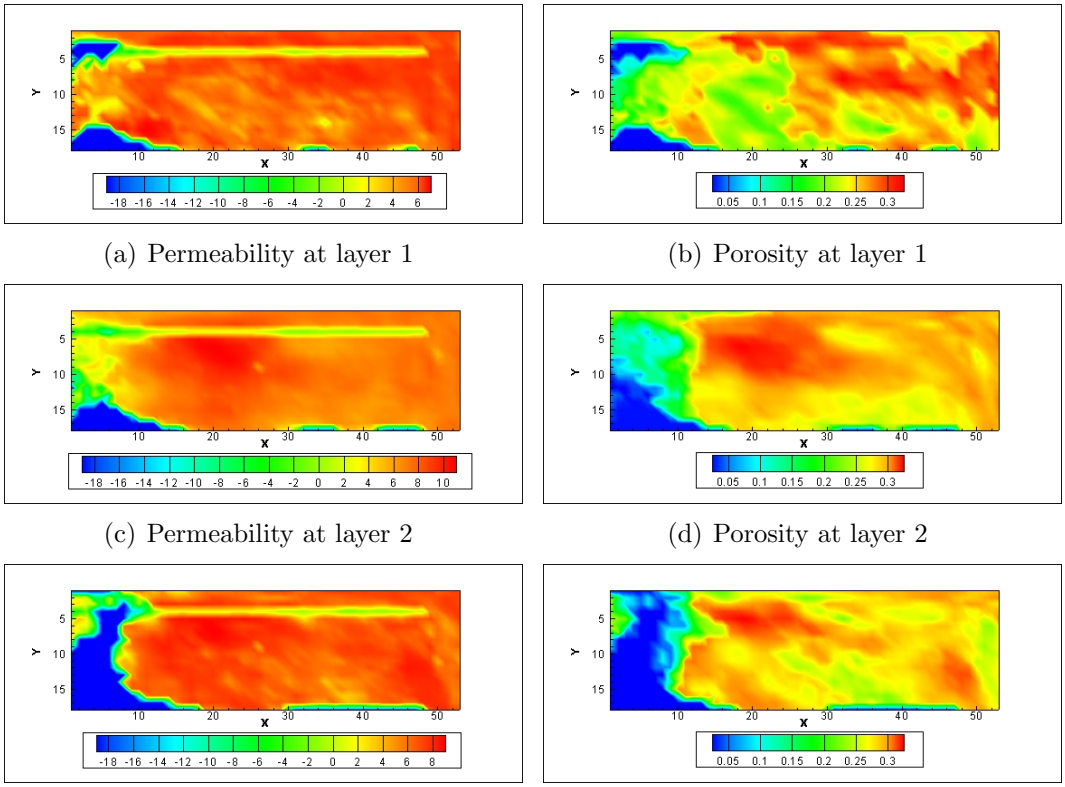

(a) Permeability at layer 1

(b) Porosity at layer 1

(c) Permeability at layer 2

(d) Porosity at layer 2

(e) Permeability at layer 3

(f) Porosity at layer 3

Figure 5.26: Log horizontal permeability and porosity fields at all 3 layers after matching the seismic impedance data

(Fig. 5.4) and the production data matched model (Fig. 5.17), the seismic impedance change data matched model does not have obvious differences in field structures. By subtracting production data matched model from the model after matching the

seismic impedance change data, we can obtain the model changes, which are shown in Fig. 5.27. The black dots in Fig. 5.27(c) denote the 7 wells.

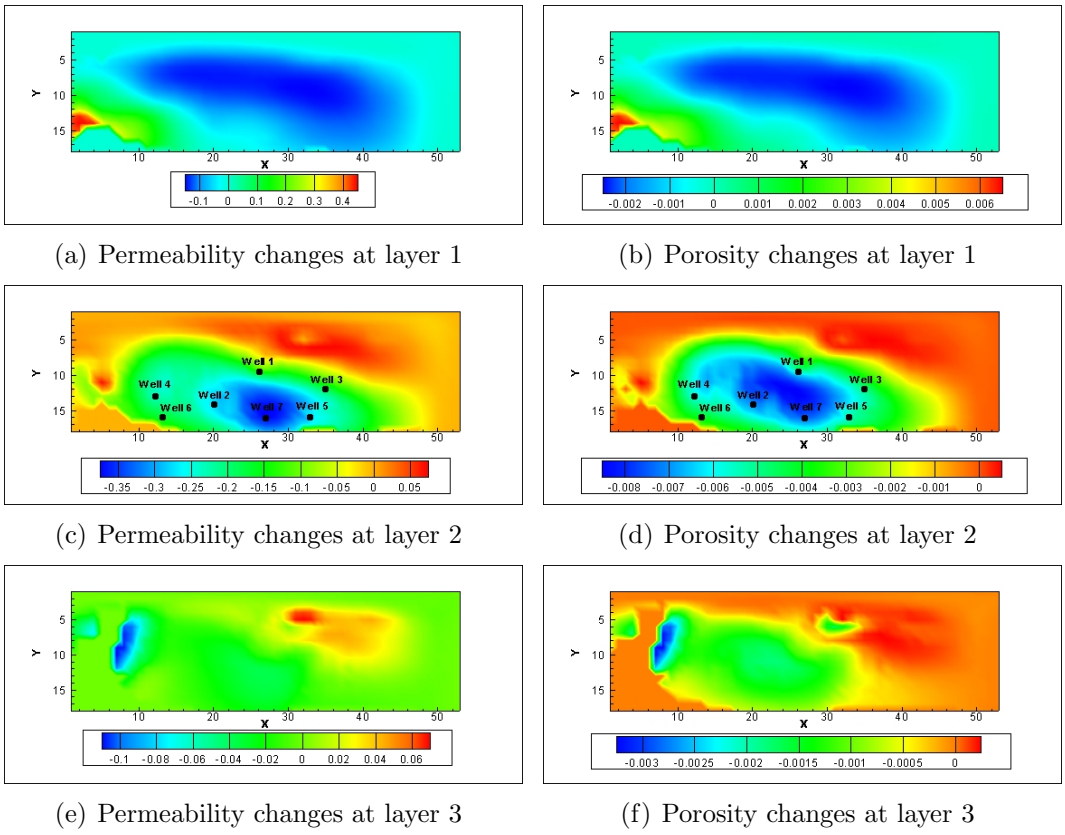

(a) Permeability changes at layer 1

(b) Porosity changes at layer 1

(c) Permeability changes at layer 2

(d) Porosity changes at layer 2

(e) Permeability changes at layer 3

(f) Porosity changes at layer 3

Figure 5.27: Log horizontal permeability and porosity changes at all 3 layers after matching the seismic impedance change data

Some observations can be made as following,

- Both permeability and porosity have their major changes at layers 1 and 2.
- At layer 1 and layer 2, the permeability change is similar as the porosity change due to the correlation between the permeability and the porosity.
- At layer 2, the most obvious porosity changes are around wells 2, 5, and 7. From Figs. 5.23(b), 5.23(e), and 5.24(b), it can be seen that the observed water cuts at those 3 wells are higher than the computed water cuts after matching the production data. Thus, the observed impedance changes are also larger than

the computed impedance changes using the production data matched model. After matching the impedance change data, the porosity values are decreased, which makes water saturations move faster. Although the permeability field is also reduced due to its correlation with the porosity, the final effect is to give more water cuts for the 3 wells, see Figs. 5.23(b), 5.23(e), and 5.24(b).

5.5 Summary

Automatic history matching with integration of both seismic impedance change data and production data was successfully applied to a real case study. The first seismic survey in the Bay Marchand field was shot long after production started, so it is necessary to match the production data first to provide an improved initial model for seismic data history matching. Due to water influx in this field, the history matching of gas production is not important although GOR data were used as observations as well as WOR data. The noise in observed seismic impedance change data is correlated, and its covariance structure was estimated by applying variogram analysis to the data gathered from the aquifer.

Through production data history matching, the water breakthrough time at all 7 wells was reproduced fairly well. The water cuts after breakthrough at some wells were matched more closely. The subsequent seismic impedance change data matching also improved the water cut match although it did not provide substantial changes in model parameters. Due to signal-to-noise ratio, the seismic impedance change did not have as large an effect on the whole automatic history matching process as it did in the synthetic and the semi-synthetic case studies.

CHAPTER VI

CONTINUOUS MODEL UPDATING USING THE ENSEMBLE KALMAN FILTER

To automatically match both production history and time-lapse seismic data by minimizing the objective function (Eq. 2.7) derived from the Bayesian framework (Tarantola, 1987) requires either the gradient of the objective function, for example, the LBFGS method in this work, or evaluation of the objective function (non-gradient based minimization methods). If the gradient is required, the adjoint method may be employed to compute the gradient. The adjoint equations, however, are highly dependent on the reservoir simulator used, i.e., they require access to the source code of the simulator. If switching to a different reservoir simulator, it is necessary to revise or even rewrite the adjoint equations, which would be very time-consuming. If non-gradient based minimization methods are chosen, thousands of simulation runs, which evaluate the objective function at each iteration step, are usually needed to find the global minimization point. When model size becomes large, it tends to be prohibitive to apply the non-gradient based minimization methods due to highly demanding simulation runs. On the other hand, with increasing deployment of permanent sensors to monitor pressure, temperature, or flow rate, the observed data become dense in time domain. To simultaneously incorporate all the data to provide a set of reservoir simulation model parameters is impractical. It is more important to keep the model up-to-date by assimilating the observed data as soon as they become available. Although the sequential data assimilation can also be realized by minimizing the objective function shown in Eq. 2.7, it is not computationally preferable because either

the adjoint code is required or the time consumed for one minimization process is too long. Moreover, for the purpose of reservoir performance prediction, it is necessary to have a set of "history-matched" models to conduct uncertainty analysis. Considering the time used to achieve one minimization process, it is not feasible to obtain a number of estimated reservoir simulation models to analyze the uncertainty. Therefore, an investigation of alternate automatic history matching methods is worthwhile.

Historically, the Kalman filter (Kalman, 1960) is the most widely used sequential data assimilation method for linear system. Since the reservoir simulation equations are highly non-linear when multiple phases co-exist, the Kalman filter is an inappropriate data assimilation method for the typical automatic history matching problems in reservoir characterization.

In 1994, Evensen (1994) introduced the ensemble Kalman filter (EnKF) as a modification of the traditional Kalman filter which could be applied to the non-linear systems. The EnKF is independent of reservoir simulators and does not require the adjoint code. It outputs a set of estimated models, which are suitable for uncertainty analysis. After its debut in 1994, the EnKF has achieved a number of successful applications in meteorology (Evensen and van Leeuwen, 1996; van Leeuwen and Evensen, 1996; Evensen, 1996; Houtekamer and Mitchell, 1998; Anderson and Anderson, 1999; Hamill and Whitaker, 2001; Houtekamer and Mitchell, 2001; Evensen, 2003). Recently, applications of the EnKF can also be found in hydrology (Reichle et al., 2002) and petroleum engineering (Nævdal et al., 2002, 2005; Gu and Oliver, 2005b,a; Liu and Oliver, 2005; Wen and Chen, 2005; Gao et al., 2005).

This chapter investigates the integration of both production data and time-lapse seismic impedance data using the EnKF. A small synthetic case study shows that it is possible to use the EnKF as an alternate automatic history matching method and to achieve satisfactory reservoir characterization results.

6.1 Kalman filter

Suppose that a discrete linear system can be modelled as

$$y_{k+1} = \phi_k y_k + w_k \,, \tag{6.1}$$

where:

- k is the time step index.
- y_k is the state vector at the time step k, which includes all parameters required to describe the system. If there are n parameters, the dimension of y_k is $n \times 1$.
- ϕ_k is the state transition matrix with dimension equal to $n \times n$.
- w_k is the vector of random noise contained in the model with dimension equal to $n \times 1$. The noise is usually assumed to be white with 0 mean and to have the known covariance matrix Q_k. It is currently assumed to be uncorrelated.

At the time step k, some measurements are obtained,

$$z_k = H_k y_k + v_k \,, \tag{6.2}$$

where,

- z_k is the measurement vector at the time step k with dimension equal to $m \times 1$.
- H_k is a matrix of dimension $m \times n$, which relates the state vector to the measurements.
- v_k is the vector of measurement error, which is usually assumed to be white noise with 0 mean and to have the known covariance matrix R_k. The dimension of v_k is $m \times 1$. It is also currently assumed to be uncorrelated.
- There is no correlation between v_k and w_k at all time steps.

Based on all available information prior to the time step k, the best estimate of the state vector is y_k^p. After incorporating the measurements z_k, the best estimate of the state vector is updated as

$$y_k^u = y_k^p + K_k(z_k - H_k y_k^p)\,, \tag{6.3}$$

where u denotes "updated", p denotes "predicted", and K_k is called the *Kalman gain* matrix. K_k can be obtained by minimizing the error covariance matrix associated with y_k^u (Brown and Hwang, 1992),

$$K_k = P_k^p H_k^T (H_k P_k^p H_k^T + R_k)^{-1}\,, \tag{6.4}$$

where P_k^p is the error covariance matrix associated with y_k^p, which is,

$$P_k^p = E[e_k^p (e_k^p)^T] = E[(y_k - y_k^p)(y_k - y_k^p)^T]\,, \tag{6.5}$$

where y_k is the truth, $e_k^p = y_k - y_k^p$ is the error in the y_k^p, and E denotes expectation. After assimilating the observed data, the error covariance matrix associated with y_k^u is

$$P_k^u = (I - K_k H_k) P_k^p\,. \tag{6.6}$$

Then, the updated state vector is advanced to the time step $k+1$ to assimilate new observations,

$$y_{k+1}^p = \phi_k y_k^u\,, \tag{6.7}$$

where the model noise vector w_k is dropped because it has 0 mean and there is no correlation between the model noise vectors at two different time steps (Brown and Hwang, 1992). Correspondingly, the error covariance matrix evolves as

$$P_{k+1}^p = \phi_k P_k^u \phi_k^T + Q_k\,. \tag{6.8}$$

Eqs. 6.3 to 6.8 can be repeated to form a recursive solution to the linear data filtering problem, which is called the Kalman filter.

Although "... the Kalman filter represents the most widely applied and demonstrably useful result to emerge from the state variable approach of *modern control theory*." (Sorenson, 1985), it is inapplicable to non-linear systems. The extended Kalman filter (EKF) applies the ideas of the Kalman filter to the non-linear systems based on linearizations of the non-linear models. However, when non-linearities are severe or the model size becomes large, the EKF is not suitable. For large scale non-linear systems, the real promising approach is the ensemble Kalman filter.

6.2 Ensemble Kalman filter (EnKF)

The basic methodology of the EnKF consists of the forecast step and the assimilation step. The forecast step is to advance the state vectors from the previous time step to the next time step. At the time step where the observations are available, the forecast step stops and the assimilation step starts to assimilate the data which updates the state vectors. The following introduces the EnKF using reservoir characterization terminology.

If the forward modelling is achieved by using a reservoir simulator, the state vector typically includes porosity ϕ, log permeability $\ln k$, pressure p, and phase saturations at each reservoir simulation gridblock. Besides the model parameters, the state vector also includes the reservoir response output from the reservoir simulator, such as P_{wf}, WOR, GOR, and time-lapse seismic data. Thus, the state vector can be written as

$$y_k = \begin{bmatrix} \boldsymbol{\phi} & \mathbf{ln}\,\boldsymbol{k} & \boldsymbol{p} & \boldsymbol{S} & \boldsymbol{d} \end{bmatrix}^T , \tag{6.9}$$

where k is the time step index and d denotes the computed data. If the number of gridblocks is N_m and the number of computed data is N_d, the dimension of y_k is $4 \times N_m + N_d$. If the reservoir simulator is denoted using f, the forecast step can be written as

$$y_{k,j} = f(y_{k-1,j}) \quad (j = 1, 2, \cdots, N_e) , \tag{6.10}$$

where j is the ensemble member index and N_e is the number of ensemble members. Using u to denote "updated" and p to denote "predicted", Eq. 6.10 becomes into

$$y^p_{k,j} = f(y^u_{k-1,j}) \quad (j = 1, 2, \cdots, N_e)\,, \tag{6.11}$$

where $y^u_{k-1,j}$ is the jth updated state vector at the time step $k-1$ and $y^p_{k,j}$ is the estimate of the jth state vector based on all available information prior to the time step k. Note that only dynamic variables, i.e., pressure and saturations, and the computed data change between $k-1$ and k. The static variables, i.e., porosity and permeability, remain unchanged during the same time interval. They are adjusted as well as the dynamic variables during the assimilation step.

At the time step k, some measurements are obtained,

$$d_{\text{obs,k}} = d_{\text{true,k}} + \epsilon_k\,, \tag{6.12}$$

where the dimension of $d_{\text{obs,k}}$ is $N_d \times 1$ and ϵ_k is the measurement noise with dimension equal to $N_d \times 1$, is usually assumed to be Gaussian. The covariance matrix of ϵ_k is $C_{D,k} = E[\epsilon_k \epsilon_k^T]$, with dimension equal to $N_d \times N_d$, is typically assumed to be diagonal if only production observations are used. By assimilating the observed data, the state vectors are updated using Eq. 6.13,

$$y^u_{k,j} = y^p_{k,j} + K_{e,k}(d_{\text{obs,k,j}} - H_k y^p_{k,j}) \quad (j = 1, 2, \cdots, N_e)\,, \tag{6.13}$$

where:

- $d_{\text{obs,k,j}}$ is the perturbed observation vector for the jth ensemble member by adding random noise to the observation $d_{\text{obs,k}}$ (Burgers et al., 1998).
- $H_k = [0 \mid I]$ is the operator matrix with dimension equal to $N_d \times (4 \times N_m + N_d)$. $H_k y^p_{k,j}$ extracts the computed data from the jth state vector corresponding to its observations.

In Eq. 6.13, $K_{e,k}$ is also called the *Kalman gain* matrix. The dimension of $K_{e,k}$ is $(4 \times N_m + N_d) \times N_d$. In contrast to the Kalman filter, $K_{e,k}$ is computed from the ensemble members using Eq 6.14,

$$K_{e,k} = P^p_{e,k} H_k^T (H_k P^p_{e,k} H_k^T + C_{D,k})^{-1} , \tag{6.14}$$

where e denotes "ensemble" and $P_{e,k}$ is the covariance matrix among the ensemble members, which is

$$P^p_{e,k} = \frac{1}{N_e - 1} \sum_{j=1}^{N_e} \left(y^p_{k,j} - \bar{y}^p_k\right) \left(y^p_{k,j} - \bar{y}^p_k\right)^T , \tag{6.15}$$

where $\bar{y}^p_k$ is the averaged state vector.

Combining Eqs. 6.11 to 6.15, a preliminary EnKF loop is formed as shown:

Step 1 Input the ensemble state vectors into the reservoir simulator and advance them in time. If it is the first time step, all the vectors are filled with initial values.

Step 2 At the time step k when the observations are available, stop advancing and fill the state vectors with the current model parameters and computed data.

Step 3 Compute the averaged state vector using Eq. 6.16,

$$\bar{y}^p_k = \frac{1}{N_e} \sum_{j=1}^{N_e} y^p_{k,j} . \tag{6.16}$$

Step 4 Compute the ensemble covariance matrix $P^p_{e,k}$ using Eq. 6.15.

Step 5 Compute the *Kalman gain* matrix using Eq. 6.14.

Step 6 Update the state vectors using Eq. 6.13.

Step 7 If the current time step is the final step, then **STOP**. Otherwise, go back to **Step 1**.

Although the preliminary loop is a good starting point, it is not a practical algorithm because of the matrix computation expense. In Eq. 6.15, the dimension of $P^p_{e,k}$ is $(4 \times N_m + N_d) \times (4 \times N_m + N_d)$. To explicitly form and store $P^p_{e,k}$ requires a large amount of computer resources, which makes the loop impractical even for a medium-size problem. Therefore, the key point to achieve a feasible algorithm is to avoid the explicit computation of $P^p_{e,k}$. In matrix form, Eq. 6.15 can be written as

$$P^p_{e,k} = \frac{1}{N_e - 1} \Delta Y^p_k (\Delta Y^p_k)^T \,, \tag{6.17}$$

where ΔY^p_k consists of N_e column vectors, each of which is the difference between an ensemble state vector and the averaged state vector. Applying Eq 6.17 to Eq. 6.14, the *Kalman gain* matrix has the new form as

$$\begin{aligned} K_{e,k} &= \frac{1}{N_e - 1} \Delta Y^p_k (\Delta Y^p_k)^T H^T_k \left(H_k \frac{1}{N_e - 1} \Delta Y^p_k (\Delta Y^p_k)^T H^T_k + C_{D,k} \right)^{-1} \\ &= \frac{1}{N_e - 1} \Delta Y^p_k \left(H_k \Delta Y^p_k \right)^T \left(\frac{1}{N_e - 1} H_k \Delta Y^p_k (H_k \Delta Y^p_k)^T + C_{D,k} \right)^{-1} . \end{aligned} \tag{6.18}$$

Since H_k is the operator matrix used to extract entries corresponding to data, $H_k \Delta Y^p_k$ does not involve matrix computation. In addition, only ΔY^p_k needs to be formed and stored. Since the dimension of ΔY^p_k is $(4 \times N_m + N_d) \times N_e$, much less computer resource is required than computing $P^p_{e,k}$. Thus, a feasible EnKF algorithm is formed:

Step 1 Input the ensemble state vectors into the reservoir simulator and advance them in time. If it is the first time step, all the vectors are filled with initial values.

Step 2 At the time step k when the observations are available, stop advancing and fill the state vectors with the current model parameters and computed data.

Step 3 Compute the averaged state vector using Eq. 6.19,

$$\bar{y}^p_k = \frac{1}{N_e} \sum_{j=1}^{N_e} y^p_{k,j} \,. \tag{6.19}$$

Step 4 Form the difference matrix ΔY_k^p and take entries from ΔY_k^p using H_k, which is $H_k \Delta Y_k^p$.

Step 5 Compute the *Kalman gain* matrix using Eq. 6.18.

Step 6 Update the ensemble state vectors using Eq. 6.13.

Step 7 If the current time step is the final step, then **STOP**. Otherwise, go back to **Step 1**.

6.3 Integration of time-lapse seismic impedance data into the EnKF

Both the observed and the computed seismic impedance data were calculated using the output from the reservoir simulator. The rock physics model used is the Gassmann (Gassmann, 1951) and Han (Han et al., 1986) equations. Since it is a synthetic case study, some typical lithology values are used. The reservoir simulator is an oil-water simulator. Because no gas phase exists, oil and water properties do not change much with pressure. Thus, constant bulk moduli of oil and water were used. The parameters used to compute the seismic impedance are listed in Table 6.1.

Parameter	Value
Shaliness	0.2
Sand Modulus (Pa)	3.8×10^{10}
Clay Modulus (Pa)	2.12×10^{10}
Density of Solid (kg/m^3)	2650
Modulus of Water (Pa)	2.39×10^9
Modulus of Oil (Pa)	6.71×10^8

Table 6.1: Parameters used for seismic impedance calculation

Since an impedance datum at one gridblock is computed using only the pressure and saturation at the gridblock, the observation noise covariance matrix $C_{D,k}$ is still

reasonably assumed to be diagonal. For real case studies, however, a non-diagonal $C_{D,k}$ probably needs to be constructed (Aanonsen et al., 2002, 2003).

In this work, the time-lapse seismic impedance data are assimilated as two data sets from two separate seismic surveys. Because seismic impedance data are much more sensitive to porosity than to permeability, the porosity field was recovered better than the permeability field in the synthetic case study.

For the impedance data from the first seismic survey, the EnKF assimilated them one by one, which is: 1) form the local ensemble state vectors in one gridblock and assimilate the seismic impedance datum in that gridblock; 2) adjust variables in the state vectors only belonging to the gridblock; 3) gather the locally adjusted state vectors to form the global state vectors and advance them in time. For the second seismic survey, the EnKF assimilated all the impedance data simultaneously because our study showed that there was a sensitivity connection across the whole reservoir model arising from the fluid flow.

6.4 Improved initial member sampling

The EnKF uses the sample mean and sample covariance to approximate the population mean and population covariance (Evensen, 1994, 2003), so to use a large number of ensemble members is presumably better than to use a small number of ensemble members. Considering the computation expense, however, the number of ensemble members must be kept small. Since the adjustments in the EnKF are within the space spanned by the ensemble members, a small number of members may not be able to provide large enough adjustment freedom, resulting in filter divergence (Evensen, 1994; Houtekamer and Mitchell, 1998; Anderson and Anderson, 1999; Anderson, 2001; Evensen, 2003, 2004).

In this work, the improved initial member sampling method (Evensen, 2004) was used to generate the initial ensemble members, which ensured a stable filter behavior.

The sampling algorithm is:

Step 1 Generate N_T ensemble members by drawing samples from the prior PDF and compute the corresponding difference matrix ΔY.

Step 2 Do the Singular Value Decomposition (hereafter SVD) of ΔY, $\Delta Y = U\Lambda V^T$, where U is the left orthogonal matrix, V is the right orthogonal matrix and Λ is a diagonal matrix with the singular values of ΔY as its diagonal entries.

Step 3 Choose the first N_e largest singular values from Λ and store them into the matrix Λ_e. Correspondingly, the first N_e column vectors of U are chosen and saved into the matrix U_e.

Step 4 Generate a $N_e \times N_e$ random matrix by sampling $N(0, 1)$.

Step 5 Do the SVD of the random matrix and save its right orthogonal matrix to the matrix V_e.

Step 6 Compute the difference matrix with smaller size, $\Delta Y_e = U_e \Lambda_e V_e^T$.

Step 7 Scale ΔY_e by dividing $\sqrt{\alpha}$, where $\alpha = N_T/N_e$.

Step 8 Adjust ΔY_e to ensure that its mean is zero and its variance meets the requirement.

Step 9 Use ΔY_e to start the EnKF loop.

The ensemble members generated using the algorithm can keep the sample statistics introduced by the original large ensemble set. They provide larger adjustment space than that from same number of ensemble members by sampling the prior PDF.

6.5 A small synthetic case study

6.5.1 Model description

This is a 2-D, 2-phase, water flooding problem. The reservoir simulation model has 16×16 gridblocks, each of which has equal volume, $60 \times 60 \times 40\ ft^3$. There are 5 wells: 1 injector at the center and 4 producers at the four corners. All 5 wells have constant bottomhole pressures so that only variable water injection rate and water/oil production rates are available to be assimilated as production data in the EnKF. The reservoir produces 200 days. The first seismic survey is at day 1 and the second seismic survey is at day 198. The true model is generated by drawing a sample from the prior PDF, which provides the observed production and seismic impedance data. Table 6.2 gives data distribution times. The true observations are perturbed twice

Time (Day)	Water Rate	Oil Rate	Seismic Impedance
1	N/A	N/A	256
10	5	4	N/A
20	5	4	N/A
...	...	...	...
190	5	4	N/A
198	N/A	N/A	256
200	5	4	N/A

Table 6.2: Assimilated data at different time steps

with random noise sampled from $N(0, 1)$ to generate observations for each ensemble member. The true model and the initial ensemble members use the same exponential variogram, whose parameters are listed in Table 6.3.

The true log permeability and porosity are shown in Fig. 6.1. The 4 black points in Fig. 6.1(a) stand for the 4 producers and the centered gray point denotes the injector. The water saturation distribution at day 200 is shown in Fig. 6.2. The producer at the left lower corner (hereafter well Prod-1) has water breakthrough.

Two ensembles were used as initial members for the EnKF independently to compare the effects from improved initial member sampling algorithm. One ensemble has

Parameter	Log Permeability	Porosity
Mean	5.5	0.2
Standard deviation	0.5	0.02
Range along X (gridblocks)	9	9
Range along Y (gridblocks)	6	6
Correlation coefficient	0.5	

Table 6.3: Variogram parameters of log permeability and porosity

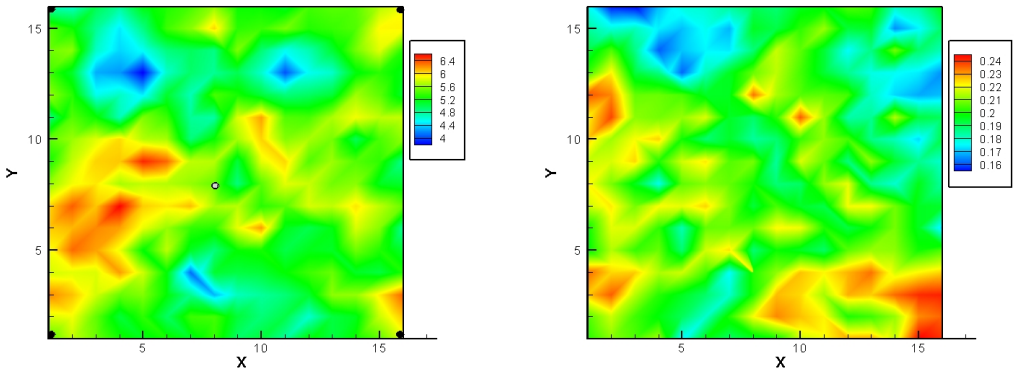

(a) Log permeability (b) Porosity

Figure 6.1: True log permeability and porosity

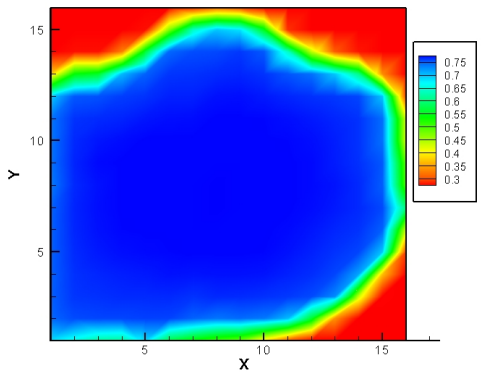

Figure 6.2: True water saturation distribution at day 200

128 members generated by directly sampling the prior PDF. The other one also has 128 members, which were re-generated from a 256-member group. They are called M128 group and M128F256 group respectively in the following sections. In two cases using those two groups, same observations were used. Local data assimilation was used for both cases to assimilate the first seismic data group.

6.5.2 M128 case

In Fig. 6.3, water injection rate at the injector is shown, where the red lines go

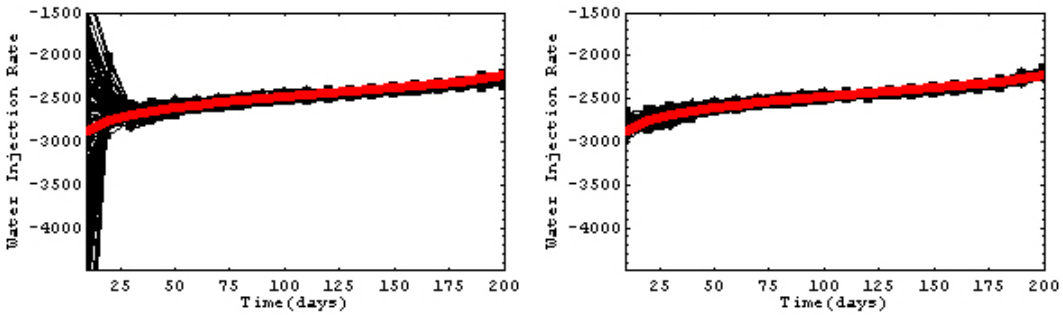

(a) Before EnKF (b) After EnKF

Figure 6.3: Water rate (STB/Day) at the injector before and after the EnKF (M128 case)

through all observed water injection rates and all blacks lines are computed data from all ensemble members. Following traditions in reservoir simulation, water injection rate is shown as negative. Before the EnKF, it can be seen that the variation in injection rates is large, especially at the early time (Fig. 6.3(a)). After the EnKF, the injection rates at all ensemble members become closer to the true rate, see Fig. 6.3(b). Fig. 6.4 shows the water production rates before and after the EnKF in the well Prod-1. From the red lines, it can be seen that the true model has water breakthrough around day 180. Before the EnKF, a few of ensemble members can not capture the correct time, see Fig. 6.4(a). After the EnKF, all ensemble members have both correct water breakthrough time and water production rate afterward (Fig. 6.4(b)). The three other wells do not have water breakthrough, so only oil production rates

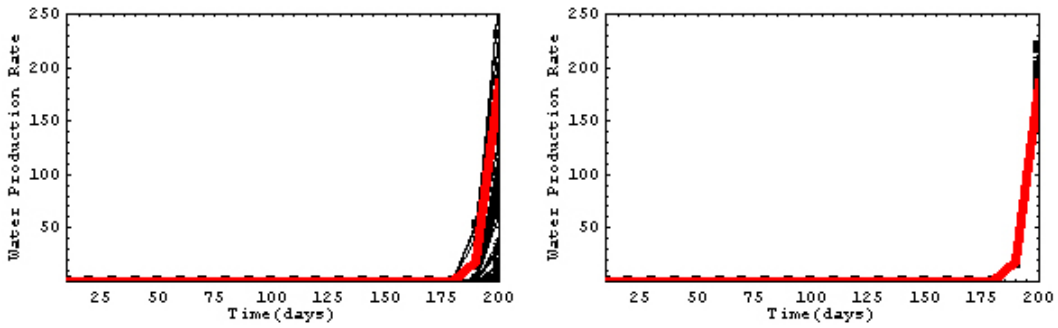

(a) Before EnKF (b) After EnKF

Figure 6.4: Water rate (STB/Day) at the well Prod-1 before and after the EnKF (M128 case)

need to be honored. Fig. 6.5 shows the oil production rates at all 4 production wells. After the EnKF, the oil production rates from all ensemble members are distributed more closely around the observations.

The two seismic impedance data are also honored very well after the EnKF, which can be seen from Fig. 6.6. The mean of seismic impedance data from all ensemble members after the EnKF has very strong correlation with the observed impedance data. The second impedance cross plot has more scattered points because in this example, the initial saturation and pressure were assumed to be known so that pressure and saturation distributions have higher uncertainties at the second seismic survey time than those at the first survey time.

The final mean of permeability and porosity fields after assimilating all data are shown in Fig. 6.7. Compared with the truth shown in Fig. 6.1, it can be seen that the porosity field has been recovered very well. Only a few features of the true permeability field are captured in the estimate, for example, the high permeability spot between the injector and the well Prod-1. The reason for the large difference is that seismic impedance data have higher sensitivity to porosity than to permeability. This difference is more obvious from the cross plots shown in Fig. 6.8. The red lines in Figs. 6.6 and 6.8 are linear regression lines. All have the same forms, $Y_{\text{true/obs}} = A + B * X_{\text{est./comp.}}$. Values of the coefficients A, B and correlation coefficients R are listed in

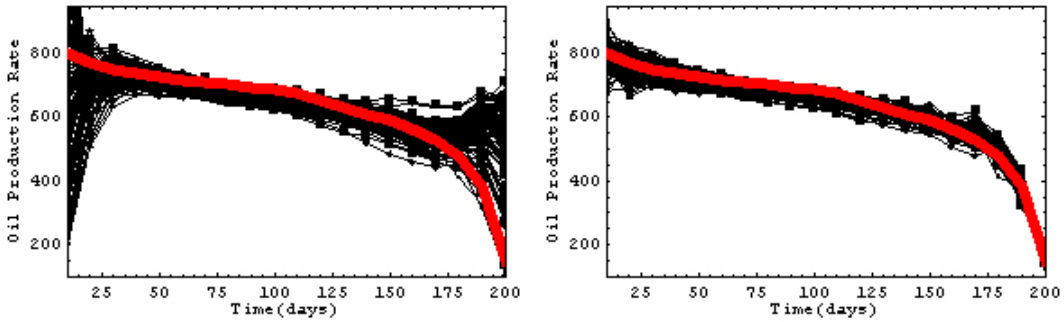

(a) Prod-1 before EnKF

(b) Prod-1 after EnKF

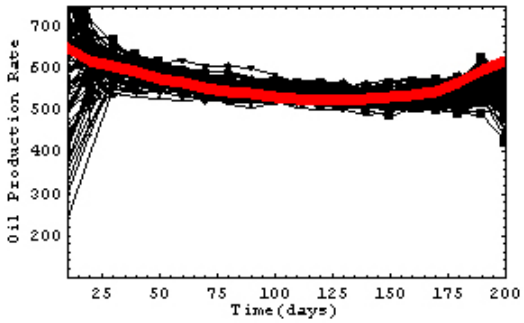

(c) Prod-2 before EnKF

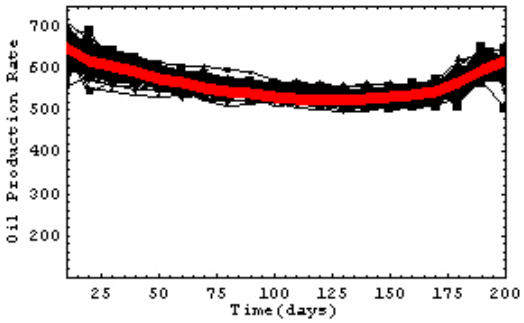

(d) Prod-2 after EnKF

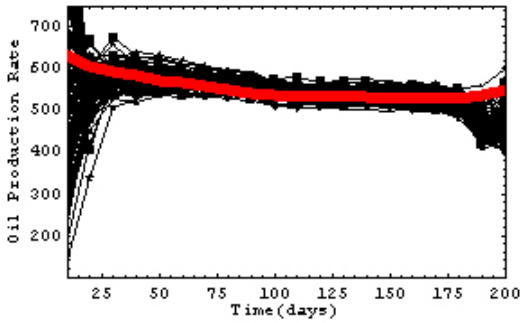

(e) Prod-3 before EnKF

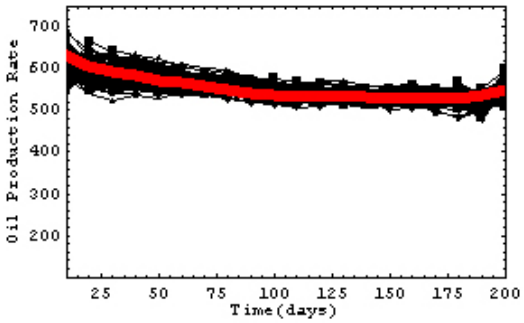

(f) Prod-3 after EnKF

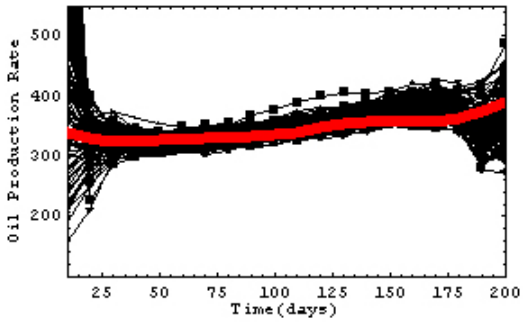

(g) Prod-4 before EnKF

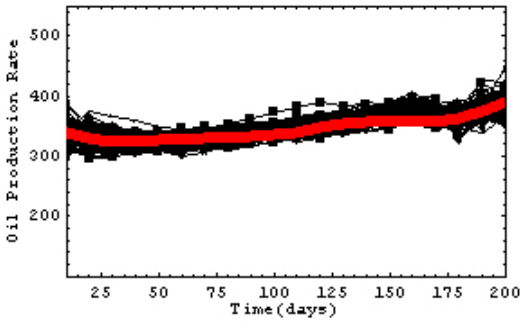

(h) Prod-4 after EnKF

Figure 6.5: Oil rates (STB/Day) at the producers before and after the EnKF (M128 case)

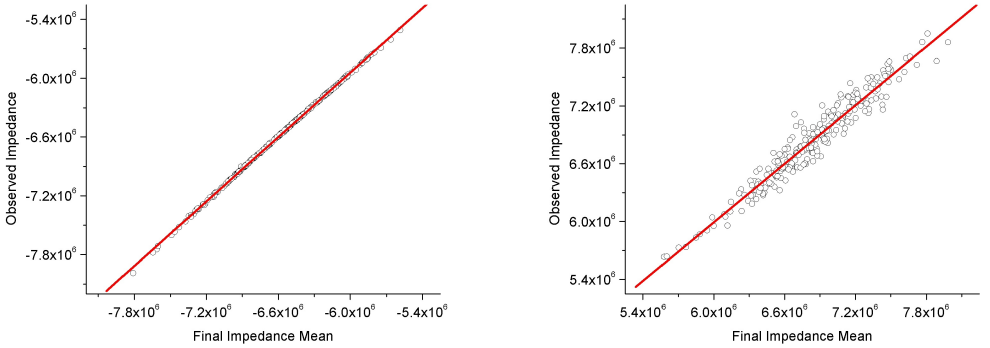

(a) First seismic impedance (b) Second seismic impedance

Figure 6.6: Cross plots of seismic impedance (M128 case)

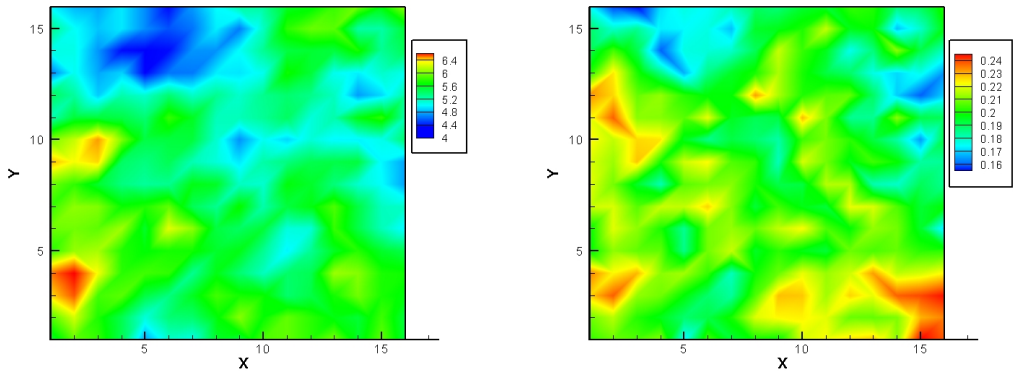

(a) Log permeability (b) Porosity

Figure 6.7: Final mean of log permeability and porosity (M128 case)

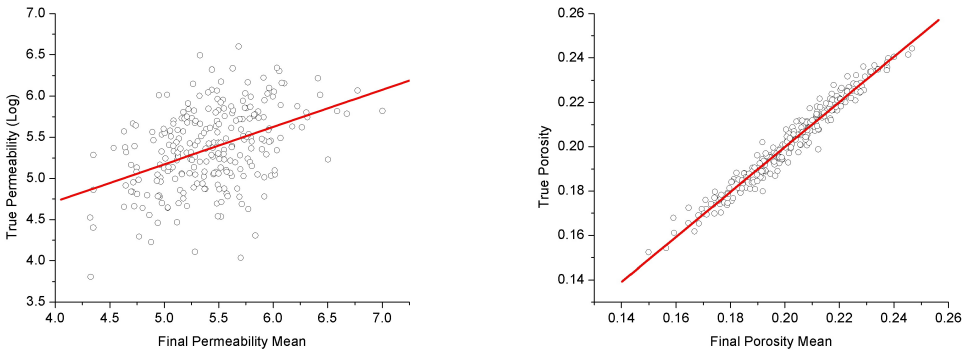

(a) Log permeability (b) Porosity

Figure 6.8: Cross plots of permeability and porosity (M128 case)

Table 6.4. The regression parameters also show that seismic data have been honored

Parameter	A	B	R
Porosity	-0.00299	1.0146	0.97927
Log permeability	2.90479	0.45336	0.42081
First seismic impedance	6.333×10^5	1.09592	0.99975
Second seismic impedance	-8.435×10^4	1.01278	0.96781

Table 6.4: Regression parameters of porosity, log permeability, and impedance (M128 case)

very well; porosity field has been estimated much better than the permeability field.

The EnKF continuously adjusts ensemble members by assimilating observation data to make the mean of ensemble members closer to the truth. Hence, the deviation between ensemble members and the truth at each gridblock can measure how close the estimations are to the true models. The deviation of each variable from the truth is defined as

$$\sigma_i = \sqrt{\frac{1}{N_e}\sum_{j=1}^{N_e}\left(y_{i,j} - y_{\mathrm{true,i}}\right)^2} \quad (i = 1, 2, \cdots, N_m)\,, \tag{6.20}$$

where N_e is the number of ensemble members and N_m is the number of gridblocks. It is expected to get smaller with more data assimilation. In Fig. 6.9, evolution of permeability deviation from the truth is shown. To have a better comparison, all plots use the same color scale, where blue color stands for the lowest value and red color for the highest value. The initial ensemble members have high deviation from the truth so most of the field is full of green and red colors, see Fig. 6.9(a). In day 1, after the first seismic data assimilation, the spot previously filled with red color in the left upper corner becomes smaller and the red color changes into yellow color; more gridblocks have light blue colors, which shows that seismic data assimilation helps to adjust permeabilities of the ensemble members toward the true values (Fig. 6.9(b)). In day 10, the first production data assimilation day, more gridblocks reduce their deviation and the red spot in left upper corner almost disappears (Fig. 6.9(c)). Then, as more data are assimilated, more reduction is obtained, see Figs. 6.9(d) to 6.9(g).

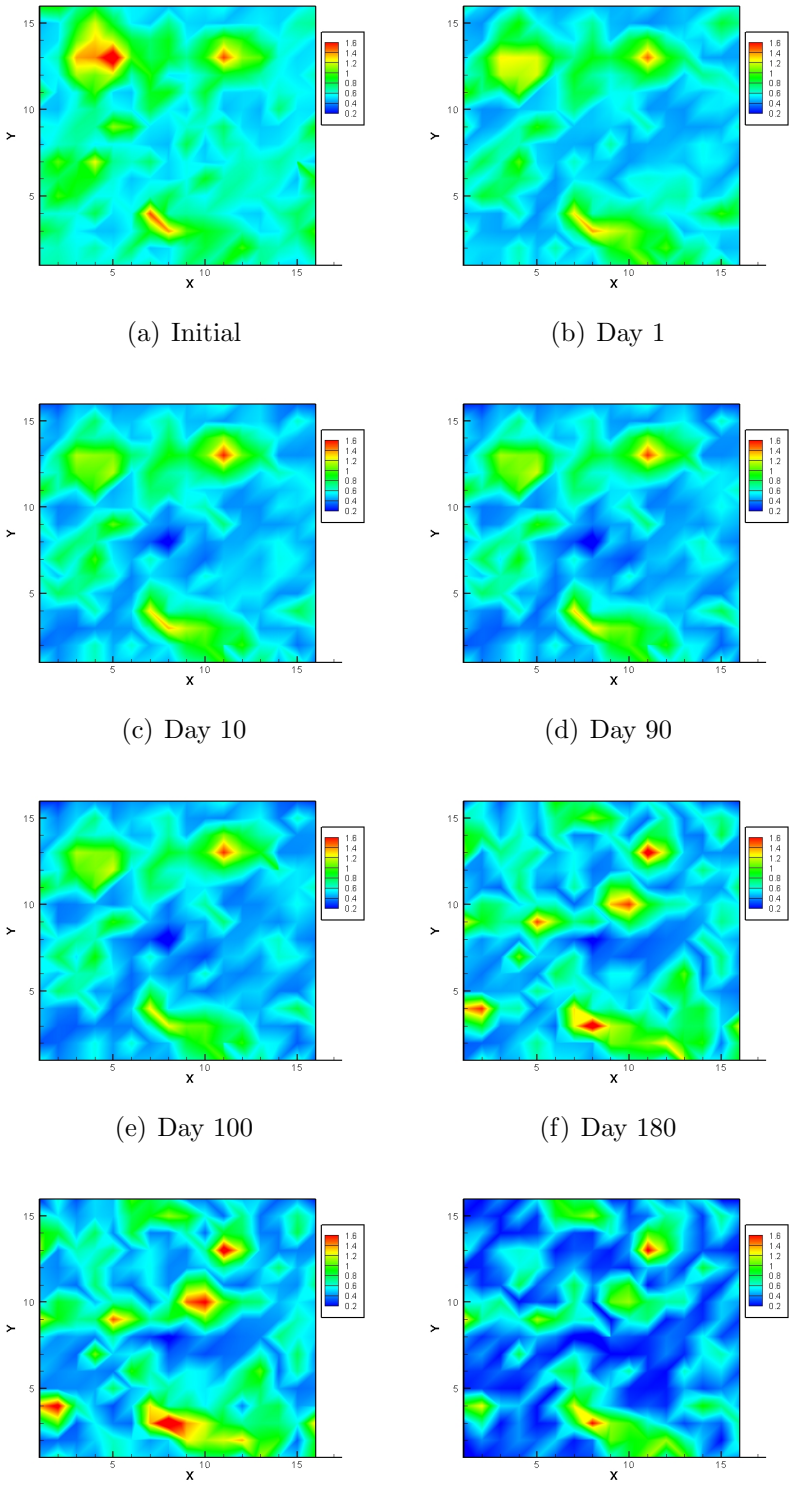

(a) Initial (b) Day 1

(c) Day 10 (d) Day 90

(e) Day 100 (f) Day 180

(g) Day 190 (h) Day 198

Figure 6.9: Evolution of permeability deviation from the truth (M128 case)

In Fig. 6.9(f) and Fig. 6.9(g), however, some high deviation blocks appear again, which are from over-adjustments around water breakthrough time at the well Prod-1. Fortunately, they are reduced by assimilating the second seismic impedance data, see Fig. 6.9(h).

The same deviation in Eq. 6.20 is also computed for porosity and shown in Fig. 6.10. Same color scale is used to provide a clearer comparison along time axis. The initial deviation map has only red color, see Fig. 6.10(a), which shows that even the smallest deviation value in the initial map is larger than the biggest value in day 198, see Fig. 6.10(h). As can be seen from permeability deviation evolution, the porosity also experiences reduction with more data assimilated, see Figs. 6.10(b) to 6.10(e). The two seismic impedance data assimilations have obvious effects: the first one reduces the deviation in all gridblocks, which makes the red color in the initial map disappear completely (Fig. 6.10(b)), and the second one reduces the high deviation blocks that come from over-adjustments around water breakthrough time at the well Prod-1, see Figs. 6.10(h), 6.10(f), and 6.10(g).

Another effective tool to measure the EnKF behavior is called the integrated **R**oot **M**ean **S**quare (**RMS**) error, which is a distance between ensemble mean and the truth. The definition is in Eq. 6.21,

$$RMS = \sqrt{\frac{1}{N_m}\sum_{i=1}^{N_m}\left(\frac{1}{N_e}\sum_{j=1}^{N_e} y_{i,j} - y_{\text{true,i}}\right)^2}, \tag{6.21}$$

where N_m is the number of gridblocks and N_e is the number of ensemble members. Different from the deviation defined in Eq. 6.20, the **RMS** error is a scalar and sums over both ensemble members and gridblocks. The **RMS** error of both permeability and porosity along with time are shown in Fig. 6.11. From Fig. 6.11(b), it can be seen that after the first seismic impedance data assimilation at day 1, the porosity **RMS** error drops about one order of magnitude, which is also reflected through the dramatic reductions in the deviation maps, see Fig. 6.10(a) and Fig. 6.10(b).

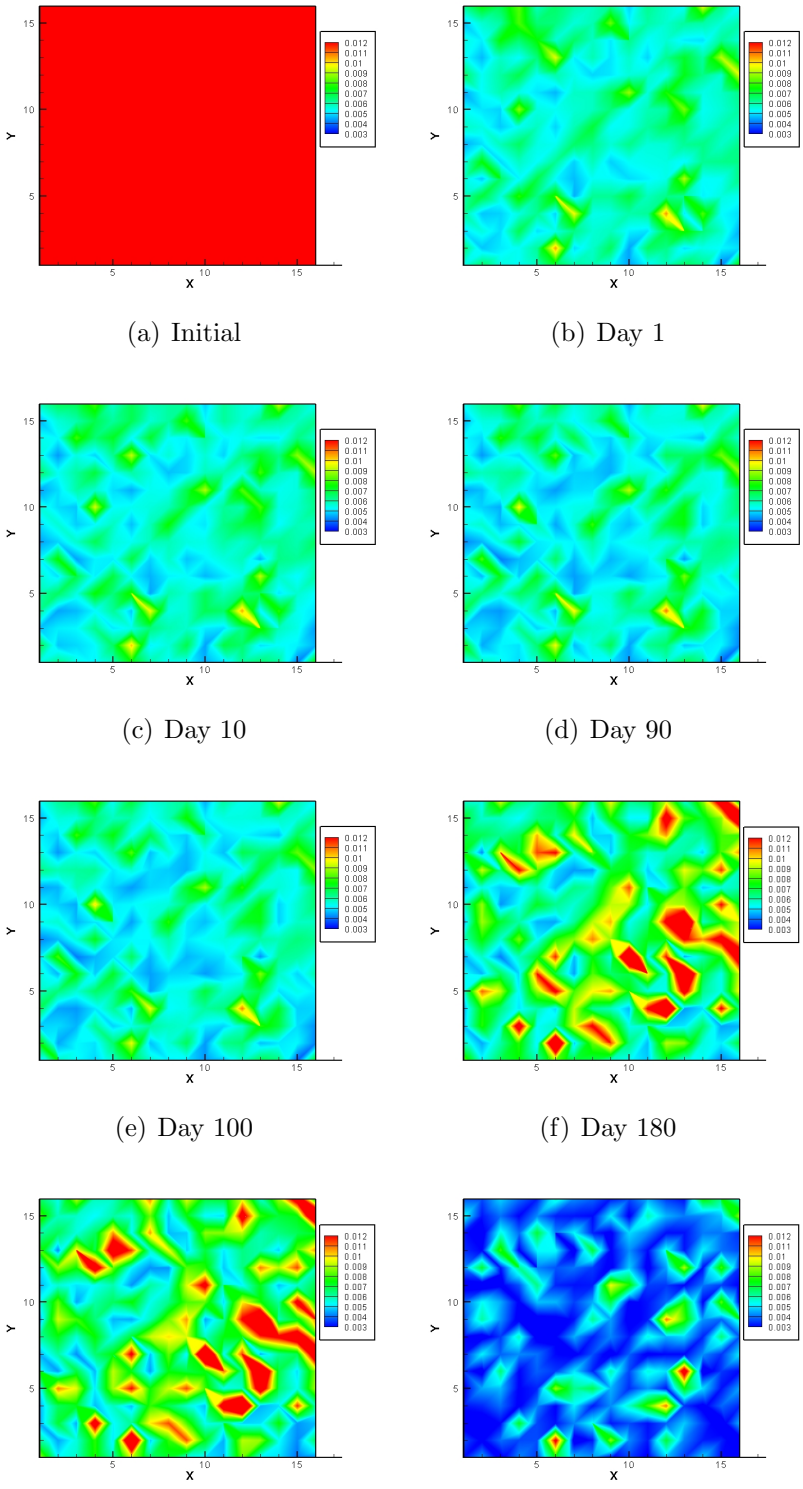

(a) Initial (b) Day 1

(c) Day 10 (d) Day 90

(e) Day 100 (f) Day 180

(g) Day 190 (h) Day 198

Figure 6.10: Evolution of porosity deviation from the truth (M128 case)

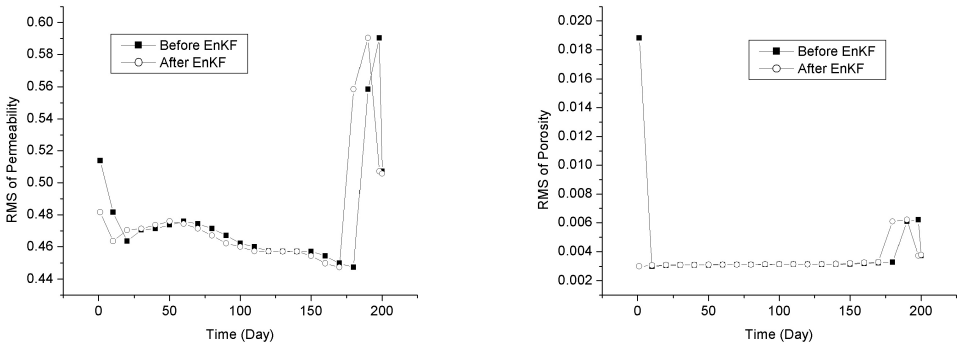

(a) Log permeability (b) Porosity

Figure 6.11: **RMS** error of permeability and porosity (M128 case)

Between day 1 and day 170, however, production data assimilation does not provide any substantial changes to the **RMS** error, which can also be seen from the deviation maps shown in Figs. 6.10(c) to 6.10(e), where patterns in all maps are barely changed. The reason is that seismic impedance data are so sensitive to porosity that even one data assimilation has been able to adjust the ensemble mean to be very close to the true porosity field. The mean porosity field after seismic data assimilation at day 1 is shown in Fig. 6.12. Comparing it with the true porosity field and the mean

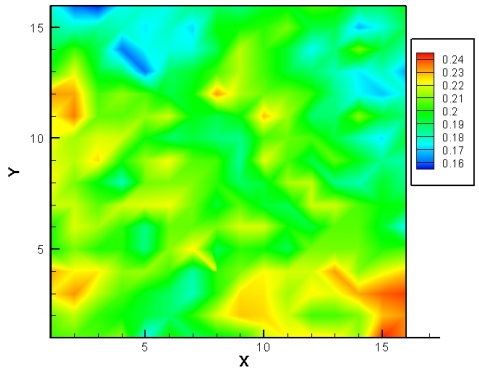

Figure 6.12: Mean porosity field after seismic data assimilation at day 1 (M128 case)

porosity field at day 200 shown in Figs. 6.1(b) and 6.7(b), it is clear that the porosity estimate at day 1 is very good. Hence, subsequent production data assimilation will

not provide much information. Around water breakthrough time at the well Prod-1, day 180 to day 190, the porosity **RMS** error increases to a high value, which again decreases after the second seismic impedance data assimilation at day 198. This phenomenon is also clear through Figs. 6.10(f) to 6.10(h).

For the permeability **RMS** error, see Fig. 6.11(a), the first seismic data assimilation provides a small reduction. It is understandable that the reduction in permeability error is small because at day 1, the flow field is poorly developed and it is hard for seismic data to capture permeability. Between day 1 and day 180, production data assimilation results in a small steady reduction in the **RMS** error. That is why in Figs. 6.9(b) to 6.9(e), more and more gridblocks change colors from green to blue. Around water breakthrough time at the well Prod-1, very dramatic oscillations appear. After the second seismic data assimilation, the permeability **RMS** error is reduced back to a value that is just a little bit smaller than the initial one. Note that the **RMS** error is an average of all ensemble members at all gridblocks so that a few large values can have a large effect on the value. In Fig. 6.9(h), about one third of gridblocks are still in green colors although other blocks are in blue, which partly explains why improvements in the **RMS** error plot are less obvious than in the deviation map.

In this M128 case, both production data and seismic impedance data have been honored very well. The porosity field has also been recovered successfully. However, the permeability estimate is poor. The **RMS** error of permeability estimate does not reduce much after assimilating all data and has severe oscillation around water breakthrough time. This problem can be solved by increasing the size of the ensemble or by using the improved initial member sampling algorithm, which is shown in the next section.

6.5.3 M128F256 case

In this case, the initial 128 ensemble members were generated from a 256 ensemble group by using the improved initial member sampling algorithm.

Water injection rate at the injector is shown in Fig. 6.13, both before and after the EnKF. As before, red lines stand for observation and black lines are for ensemble members. Since water injection rate is also honored quite well in M128 case, there is

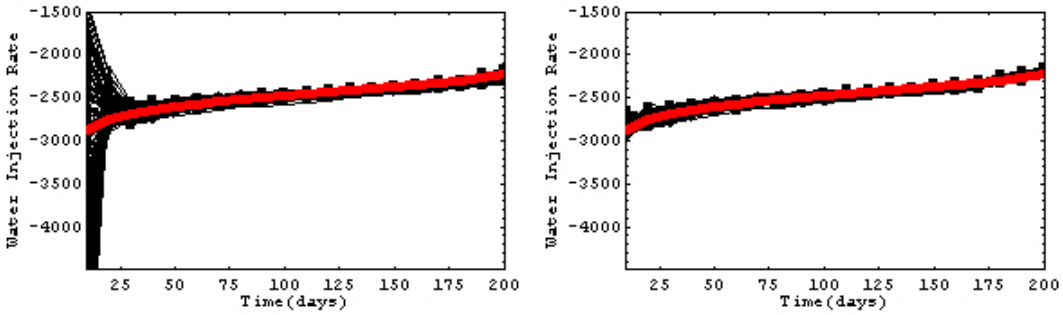

(a) Before EnKF (b) After EnKF

Figure 6.13: Water rate (STB/Day) at the injector before and after the EnKF (M128F256 case)

not much difference between Fig. 6.13(b) and Fig. 6.3(b). The only visible improvements occur around day 25, where the black lines in Fig. 6.13(b) are closer to the observation than the black lines in Fig. 6.3(b).

Water production rate at the well Prod-1 before the EnKF and after the EnKF is shown in Fig. 6.14. After the EnKF, water production rate is honored very well, too (Fig. 6.14(b)). Before the EnKF, more ensemble members approximately capture water breakthrough time compared to the M128 case (Fig. 6.4(a)), which shows that the ensemble members in M128F256 case have better property estimates before water breakthrough at day 180.

Oil production rates at all four production wells before and after the EnKF are shown in Fig. 6.15. The EnKF provides adjustments to all ensemble members at four wells so that computed oil production rates are distributed closely around the

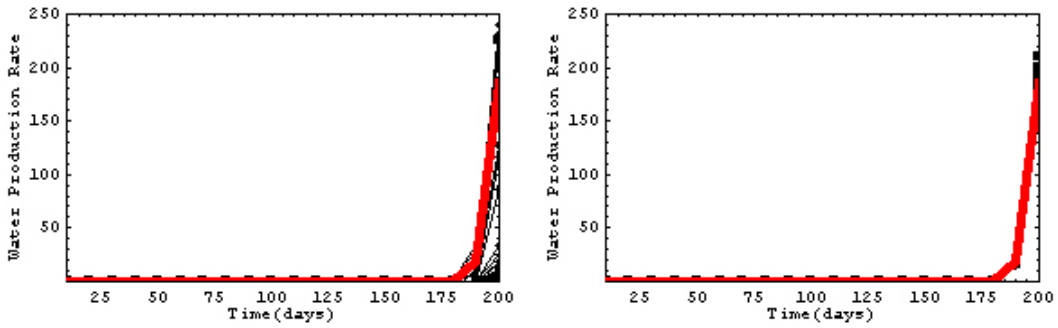

(a) Before EnKF (b) After EnKF

Figure 6.14: Water rate (STB/Day) at the well Prod-1 before and after the EnKF (M128F256 case)

observation (Figs. 6.5(b), 6.5(d), 6.5(f), and 6.5(h)). From Figs. 6.13, 6.14, and 6.15, it can be seen that no substantial improvements in honoring production data are gained by re-sampling initial members.

Seismic data matching does not gain obvious changes either (see cross plots in Fig. 6.16). The correlation between the observed seismic impedance and the seismic impedance mean at the time of the first seismic survey is still very strong (Fig. 6.16(a). The second one has relatively more scattered points, but still is well correlated. The small improvements are reflected through correlation coefficients of the regression lines (red lines in Fig. 6.16), listed in Table 6.5.

The final mean of permeability field and porosity field are shown in Fig. 6.17. Similar to the M128 case, porosity mean (Fig. 6.17(b)) is well estimated of the true field (Fig. 6.1(b)). Even most of the detailed features are recovered by the EnKF. The permeability mean (Fig. 6.17(a)), however, looks much different from its counterpart shown in Fig. 6.7(a). The big blue spot at upper left corner of Fig. 6.7(a) is replaced with a small narrow blue stripe in the same place of Fig. 6.17(a). At lower left corner in Fig. 6.17(a), more gridblocks have high permeability values, which is also an improvement compared to the true permeability field.

Cross plots of permeability and porosity between the truth and the mean are shown in Fig. 6.18. It can be seen that correlation between the permeability mean

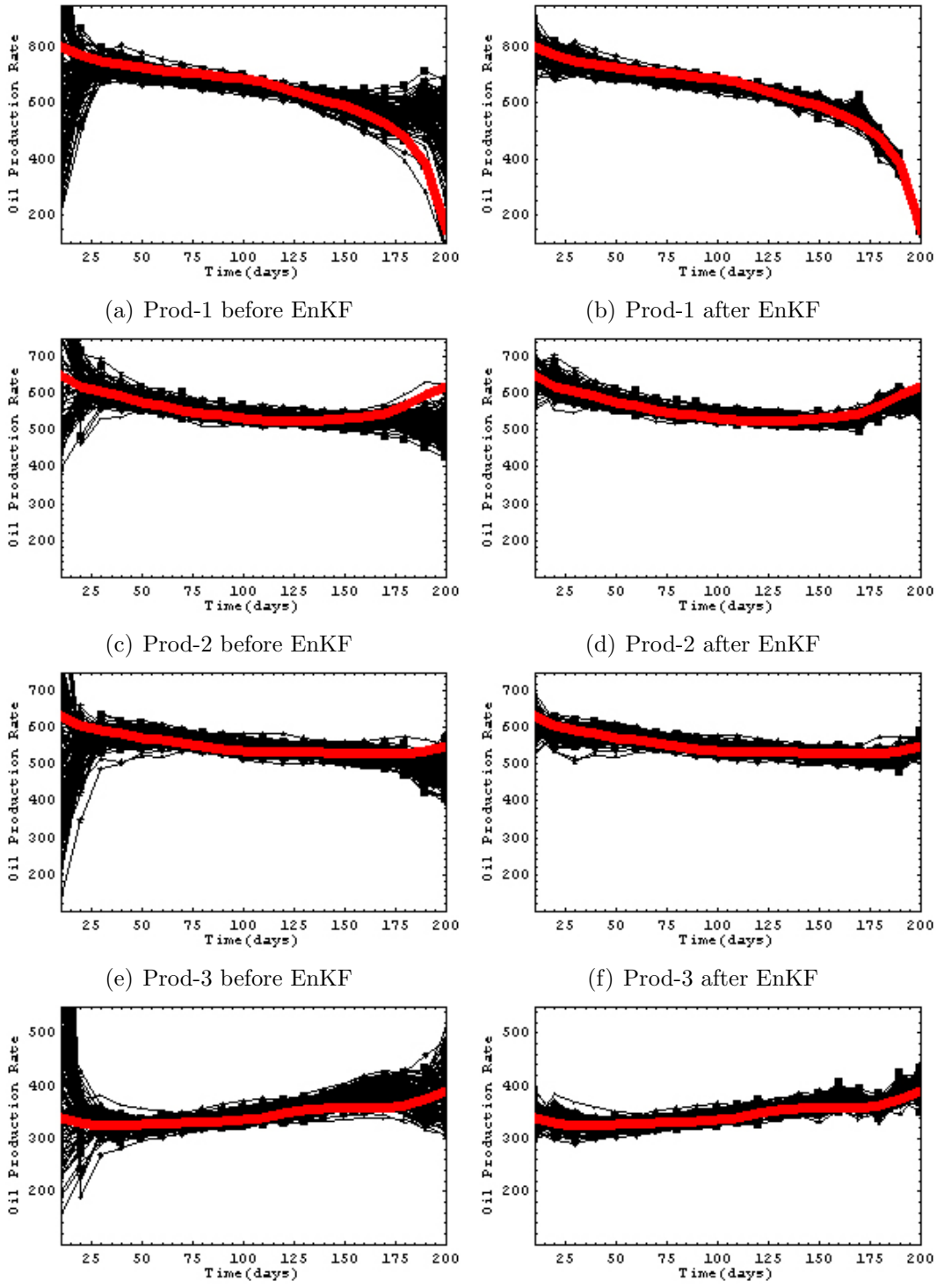

(a) Prod-1 before EnKF

(b) Prod-1 after EnKF

(c) Prod-2 before EnKF

(d) Prod-2 after EnKF

(e) Prod-3 before EnKF

(f) Prod-3 after EnKF

(g) Prod-4 before EnKF

(h) Prod-4 after EnKF

Figure 6.15: Oil rates (STB/Day) at the producers before and after the EnKF (M128F256 case)

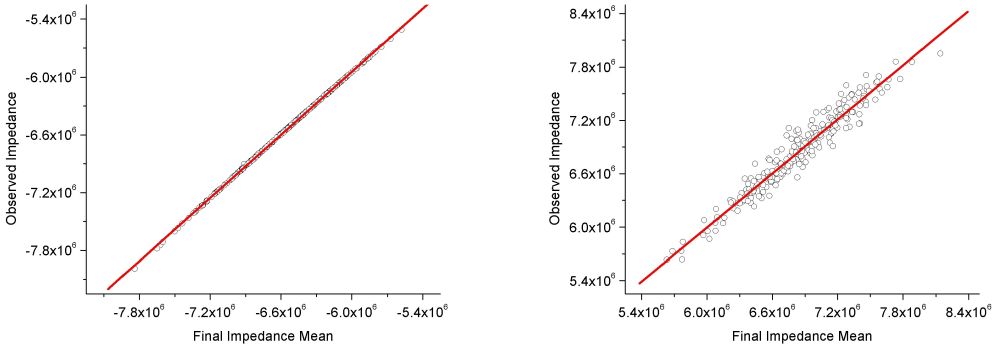

(a) First seismic impedance (b) Second seismic impedance

Figure 6.16: Cross plots of seismic impedance (M128F256 case)

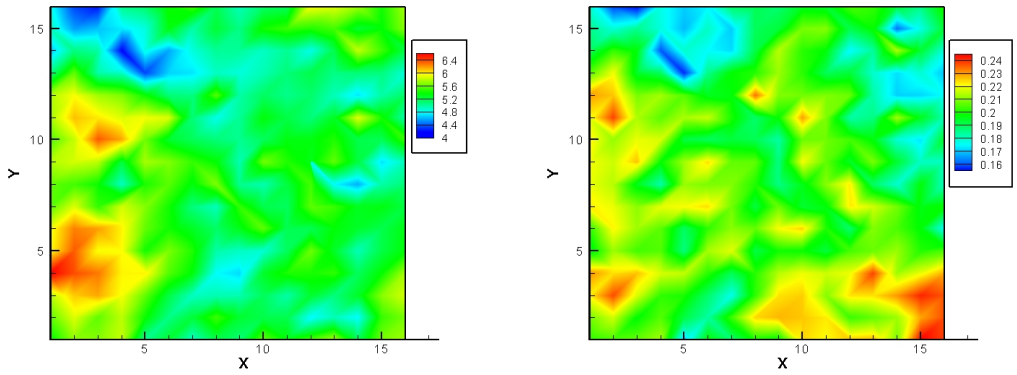

(a) Log permeability (b) Porosity

Figure 6.17: Final mean of log permeability and porosity (M128F256 case)

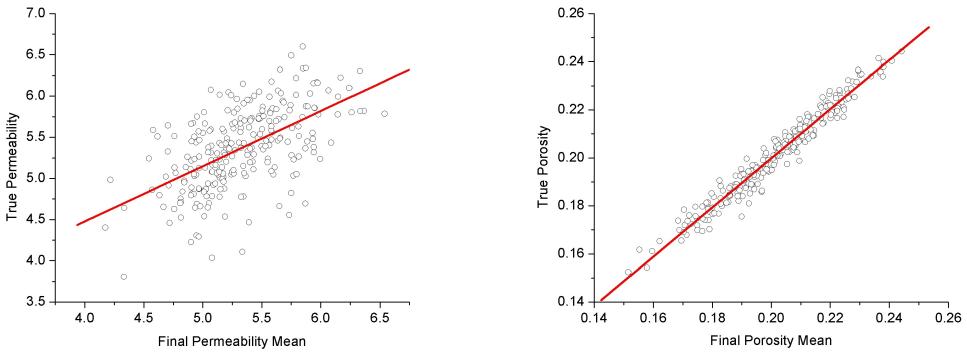

(a) Log permeability (b) Porosity

Figure 6.18: Cross plots of permeability and porosity (M128F256 case)

and the true permeability is better than it was for the M128 case, i.e., points are less scattered (Fig. 6.18(a)), which is clearer from Table 6.5. All regression lines use the

Parameter	A	B	R
Porosity	-0.00483	1.02319	0.97822
Log permeability	1.79454	0.67076	0.57235
First seismic impedance	6.035×10^5	1.09131	0.99987
Second seismic impedance	-8.559×10^4	1.01359	0.96793

Table 6.5: Regression parameters of porosity, log permeability, and impedance (M128F256 case)

same forms: $Y_{\text{true/obs}} = A + B * X_{\text{est./comp.}}$.

Using the same definition of the deviation in Eq. 6.20, evolution of both permeability deviation and porosity deviation from the truth are shown in Fig. 6.19 and Fig. 6.20. To have a legitimate comparison to the same type of plots in the M128 case, Fig. 6.19 and Fig. 6.20 use the same color scale respectively.

Comparing to the M128 case (Fig. 6.9(a)), the permeability deviation in M128F256 case (Fig. 6.19(a)) is very similar, with only minor differences at a few gridblocks. There are two reasons for the similarity: 1) improved initial sampling method uses the same prior PDF as conventional sampling method; 2) the deviation does not directly measure distances among the ensemble members so improvements are not obvious although the space spanned by resampled members is larger than that spanned by members without resampling. At day 1, the first seismic data are assimilated, which reduces deviations in some blocks, see Fig. 6.19(b). Compared with Fig. 6.9(b), the general features of Fig. 6.19(b) are almost identical because at day 1, seismic data are not sensitive directly to permeability field or indirectly through saturation because flow has not yet occurred. However, at locations with deviation reduction, it can be seen that the magnitude of reduction is larger in the M128F256 case than in the M128 case, i.e., light blue is replaced with dark blue. This better adjustment comes from better approximation to the covariance gained from the resampling algorithm. At day

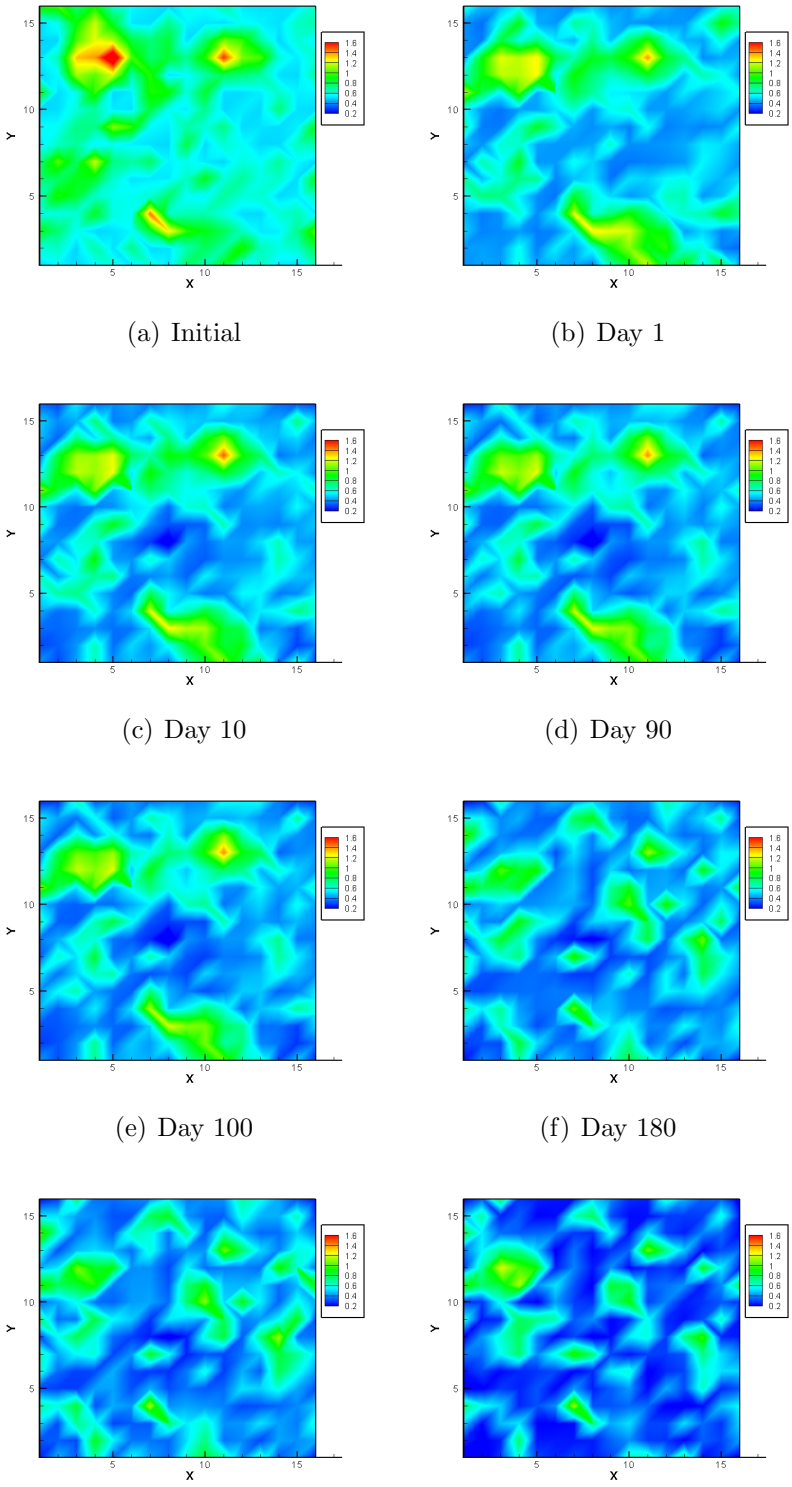

(a) Initial (b) Day 1

(c) Day 10 (d) Day 90

(e) Day 100 (f) Day 180

(g) Day 190 (h) Day 198

Figure 6.19: Evolution of permeability deviation from the truth (M128F256 case)

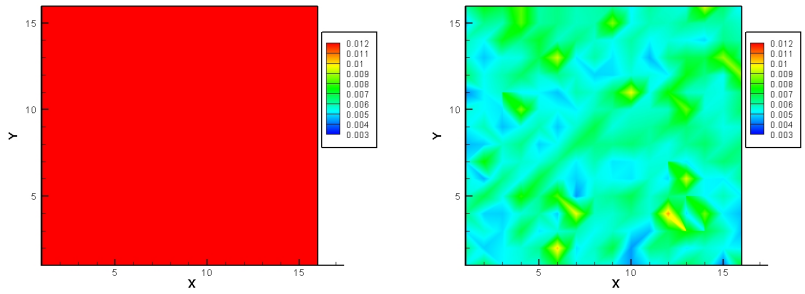

(a) Initial

(b) Day 1

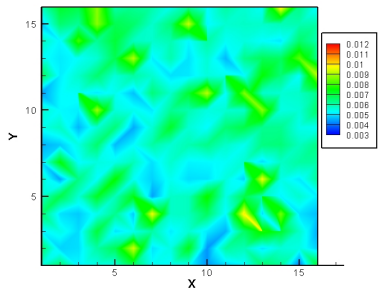

(c) Day 10

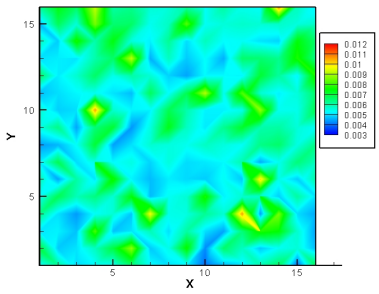

(d) Day 90

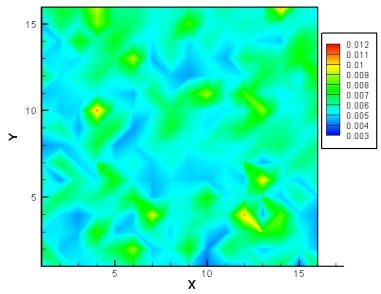

(e) Day 100

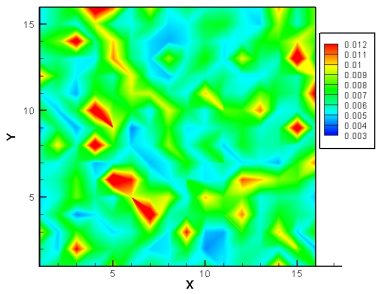

(f) Day 180

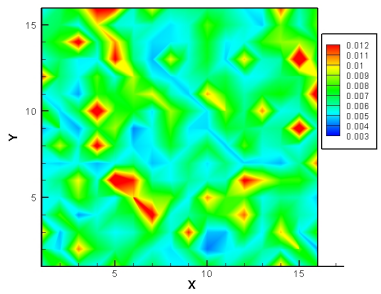

(g) Day 190

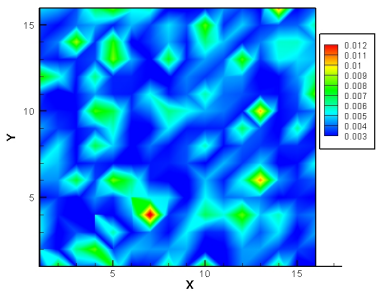

(h) Day 198

Figure 6.20: Evolution of porosity deviation from the truth (M128F256 case)

10, the first production data are assimilated. The reduction in the deviation is greater in this case (Fig. 6.19(c)) than that in the M128 case (Fig. 6.9(c)), especially at lower left corner and an area to the left side of the injector. Similar features can be seen from Fig. 6.19(d) and Fig. 6.9(d). The most important improvements obtained from re-sampling the initial members are around day 180 and day 190, see Fig. 6.19(f) and Fig. 6.19(g). Remember that some blocks have high deviations again at those two days in the M128 case due to over-adjustments around water breakthrough time at the well Prod-1 (Fig. 6.9(f) and Fig. 6.9(g)). In this case, however, there is no obvious increase in deviation, which shows that the resampled initial ensemble members have sufficient degrees of freedom to capture the true model parameters even when large changes in properties are required at water breakthrough. After second seismic data assimilation at day 198, permeability deviation has more reductions, see Fig. 6.19(h). Compared with the M128 case (Fig. 6.9(h)), more regions have low deviations in the M128F256 case, i.e., with dark blue color.

The porosity deviation also benefits from resampling the initial ensemble members (Fig. 6.20). At day 1, when the first seismic data are assimilated, the porosity deviation shows a large reduction (Fig. 6.20(a) and Fig. 6.20(b)), but the magnitude of the reduction is very similar to those shown in Fig. 6.10(b) of the M128 case because the porosity field is also recovered well in that case. At day 180 and day 190 when the well Prod-1 has water breakthrough, some regions return to high deviation values, note the red spots in Fig. 6.19(f) and Fig. 6.19(g). Compared with Fig. 6.9(f) and Fig. 6.9(g), however, there are fewer red spots, which shows that the over-adjustment problem for the porosity field has been reduced by using the resampled ensemble members. Also, the second seismic data assimilation reduces deviation more, see Fig. 6.20(h).

It is clear that the resampled initial ensemble members have better filter behavior, especially around water breakthrough time. The over-adjustment problem can be mitigated to some extent by using the resampled members. For permeability,

such improvements are more obvious than for porosity, partly because the porosity deviation before water breakthrough has been reduced to very low value.

Fig. 6.21 shows the **RMS** error defined in Eq. 6.21. It is clearer from Fig. 6.21(a)

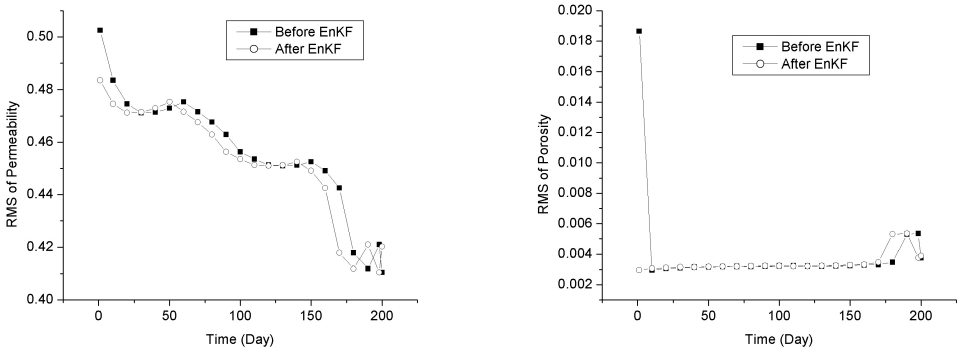

(a) Log permeability (b) Porosity

Figure 6.21: **RMS** error of permeability and porosity (M128F256 case)

that filter behavior using the resampled initial ensemble members is better than the M128 case (Fig. 6.11(a)): 1) there is continuous reduction in the **RMS** error between the two seismic surveys due to production data assimilation; 2) instability around water breakthrough time is not severe any more. The plot of the **RMS** error of porosity (Fig. 6.21(b)) still has similar feature as in the M128 case (Fig. 6.11(b)). The first seismic data assimilation gives a large reduction of the **RMS** error. The subsequent production data assimilation provides very small additional reduction to the **RMS** error. It can be understood from Fig. 6.22, which is the porosity mean at day 1 after seismic data assimilation. Comparing the figure with Fig. 6.1(b) and Fig. 6.7(b), it can be seen that porosity estimate is quite good by only using the first seismic data group. Subsequent improvement from production data assimilation is fairly minor because the estimate is already close to the truth. Around water breakthrough time, there are some oscillations, but the second seismic data assimilation returns the **RMS** error to a low value comparable with the one before water breakthrough. This phenomenon is also clear in Figs. 6.20(f) to 6.20(h).

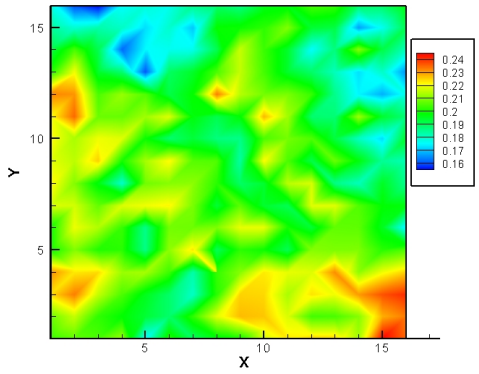

Figure 6.22: Mean porosity field after seismic data assimilation at day 1 (M128F256 case)

6.6 Summary

The small synthetic case study showed that the EnKF is a possible alternate method for automatic history matching both production data and time-lapse seismic data. Both production data and seismic impedance data were honored very well. The permeability field was not well constrained from the seismic data. The estimate of the porosity field from seismic data integration was quite good because seismic impedance is very sensitive to porosity. Production data are necessary to provide sensitivities to recover the permeability field and to provide constraints for the simulator.

128 ensemble members were enough for this small case. For large scale cases, however, a larger ensemble may be required. Determination of the size requires more investigation. When seismic data are considered, research based on some large scale problems are essential to determine if the EnKF with seismic data is scalable.

For this small case, the overall cost is 128 simulation runs plus overhead of matrices computation. However, for large scale problems, 128 members may be very demanding in computation resources. Hence, to reduce the number of ensemble members is a crucial issue for the EnKF. Therefore, to carefully select initial members by using improved sampling algorithm is highly necessary because resampled members can

usually provide large covariance space at the expense of small ensemble size.

CHAPTER VII

CONCLUSIONS

The main objective of this work is to develop an automatic history matching procedure to adjust reservoir simulation parameters at each gridblock by integrating both the seismic impedance change data and the production data. Since both the number of data and the number of model parameters are large, the adjoint method is used to efficiently compute the gradient of the objective function and the limited memory Broyden-Fletcher-Goldfarb-Shanno (LBFGS) method is applied to minimize the objective function without requiring the Hessian matrix. The reservoir simulator, CLASS (**C**hevron **L**imited **A**pplication **S**imulation **S**ystem) is used, so the resulting pressure and saturation distributions are forced to honor flow equations and material balance. A set of rock physics models are embedded into the simulator, which enables us to compute the seismic impedance change using output from the simulator.

Seismic data gathered from one seismic survey are sensitive to both the static reservoir parameters and the dynamic fluid flow related parameters. If seismic impedance change data are used, the effects from the static parameters can be reduced, and the dynamic parameters can be emphasized. It is shown that the effect of uncertainty in static parameters such as grain modulus or shaliness on the change in seismic impedance is small compared to the effect of change in saturation.

The procedure was tested on two case studies. The small synthetic case shows that the seismic impedance change data help to resolve the edges among 3 zones, each of which has difference permeability values. A semi-synthetic case study derived from the Tengiz field demonstrates the potential of this procedure to be applied to the large scale real problems. The adjoint method efficiently computes the gradient

of the objective function when the number of data, around 14,455, and the number of model parameters, 28,910, are both large. The LBFGS method achieves minimization without computing the Hessian matrix. Integration of seismic impedance change data recovers the boundaries between different zones, which are missed if only production data are used. Although the data have been honored well, the model variables are not well constrained.

In the real case study of the Bay Marchand field, the first seismic survey was shot long after production began, so the production history matching was conducted before matching the seismic impedance change data to provide an improved initial model for seismic data history matching. Although GOR data were also used in the production history matching, they were weighted less heavily than WOR data because the main driving mechanism in the field was water influx. The covariance matrix of the noise in the impedance change data was constructed by applying variogram analysis to the impedance changed data gathered from the aquifer. The water breakthrough time at all 7 wells were captured fairly well through production history matching. The water cuts were also matched more closely after history matching. History matching of the seismic impedance change data improved the water cut match although it did not substantially change the model parameters in field scale.

The small synthetic case study showed that it is possible to integrate both seismic impedance change data and production data using the EnKF for reservoir characterization. The improved initial member sampling algorithm increased the variability of the space spanned by the ensemble members, ensuring a more stable filter behavior. The porosity field was recovered much better than the permeability field because seismic impedance is more sensitive to porosity than to permeability.

Bibliography

Aanonsen, S. I., Efficient history matching using a multiscale technique, SPE 92758, in 2005 *SPE Reservoir Simulation Symposium*, 2005.

Aanonsen, S. I., I. Aavatsmark, T. Barkve, A. Cominelli, O. Gosselin, M. Kolasinski, and H. Reme, Effect of scale dependent data correlations in an integrated history matching loop combining production data and 4D seismic data, SPE 79665, in 2003 *SPE Reservoir Simulation Symposium*, 2003.

Aanonsen, S. I., A. Cominelli, O. Gosselin, I. Aavatsmark, and T. Barkve, Integration of 4D data in the history match loop by investigating scale dependent correlations in the acoustic impedance cube, *8th European Conference on the Mathematics of Oil Recovery*, 2002.

Abacioglu, Y., D. S. Oliver, and A. C. Reynolds, Efficient reservoir history matching using subspace vectors, *Computational Geosciences*, **5**(2), 151–172, 2001.

Abdassah, D., L. Mucharam, I. Soengkowo, H. Trikoranto, and R. Sumantri, Coupling seismic data with simulated annealing method improves reservoir characterization, SPE 36968, in 1996 *SPE Asia Pacific Oil and Gas Conference*, 1996.

Abriel, W. L., P. S. Neale, J. S. Tissue, and R. M. Wright, Seismic interpretation; 27, Modern technology in an old area; Bay Marchand revisited, *The Leading Edge*, **10**, 21–35, 1991.

Anderson, J. L., An ensemble adjustment Kalman filter for data assimilation, *Monthly Weather Review*, **129**, 2884–2903, 2001.

Anderson, J. L. and S. L. Anderson, A Monte Carlo implementation of the nonlinear filtering problem to produce ensemble assimilations and forecasts, *Monthly Weather Review*, **127**, 2741–2758, 1999.

Anterion, F., B. Karcher, and R. Eymard, Use of parameter gradients for reservoir history matching, SPE 18433, in *10th SPE Reservoir Simulation Symposium*, pp. 339–354, 1989.

Arenas, E., C. van Kruijsdijk, and T. Oldenziel, Semi-automatic history matching using the pilot point method including time-lapse seismic data, SPE 71634, in 2001 *SPE Annual Technical Conference and Exhibition*, 2001.

Aziz, K. and A. Settari, *Petroleum Reservoir Simulation*, Elsevier Applied Science Publishers, London, 1979.

Batzle, M. and Z. Wang, Seismic properties of pore fluids, *Geophysics*, **57**(11), 1396–1408, 1992.

Behrens, R., P. Condon, W. Haworth, M. Bergeron, Z. Wang, and C. Ecker, 4D seismic monitoring of water flux at Bay Marchand: The practical use of 4D in an imperfect world, *SPE Reservoir Evaluation and Engineering*, **5**(5), 410–420, 2002.

Biot, M. A., Theory of propagation of elastic waves in a fluid-saturated porous solid. I Low-frequency range, *The Journal of the Acoustical Society of America*, **28**(2), 168–178, 1956a.

Biot, M. A., Theory of propagation of elastic waves in a fluid-saturated porous solid. II Higher frequency range, *The Journal of the Acoustical Society of America*, **28**(2), 179–191, 1956b.

Biot, M. A., Generalized theory of acoustic propagation in porous dissipative media, *The Journal of the Acoustical Society of America*, **34**(9), 1254–1264, 1962.

Bissell, R., O. Dubrule, P. Lamy, P. Swaby, and O. Lepine, Combining goestatistical modelling with gradient information for history matching: The pilot point method, SPE 38730, in *Proceedings of the 1997 SPE Annual SPE Technical Conference and Exhibition*, pp. 139–154, 1997.

Blonk, B., R. W. Calvert, J. K. Koster, and G. van der Zee, Assessing the feasibility of a time-lapse seismic reservoir monitoring project, *SPE Reservoir Evaluation and Engineering*, **3**(1), 80–87, 2000.

Bogan, C., D. Johnson, M. Litvak, and D. Stauber, Building reservoir models based on 4D seismic & well data in Gulf of Mexico oil fields, SPE 84370, in 2003 *SPE Annual Technical Conference and Exhibition*, 2003.

Brown, R. G. and P. Y. C. Hwang, *Introduction to Random Signals and Applied Kalman Filtering*, pp. 230–236, John Wiley & Sons, Inc., New York, 1992.

Broyden, C. G., The convergence of a class of double rank minimization algorithm parts I and II, *Journal of Institute of Mathematics and its Applications*, **6**, 76–90 and 222–231, 1970.

Burgers, G., P. J. van Leeuwen, and G. Evensen, Analysis scheme in the ensemble Kalman filter, *Monthly Weather Review*, **126**, 1719–1724, 1998.

Burkhart, T., A. R. Hoover, and P. B. Flemings, Time-lapse (4-D) seimsic monitoring of primary production of turbidite reservoirs at south Timbalier block 295, offshore Louisiana, Gulf of Mexico, *Geophysics*, **65**(2), 351–367, 2000.

Certes, C. and G. de Marsily, Application of the pilot point method to the identification of aquifer transmissivities, *Advances in Water Resources*, **14**(5), 284–300, 1991.

Chavent, G. M., M. Dupuy, and P. Lemonnier, History matching by use of optimal control theory, *SPE Journal*, **15**(1), 74–86, 1975.

Chen, W. H., G. R. Gavalas, J. H. Seinfeld, and M. L. Wasserman, A new algorithm for automatic history matching, *SPE Journal*, **14**(6), 593–608, 1974.

Cooper, M., E. Thorogood, A. O'Donovan, P. Kristiansen, and P. Christie, Foinaven active reservoir management: The time-lapse signal, *1999 SEG Expanded Abstracts*, 1999.

de Marsily, G., G. Lavedan, M. Boucher, and G. Fasanino, Interpretation of interference tests in a well field using geostatistical techniques to fit the permeability distribution in a reservoir model, in *Geostatistics for Natural Resources Characterization, Part 2*, (edited by G. Verly, M. David, A. G. Journel, and A. Marechal), pp. 831–849, D. Reidell, Dordrecht, Holland, 1984.

Deutsch, C. V. and A. G. Journel, *Geostatistical Software Library and User's Guide*, Oxford University Press, New York, 1992.

Deutsch, C. V. and A. G. Journel, The application of simulated annealing to stochastic reservoir modeling, *SPE Applied Technology Series*, **2**(2), 222–227, 1994.

Dong, Y. and D. S. Oliver, Sensitivity of seismic impedance change to permeability and porosity, *TUPREP Annual Technical Report*, pp. 110–137, 2002.

Dong, Y. and D. S. Oliver, Quantitative use of 4D seismic data for reservoir characterization, *SPE Journal*, **10**(1), 91–99, 2005.

Dunlop, K. N. B., G. A. King, and E. A. Breltenbach, Monitoring oil/water fronts by direct measurement(includes associated papers 23943 and 24103), *Journal of Petroleum Technology*, pp. 596–602, 1991.

Eastwood, J., D. Johnston, X. Huang, K. Craft, and R. Workman, Processing for robust time-lapse seismic analysis: Gulf of Mexico example, Lena Field, *1998 SEG Expanded Abstracts*, 1998.

Evensen, G., Sequential data assimilation with a nonlinear quasi-geostrophic model using Monte Carlo methods to forecast error statistics, *Journal of Geophysical Research*, **99**(C5), 10,143–10,162, 1994.

Evensen, G., Advanced data assimilation for strongly nonlinear dynamics, *Monthly Weather Review*, **125**, 1342–1354, 1996.

Evensen, G., The ensemble Kalman filter: theoretical formulation and practical implementation, *Ocean Dynamics*, **53**, 343–367, 2003.

Evensen, G., Sampling strategies and square root analysis schemes for the EnKF, *Ocean Dynamics*, **54**, 539–560, 2004.

Evensen, G. and P. J. van Leeuwen, Assimilation of geosat altimeter data for the Agulhas current using the ensemble Kalman filter with a quasigeostrophic model, *Monthly Weather Review*, **124**, 85–96, 1996.

Fletcher, R., A new approach to variable metric algorithms, *Computer Journal*, **13**, 317–322, 1970.

Gao, G. and A. C. Reynolds, An improved implementation of the LBFGS algorithm for automatic history matching, SPE 90058, in 2004 *SPE Annual Technical Conference and Exhibition*, 2004.

Gao, G., M. Zafari, and A. C. Reynolds, Quantifying uncertainty for the PUNQ-S3 problem in a Bayesian setting with RML and EnKF, SPE 93324, in 2005 *SPE Reservoir Simulation Symposium*, 2005.

Gassmann, F., Elastic waves through a packing of spheres, *Geophysics*, **16**(4), 673–685, 1951.

Gavalas, G. R., P. C. Shah, and J. H. Seinfeld, Reservoir history matching by Bayesian estimation, *SPE Journal*, **16**(6), 337–350, 1976.

Goldfarb, D., A family of variable-metric methods derived by variational means, *Mathematics of Computing*, **24**, 23–26, 1970.

Golub, G. H. and C. F. van Loan, *Matrix Computations*, second edn., The Johns Hopkins University Press, Baltimore, 1989.

Gosselin, O., S. I. Aanonsen, I. Aavatsmark, A. Cominelli, R. Gonard, M. Kolasinski, F. Ferdinandi, L. Kovacic, and K. Neylon, History matching using time-lapse seismic (HUTS), SPE 84464, in 2003 *SPE Annual Technical Conference and Exhibition*, 2003.

Gosselin, O., A. Cominelli, S. van den Berg, and S. D. Chowdhury, A gradient-based approach for history-matching of both production and 4D seismic data, *7th European Conference on the Mathematics of Oil Recovery*, 2000.

Gouveia, W. P., D. H. Johnston, A. Solberg, and M. Lauritzen, Jotun 4D: Characterization of fluid contact movement from time-lapse seismic and production logging tool data, *The Leading Edge*, **23**(11), 1187–1194, 2004.

Greaves, R. J. and T. J. Fulp, Three-dimensional seismic monitoring of an enhanced oil recovery process, *Geophysics*, **52**(9), 1175–1187, 1987.

Gu, Y. and D. S. Oliver, The ensemble Kalman filter for continuous updating of reservoir simulation models, *Journal of Energy Resources Technology (in process of reviewing)*, 2005a.

Gu, Y. and D. S. Oliver, History matching of the PUNQ-S3 reservoir model: using the ensemble Kalman filter, *SPE Journal*, **10**(2), 2005b.

Guerin, G., *Acoustic and Thermal Characterization of Oil Migration, Gas Hydrates Formation and Silica Diagenesis*, Ph.D. thesis, Columbia University, 2000.

Hamill, T. M. and J. S. Whitaker, Distance-dependent filtering of background error covariance estimates in an ensemble Kalman filter, *Monthly Weather Review*, **129**, 2776–2790, 2001.

Han, D., A. Nur, and D. Morgan, Effects of porosity and clay content on wave velocities in sandstones, *Geophysics*, **51**(11), 2093–2107, 1986.

He, N., A. C. Reynolds, and D. S. Oliver, Three-dimensional reservoir description from multiwell pressure data and prior information, *SPE Journal*, **2**(3), 312–327, 1997.

Hill, R., The elastic behaviour of a crystalline aggregate, *Proceedings of the Physical Society of London Secton A*, **65**, 349–355, 1952.

Houtekamer, P. L. and H. L. Mitchell, Data assimilation using an ensemble Kalman filter technique, *Monthly Weather Review*, **126**, 796–811, 1998.

Houtekamer, P. L. and H. L. Mitchell, A sequential ensemble Kalman filter for atmospheric data assimilation, *Monthly Weather Review*, **129**, 123–137, 2001.

Huang, X., L. R. Bentley, and C. Laflamme, Integration of production history and time-lapse seismic data guided by seismic attribute zonation, SPE 68819, in 2001 *SPE Western Regional Meeting*, 2001.

Huang, X., L. Meister, and R. Workman, Reservoir characterization by integration of time-lapse seismic and production data, SPE 38695, in 1997 *SPE Annual Technical Conference and Exhibition*, 1997.

Hughes, J. K., Examination of seismic repeatability as a key element of time-lapse seismic monitoring, SPE 50627, in 1998 *SPE European Petroleum Conference*, 1998.

Hughes, J. K., Examination of seismic repeatability as a key element of time-lapse seismic monitoring, *SPE Reservoir Evaluation and Engineering*, **3**(6), 517–524, 2000.

Jacquard, P. and C. Jain, Permeability distribution from field pressure data, *SPE Journal*, **5**(4), 281–294, 1965.

Jahns, H. O., A rapid method for obtaining a two-dimensional reservoir description from well pressure response data, *SPE Journal*, **6**(12), 315–327, 1966.

Kalman, R. E., A new approach to linear filtering and prediction problems, *Journal of Basic Engineering (ASME)*, **82**, 35–45, 1960.

Khan, M., J. R. Waggoner, and J. K. Hughes, 4D cause and effect: What do reservoir fluid changes look like on seismic, SPE 63132, in 2000 *SPE Annual Technical Conference and Exhibition*, 2000.

Kitanidis, P. K., Quasi-linear geostatistical theory for inversing, *Water Resources Research*, **31**(10), 2411–2419, 1995.

Koster, K., P. Gabriels, M. Hartung, J. Verbeek, G. Deinum, and R. Staples, Time-lapse seismic surveys in the North Sea and their business impact, *The Leading Edge*, **19**(3), 286–293, 2000.

Kretz, V., M. L. Ravalec-Dupin, and F. Roggero, An integrated reservoir characterization study matching production data and 4D seismic, *SPE Reservoir Evaluation and Engineering*, **7**(2), 116–122, 2004a.

Kretz, V., B. Vallès, and L. Sonneland, Fluid front history matching using 4D seismic dana streamline simulation, SPE 90136, in 2004 *SPE Annual Technical Conference and Exhibition*, 2004b.

Kuster, G. T. and M. N. Toksöz, Velocity and attenuation of seismic waves in two-phase media: Part 1. theoretical formulations, *Geophysics*, **39**(5), 587–606, 1974.

Landa, J. L. and R. N. Horne, A procedure to integrate well test data, reservoir performance history and 4-D seismic information into a reservoir description, SPE 38653, in 1997 *SPE Annual Technical Conference and Exhibition*, 1997.

Landrø, M., Discrimination between pressure and fluid saturation changes from time-lapse seismic data, *Geophysics*, **66**(3), 836–844, 2001.

Li, R., *Conditioning Geostatistical Models to Three-Dimensional Three-Phase Flow Production Data by Automatic History Matching*, Ph.D. thesis, University of Tulsa, Tulsa, Oklahoma, 2001.

Li, R., A. C. Reynolds, and D. S. Oliver, History matching of three-phase flow production data, *SPE Journal*, **8**(4), 328–340, 2003.

Liu, N. and D. S. Oliver, Critical evaluation of the ensemble Kalman filter on history matching of geologic facies, SPE 92867, in 2005 *SPE Reservoir Simulation Symposium*, 2005.

Lumley, D. E., Time-lapse seismic reservoir monitoring, *Geophysics*, **66**(1), 50–53, 2001.

Lumley, D. E., R. A. Behrens, and Z. Wang, Assessing the technical risk of a 4D seismic project, *The Leading Edge*, **16**(9), 1287–1292, 1997.

Lumley, D. E., A. G. Nunns, G. Delorme, and M. F. Bee, Meren field, Nigeria: A 4D seismic case study, *1999 SEG Expanded Abstracts*, 1999.

Lumley, D. E., A. Nur, S. Strandenes, J. Dvorkin, and J. Packwood, Seismic monitoring of oil production: A feasibility study, *1994 SEG Expanded Abstracts*, 1994.

Lumley, D. E. and A. Viejo, Business and technology challenges for 4D seismic reservoir monitoring, *The Leading Edge*, **23**(11), 1166–1168, 2004.

Makhlouf, E. M., W. H. Chen, M. L. Wasserman, and J. H. Seinfeld, A general history matching algorithm for three-phase, three-dimensional petroleum reservoirs, *SPE Advanced Technology Series*, **1**(2), 83–91, 1993.

Meadows, M. A., Enhancements to Landro's method for separating time-lapse pressure and saturation changes, *2001 SEG Expanded Abstracts*, 2001.

Mezghani, M., A. Fornel, V. Langlais, and N. Lucet, History matching and quantitative use of 4D seismic data for an improved reservoir characterization, SPE 90420, in 2004 *SPE Annual Technical Conference and Exhibition*, 2004.

Murphy, W., A. Reischer, and K. Hsu, Modulus decomposition of compressional and shear velocities in sand bodies, *Geophysics*, **58**(2), 227–239, 1993.

Nævdal, G., L. M. Johnsen, S. I. Aanonsen, and E. H. Vefring, Reservoir monitoring and continuous model updating using ensemble Kalman filter, *SPE Journal*, **10**(1), 66–74, 2005.

Nævdal, G., T. Mannseth, and E. H. Vefring, Near-well reservoir monitoring through ensemble Kalman filter, SPE 75235, in 2002 *SPE/DOE Improved Oil Recovery Symposium*, 2002.

Nocedal, J., Updating quasi-Newton matrices with limited storage, *Mathematics of Computation*, **35**(151), 773–782, 1980.

Nocedal, J. and S. J. Wright, *Numerical Optimization*, pp. 47–49, Springer, New York, 1999.

Nolen-Hoeksema, R. C., Modulus-porosity relations, Gassmann's equations, and the low-frequency elastic-wave response to fluids, *Geophysics*, **65**(5), 1355–1363, 2000.

Oliver, D. S., Moving averages for Gaussian simulation in two and three dimensions, *Mathematical Geology*, **27**(8), 939–960, 1995.

Oliver, D. S., Multiple realizations of the permeability field from well-test data, *SPE Journal*, **1**(2), 145–154, 1996.

Ouenes, A., S. Bhagavan, P. H. Bunge, and B. J. Travis, Application of simulated annealing and other global optimization methods to reservoir description: myths and realities, SPE 28415, in 1994 *SPE Annual Technical Conference and Exhibition*, 1994.

Ouenes, A., B. Bréfort, G. Meunier, and Dupere, A new algorithm for automatic history matching: Application of simulated annealing method (SAM) to reservoir inverse modeling, *SPE 26297*, 1993.

Ouenes, A., G. Meunier, V. Pelce, and I. Lhote, Enhancing gas reservoir characterization by simulated annealing method (SAM), SPE 25023, in 1992 *SPE European Petroleum Conference*, 1992.

Pannett, S., S. Slager, G. Stone, and S. Dekker, Constraining a complex gas-water dynamic model using 4D seismic, SPE 89793, in 2004 *SPE Annual Technical Conference and Exhibition*, 2004.

Peaceman, D. W., Interpretation of well-block pressures in numerical reservoir simulation with non-square grid blocks and anisotropic permeability, *SPE Journal*, **23**(6), 531–543, 1983.

Phan, V. and R. N. Horne, Fluvial channel parameter estimation constrained to static, production and 4D seismic data, SPE 77518, in 2002 *SPE Annual Technical Conference and Exhibition*, 2002.

Portellaand, R. C. M. and F. Prais, Use of automatic history matching and geostatistical simulation to improve production forecast, SPE 53976, in 1999 *SPE Latin American and Caribbean Petroleum Engineering Conference*, 1999.

Porter-Hirsche, J. and K. Hirsche, Repeatability study of land data acquisition and processing for time lapse seismic, *1998 SEG Expanded Abstracts*, 1998.

Raef, A. E., R. D. Miller, A. P. Byrnes, and W. E. Harrison, 4D seismic monitoring of the miscible CO2 flood of Hall-Gurney field, Kansas, U.S., *The Leading Edge*, **23**(11), 1171–1176, 2004.

Ramammorthy, R., W. F. Murphy, and C. Coll, Total porosity estimation in shaly sands from shear modulus, *SPWLA 36th Annual Logging Symposium Transactions*, pp. H1–H12, 1995.

RamaRao, B. S., A. M. LaVenue, G. de Marsily, and M. G. Marietta, Pilot point methodology for automated calibration of an ensemble of conditionally simulated transmissivity fields, 1. Theory and computational experiments, *Water Resources Research*, **31**(3), 475–493, 1995.

Reichle, R. H., D. B. McLaughlin, and D. Entekhabi, Hydrologic data assimilation with the ensemble Kalman filter, *Monthly Weather Review*, **130**, 103–114, 2002.

Reuss, A., Berechnung der fliessgrense von mischkristallen auf grund der plastizitatbedingung fur einkristalle, *Zeitschrift fur Angewandte Mathematik aus Mechnik*, **9**, 49–58, 1929.

Rickett, J. and D. E. Lumley, Cross-equalization data processing for time-lapse seismic reservoir monitoring: A case study from Gulf of Mexico, *Geophysics*, **66**(4), 1015–1025, 2001.

Roggero, F., Direct selection of stochastic model realizations constrained to historical data, SPE 38731, in 1997 *SPE Annual Technical Conference and Exhibition*, pp. 155–165, 1997.

Romero, C. E., J. N. Carter, A. C. Gringarten, and R. W. Zimmerman, A modified genetic algorithm for reservoir characterisation, SPE 64765, in 2000 *SPE International Oil and Gas Conference and Exhibition in China*, 2000.

Ross, C. P., G. B. Cunningham, and D. P. Weber, Inside the crossequalization black box, *The Leading Edge*, **15**(11), 1233–1240, 1996.

Saccomano, A. F., G. B. Savioli, and M. S. Bidner, Stochastic modeling of rock heterogeneities applying new autocorrelation estimators and simulated annealing, SPE 69654, in 2001 *SPE Latin American and Caribbean Petroleum Engineering Conference*, 2001.

Sen, M. K., A. D. Gupta, P. L. Stoffa, L. W. Lake, and G. A. Pope, Stochastic reservoir modeling using simulated annealing and genetic algorithm, *SPE Formation Evaluation*, **10**(1), 49–56, 1995.

Shah, S., G. R. Gavalas, and J. H. Seinfeld, Error analysis in history matching: The optimum level of parameterization, *SPE Journal*, **18**(3), 219–228, 1978.

Shanno, D. F., Conditioning of quasi-Newton methods for function minimization, *Mathematics of Computation*, **24**(111), 647–656, 1970.

Shyeh, J. J., D. H. Johnston, J. E. Eastwood, M. Khan, and L. R. Stanley, Interpretation and modeling of time-lapse seismic data: Lena field, Gulf of Mexico, SPE 56731, in 1999 *SPE Annual Technical Conference and Exhibition*, 1999.

Smith, T. M., C. H. Sondergeld, and C. S. Rai, Gassmann fluid substitutions: A tutorial, *Geophysics*, **68**(2), 430–440, 2003.

Sorenson, H. W., *Kalman Filtering: Theory and Application*, IEEE Press, 1985.

Tarantola, A., *Inverse Problem Theory: Methods for Data Fitting and Model Parameter Estimation*, Elsevier, Amsterdam, The Netherlands, 1987.

Tura, A. and D. Lumley, Estimating pressure and saturation changes from time-lapse AVO data, *1999 SEG Extended Abstracts*, 1999.

van Ditzhuijzen, R., T. Oldenziel, and van Kruijsdijk, Geological parameterization of a reservoir model for history matching incorporating time-lapse seismic based on a case study of the Statfjord field, SPE 71318, in 2001 *SPE Annual Technical Conference and Exhibition*, 2001.

van Leeuwen, P. J. and G. Evensen, Data assimilation and inverse methods in terms of probabilistic formulation, *Monthly Weather Review*, **124**, 2898–2913, 1996.

Vasco, D. W., A. Datta-Gupta, Z. He, R. Behrens, J. Rickett, and P. Condon, Reconciling time-lapse seismic and production data using streamline models: the Bay Marchand field, Gulf of Mexico, SPE 84568, in 2003 *SPE Annual Technical Conference and Exhibition*, 2003.

Vasco, D. W., A. Datta-Gupta, and J. C. S. Long, Integrating field production history in stochastic reservoir characterization, *SPE Formation Evaluation*, **12**(3), 149–156, 1997.

Voight, W., *Lehrbuch der Kristallphysik: Teubner*, 1928.

Waggoner, J. R., 4D seismic, synergy, not just integration, of geophysics and engineering, SPE 50665, in 1998 *SPE European Petroleum Conference*, 1998.

Waggoner, J. R., A. Cominelli, and R. H. Seymour, Improved reservoir modeling with time-lapse seismic in a Gulf of Mexico gas condensate reservoir, SPE 77956, in 2002 *SPE Asia Pacific Oil and Gas Conference and Exhibition*, 2002.

Wang, Z., Fundamentals of seismic rock physics, *Geophysics*, **66**(2), 398–412, 2001.

Wayland, J. R. and D. Lee, Seismic mapping of EOR processes, *The Leading Edge*, **5**(12), 36–40, 1986.

Wen, X.-H. and W. H. Chen, Real-time reservoir model updating using ensemble Kalman filter, SPE 92991, in 2005 *SPE Reservoir Simulation Symposium*, 2005.

Wen, X.-H., C. V. Deutsch, and A. S. Cullick, High resolution reservoir models integrating multiple-well production data, SPE 38728, in 1997 *SPE Annual Technical Conference and Exhibition*, pp. 115–129, 1997.

Wen, X.-H., C. V. Deutsch, and A. S. Cullick, High-resolution reservoir models integrating multiple-well production data, *SPE Journal*, **3**(4), 344–355, 1998.

Wen, X.-H., C. V. Deutsch, and A. S. Cullick, Construction of geostatistical aquifer models integrating dynamic flow and tracer data using inverse technique, *Journal of Hydrology*, **255**(1–4), 151–168, 2002.

Wu, Z., A. C. Reynolds, and D. S. Oliver, Conditioning geostatistical models to two-phase production data, *SPE Journal*, **3**(2), 142–155, 1999.

Xu, W., T. T. Tran, R. M. Srivastava, and A. G. Journel, Integrating seismic data in reservoir modeling: The collocated Cokriging approach, SPE 24742, in 1992 *SPE Annual Technical Conference and Exhibition*, 1992.

Xue, G., A. Datta-Gupta, P. Valko, and T. Blasingame, Optimal transformations for multiple regression: Application to permeability estimation from well logs, *SPE Formation Evaluation*, **12**(2), 85–94, 1997.

Yeh, W. W.-G., Review of parameter identification in groundwater hydrology: The inverse problem, *Water Resources Research*, **22**(2), 95–108, 1986.

Yilmaz, Ö. and S. M. Doherty, *Seismic data analysis : processing, inversion, and interpretation of seismic data*, Society of Exploration Geophysicists, Tulsa, OK, 1987.

Zhang, F., *Automatic History Matching of Production Data for Large Scale Problems*, Ph.D. thesis, University of Tulsa, Tulsa, Oklahoma, 2002.

Zhang, F. and A. C. Reynolds, Optimization algorithms for automatic history matching of production data, *8th European Conference on the Mathematics of Oil Recovery*, 2002.

Zhang, F., A. C. Reynolds, and D. S. Oliver, The impact of upscaling errors on conditioning a stochastic channel to pressure data, *SPE Journal*, **8**(1), 13–21, 2003.